Role of Electrical Synapses in the Rat Inferior Olive: Assessment During Postnatal Development and After Knockdown of Connexin 36

Dissertation

zur Erlangung des Grades eines

Doktors der Naturwissenschaften

der Mathematisch-Naturwissenschaftlichen Fakultät

und

der Medizinischen Fakultät

der Eberhard-Karls-Universität Tübingen

vorgelegt

von

Jens Robert Müller

aus Aichhalden, Deutschland

2025

Tag der mündlichen Prüfung:	4. Juni 2024
Dekan der Math.-Nat. Fakultät:	Prof. Dr. Thilo Stehle
Dekan der Medizinischen Fakultät:	Prof. Dr. Bernd Pichler
1. Berichterstatter:	Prof. Dr. Peter Thier
2. Berichterstatter:	Prof. Dr. Hansjürgen Volkmer
Prüfungskommission:	Prof. Dr. Peter Thier
	Prof. Dr. Hansjürgen Volkmer
	Prof. Dr. Steffen Hage
	Prof. Dr. Fahad Sultan

Erklärung / Declaration:

Ich erkläre, dass ich die zur Promotion eingereichte Arbeit mit dem Titel *„Role of Electrical Synapses in the Rat Inferior Olive: Assessment During Postnatal Development and After Knockdown of Connexin 36“* selbständig verfasst, nur die angegebenen Quellen und Hilfsmittel benutzt und wörtlich oder inhaltlich übernommene Stellen als solche gekennzeichnet habe. Ich versichere an Eides statt, dass diese Angaben wahr sind und dass ich nichts verschwiegen habe. Mir ist bekannt, dass die falsche Abgabe einer Versicherung an Eides statt mit Freiheitsstrafe bis zu drei Jahren oder mit Geldstrafe bestraft wird.

I hereby declare that I have produced the work entitled *„Role of Electrical Synapses in the Rat Inferior Olive: Assessment During Postnatal Development and After Knockdown of Connexin 36“* submitted for the award of a doctorate, on my own (without external help), have used only the sources and aids indicated and have marked passages included from other works, whether verbatim or in content, as such. I swear upon oath that these statements are true and that I have not concealed anything. I am aware that making a false declaration under oath is punishable by a term of imprisonment of up to three years or by a fine.

Tübingen, den _____ _____

Datum / Date Unterschrift / Signature

Meinen Eltern

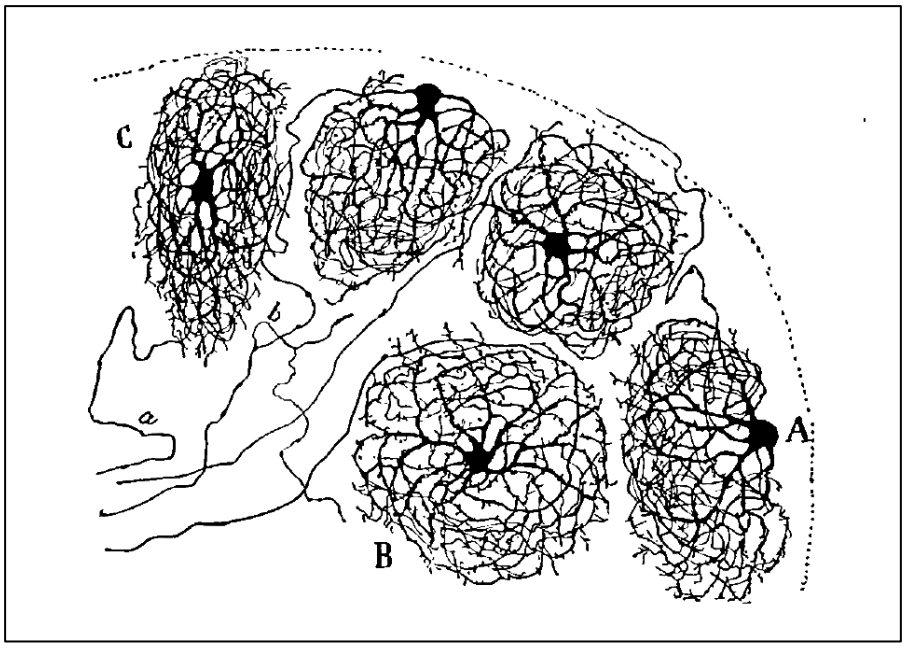

Cellules de l'olive bulbaire: enfant nouveau-né. Méthode de Golgi. Adapted from Ramón y Cajal (1909).

Ramón y Cajal S. *Histologie du système nerveux de l'homme & des vertébrés*. Paris: Maloine, A., 1909.

Table of contents

Summary

The inferior olive is a brainstem nucleus which receives input from a broad spectrum of sources ranging from visual and auditory to proprioceptive and nociceptive to vestibular and motor-sensory inputs as well as cortical innervation but also inhibitory innervation from the cerebellar nuclei via the olivo-cerebellar loop. Olivary neurons project to Purkinje cells in the cerebellar cortex via the climbing fibers and to the cerebellar nuclei via climbing fibers collaterals. While the input is manifold and integrates many modalities, the output climbing fiber signal consists of a short high frequency burst with a variable number of burst components but an amazingly low burst frequency of about 1-2 Hz. The climbing fiber signal elicits a massive calcium influx in the dendritic tree of Purkinje cells which gives rise to the somatic complex spike. Although Purkinje cell function has drawn a lot of attention, the purpose of the complex spike and its source, the climbing fiber signal, remain only poorly understood. This has consequences for the understanding of the role of the cerebellum at large. A key towards better insight into the nature of cerebellar function may therefore lie in the investigation of the function of the inferior olive in general and of the spatio-temporal nature of olivary neuron activity in particular.

Neurons of the inferior olive are remarkable as they are densely connected to each other via dendro-dendritic electrical synapses –the highest density of electrical synapses in the central nervous system – resulting in clusters of electrotonically coupled neurons. It has been shown that these electrical synapses are primarily composed of the gap junction protein connexin 36 (Cx36). Olivary neurons exhibit sub-threshold oscillations (STO) which are based on the interplay of calcium conductances. These oscillations are highly synchronous among neighboring olivary neurons and it is assumed that electrical coupling provides the means of this synchrony. Current interpretations of the functional relevance of the STO assume that the probability of regenerative events is higher at the peak of the STO phase when the membrane is more depolarized. This would allow a temporal and spatial control of activity among coupled neurons. Moreover, recent work has indicated that the strength of coupling among olivary neurons is dynamically regulated on different time scales. In particular synaptic input located at the electrical synapses seems to be able to modulate coupling and thus provide control over the extent of coupled neuron clusters and their synchrony on a short time scale.

Previous studies have attempted to understand the purpose of the electrotonic coupling by using Cx36 knockout mice. In these animals olivary neurons were able to maintain STO in the absence of Cx36 but the oscillations were not in synchrony any more. Yet, only a mild phenotype with subtle impairment of motor learning but not of motor coordination could be described. This may be due to the fact that olivary neurons compensate for the lack of Cx36 on the cellular level. To overcome the issue of developmental compensation lentiviral vector mediated dominant negative inhibition of

Summary

Cx36 in rats was used as a tool to transduce olivary neurons. This work showed that olivary neurons in areas with high transduction density were no longer able to maintain STO. Unfortunately animals used in this work were not subjected to behavioral assessment and thus no conclusion on possible motor impairment could be drawn. Hence, it also remains unexplored what possible consequences on locomotion may arise from postnatal reduction of Cx36 based coupling.

We tried to address the role of Cx36 mediated coupling in the rat inferior olive by a strategy resting on two pillars.

The first pillar was formed by investigating the change of gap junctional coupling during the first postnatal weeks. We recorded the presence and properties of spontaneous regenerative events (spontaneous action potentials and spikelets) as well as STO in olivary neurons in acute brain slices from animals at postnatal week two, three or five with the whole-cell patch clamp technique. Furthermore, we diffused neurobiotin, a gap junction permeable dye, to the patch clamp recorded neurons and reconstructed the extent of the coupled networks in three dimensional confocal laser scanning microscopy image stacks.

The second pillar was formed by RNA interference mediated knockdown of Cx36 by specific short-hairpin RNA delivered by lentiviral vector. At three weeks (postnatal day 21) viral vector solution was stereotaxically injected in the center of the inferior olive under electrophysiological guidance. Animals (5w-shCx36) were allowed to recover for several days and were subjected to free locomotion analysis before being sacrificed at postnatal week five for whole-cell patch clamp recordings of olivary neurons / neuron pairs. Recordings of pairs of olivary neurons enabled us to assess the electrotonic coupling in 5w-shCx36 neurons compared to the wildtype or non-functional control and to investigate differences in STO presence and synchrony. Moreover, we examined the occurrence of spontaneous regenerative events and their kinetics in respect to the phase and amplitude of the STO cycle in the prospect to identify features that may code for the oscillatory state of the respective neuron – putative important information to be transmitted to the cerebellar cortex and the cerebellar nuclei.

We found that gap junctional coupling among olivary neurons undergoes dynamical changes during the first postnatal weeks with highest coupling around postnatal week three. Whereas no case of neurobiotin dye-coupling could be observed at postnatal week two, the incidence of dye-coupling and the number of coupled cells per dye-filled neuron increased at postnatal week three but dropped again by postnatal week five. Robust STO were not found until postnatal week three, the time point of maximal coupling, and continued to be present from then on. The probability of occurrence of spontaneous action potentials as well as of spikelets in olivary neurons followed the dynamics of gap junctional coupling and so did the spontaneous firing frequencies of both event

types. We further found a general maturation of the regenerative events during postnatal development. Spontaneous action potentials as well as spikelets became faster from postnatal week two to five, indicating substantial changes in membrane channel composition and density.

RNAi was found to effectively reduce the amount of Cx36 immunoreactivity in transduced olivary neurons indicating that a substantial proportion of gap junctions was eliminated. This manifested in highly reduced dye-coupling and almost complete diminishing of electrical coupling. The largely absent coupling led to an increased probability of observing spontaneous action potentials. Moreover, the firing frequency of spontaneous action potentials was higher than in the age matched wildtype, resembling frequencies found in olivary neurons from postnatal week three. Interestingly, spikelets were still observed in 5w-shCx36 neurons which is counterintuitive to the idea of them being the echo of action potentials transmitted across gap junctions, questioning the prevailing interpretation. Uncoupled 5w-shCx36 neurons were less able to maintain STO synchrony with neighboring neurons. Yet, most of these neurons were stable oscillators during the full time of recording and we even observed an increase in dominant STO frequency as a result of uncoupling.

We observed that spontaneous action potentials and spikelets occurred independent of the STO phase at postnatal week three. At postnatal week five however, both event types were aligned to the peak of the STO phase. In contrast, uncoupling led to a loss of spikelet alignment to the STO phase while the alignment of spontaneous action potentials to the STO phase was undisturbed. Parameters of the kinetics of both regenerative event types were sensitive to the STO phase or amplitude and may be capable to convey information about the oscillatory state of the neuron.

While several electrophysiological changes on the neuronal level could be attributed to the loss of gap junctional coupling, we identified only a mild phenotype during free locomotion. Classifying animals based on the affected olivary sub-nuclei, we could identify most alterations of locomotion parameters when substantial parts of the medial accessory olive (MAO) were transduced.

We conclude that gap junctional coupling is necessary for the proper maintenance of STO synchrony and the timing of spikelets in respect to the STO phase. Moreover, spontaneous activity of IO neurons seems to positively depend on coupling. Furthermore, features of action potential and spikelet kinetics appear to convey information on the STO phase and amplitude at event occurrence. Yet, on the level of locomotor coordination, only moderate changes were observed and it seems that the impact was strongest if the medial accessory olive was affected to a great extent.

1. Introduction

Since Ramón y Cajal's first and beautifully illustrated description of neurons of the inferior olive (IO) (page V, Ramón y Cajal (1909)) the extraordinary gross anatomical appearance of this brainstem nucleus and later even more so the puzzling functional connectivity have fascinated neuroanatomists and neurophysiologists alike.

Neurons of the inferior olive are remarkable in several ways: i) they are the sole source of the cerebellar climbing fibers, ii) they unite excitatory and inhibitory synaptic input close to electrical synapses in a structure known as the glomerulus, and iii) a (sub-) type of IO neurons maintains retroverting dendrites that bend back in the direction of the soma. Here, theories of olivo-cerebellar function will be described and put in context to the unique features of IO neurons. Moreover, experimental strategies to investigate the olivo-cerebellar function are illustrated leading to presentation of the study performed here.

1.1 Afferent and efferent connectivity of the inferior olive

The nuclei of the inferior olive receive a manifold of afferent innervation and have a topographically organized output to the Purkinje cells (PC) of the cerebellar cortex (Figure 1).

The dorsal accessory olive (DAO) receives primarily somatosensory input from the spinal cord and the dorsal column nuclei and projects to the vermis and intermediate areas of the posterior lobe of the cerebellum. The principal olive (PO) is innervated by input from the red nucleus, the nucleus of the optic tract, nucleus Darkschewitsch, and cortical areas as well as likely from the perirubral area and from diencephalic sources. Many of these innervations are associated with motor instances. The PO predominantly projects to the hemispheres of the cerebellum. The broadest spectrum of afferents can be found for the medial accessory olive (MAO). Input from the spinal cord, dorsal column nuclei, vestibular nuclei, tectal and pretectal sources, periaqueductal gray, and the nucleus of Darkschewitsch project to different lamellar areas of the MAO. The vertical lamella of the MAO projects to the posterior vermis and to the flocculus whereas the horizontal and the rostral lamellae project to the anterior vermis and to intermediate areas or the hemispheres, respectively (Azizi and Woodward 1987). For a further detailed review see also Glickstein et al. (2011).

IO neurons are the sole source of the climbing fibers (CF) which project to PC in the cerebellar cortex (Desclin 1974; Szentágothai and Rajkovits 1959) and to neurons of the cerebellar nuclei (CN) via CF collaterals, although the latter projection appears to be weak (Lu et al. 2016). These projections preserve a topography where proximity of IO neurons is represented in parasagittal zones of CF-PC innervation (Armstrong et al. 1974; Sugihara and Shinoda 2004; 2007; Sugihara et al. 2001). The projections of PCs of such a parasagittal zone converge on neurons of the CN. These

neurons in turn project to the respective IO neurons that give rise to the CFs projecting to the very sagittal zone, constituting a loop-like connectivity - the proposed cerebellar module (Apps and Garwicz 2000; Ruigrok 2011).

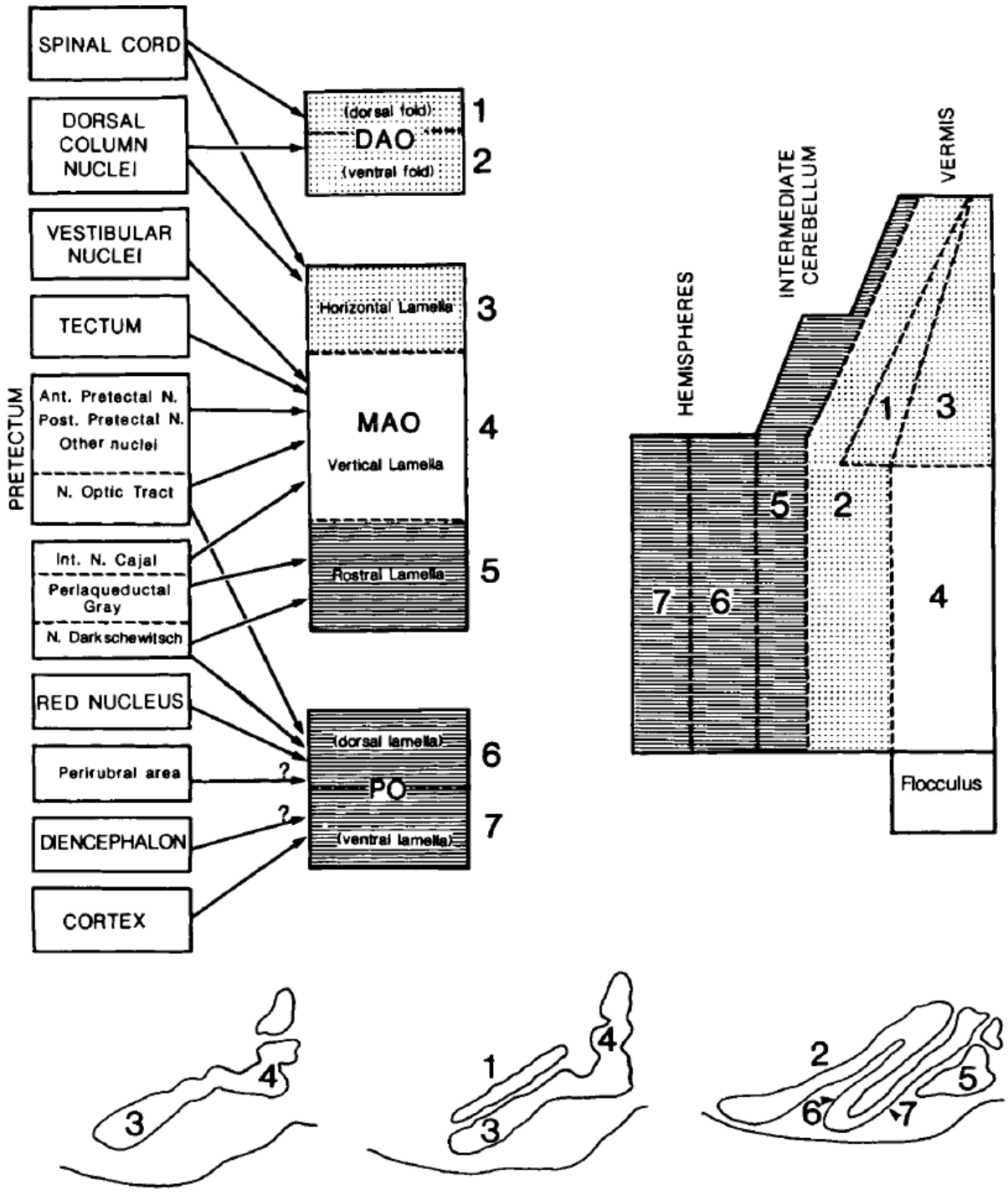

Figure 1. Schematic diagram of lamellar and zonal distribution of olivary afferents and efferents.
The two lamellae (folds) of the DAO (1 and 2) and the horizontal lamella of the MAO (3) receive afferents mainly from the spinal cord and dorsal column nuclei while projecting to the anterior vermis and to parts of the intermediate cerebellum. The medial MAO (vertical lamella, 4) receives input from vestibular and visual areas and projects to the posterior vermis and to the flocculus. The rostral lamella of the MAO and both lamellae of the PO receive projections from higher centers and send fibers to the lateral hemispheres. From Azizi and Woodward (1987) (reproduction with permission from Wiley, license number: 4680980432221).

1.2 Developmental changes in climbing fiber innervation

The CF innervations to PC of the cerebellar cortex undergo major alterations during the first three weeks of postnatal development (Hashimoto and Kano 2013) (**Figure 2**), before the onset of puberty in small rodents (mouse: postnatal week 5, rat: postnatal week 6 - 8) (Zutphen et al. 2001).

Neurons of the inferior olive establish axons to the developing cerebellum by embryonic day 18 (Morara et al. 2001; Wassef et al. 1992) but it is not before postnatal day 3 (p3) that a functional innervation of PCs can be found (Crepel 1971). Initially, at a time when the dendritic tree of the PCs is not yet developed, multiple different CFs originating from different IO neurons terminate on one PC soma. These multiple innervations can be measured as graded excitatory post-synaptic responses in a PC if the corresponding section of the IO or the CFs are electrically stimulated at increasing intensities (Crepel et al. 1976; Kakegawa et al. 2015).

Between p3 - p7, one single CF innervation is strengthened in an activity dependent manner while the other CFs remain unchanged (Hashimoto and Kano 2003). From p9 on, this strengthened CF translocates from the soma to the meanwhile more developed PC dendrites. Around the same time the non-strengthened CFs are eliminated which is only completed by p17 or even later (Hashimoto et al. 2009). It has recently been described that from p14 - 16 to p17 - 19 a steep increase in CS firing rate may either reflect the strengthening of one CF or may play a role in activity dependent maturation (Arancillo et al. 2015). In a final stage, synaptic connections of the solitary “winner” CF with the PC dendrite undergo further maturation (Hashimoto and Kano 2013). This is accompanied by the transformation of the PC dendrite towards its adult monoplanar appearance in the third postnatal week (Kaneko et al. 2011). While initially CF maturation was considered to establish a hard wiring that would persist during life, it became obvious more recently that CF morphology is under dynamical change throughout adulthood (Cesa and Strata 2009) and may be an important substrate for cerebellar learning.

During the time frame described above (first three postnatal weeks), transition from immature to adult locomotion pattern takes place in mice and rats (Westerga and Gramsbergen 1990) and in the light of activity dependent differentiation, the question of the contribution of olivary synchrony in shaping the olivo-cerebellar connectivity is still persisting.

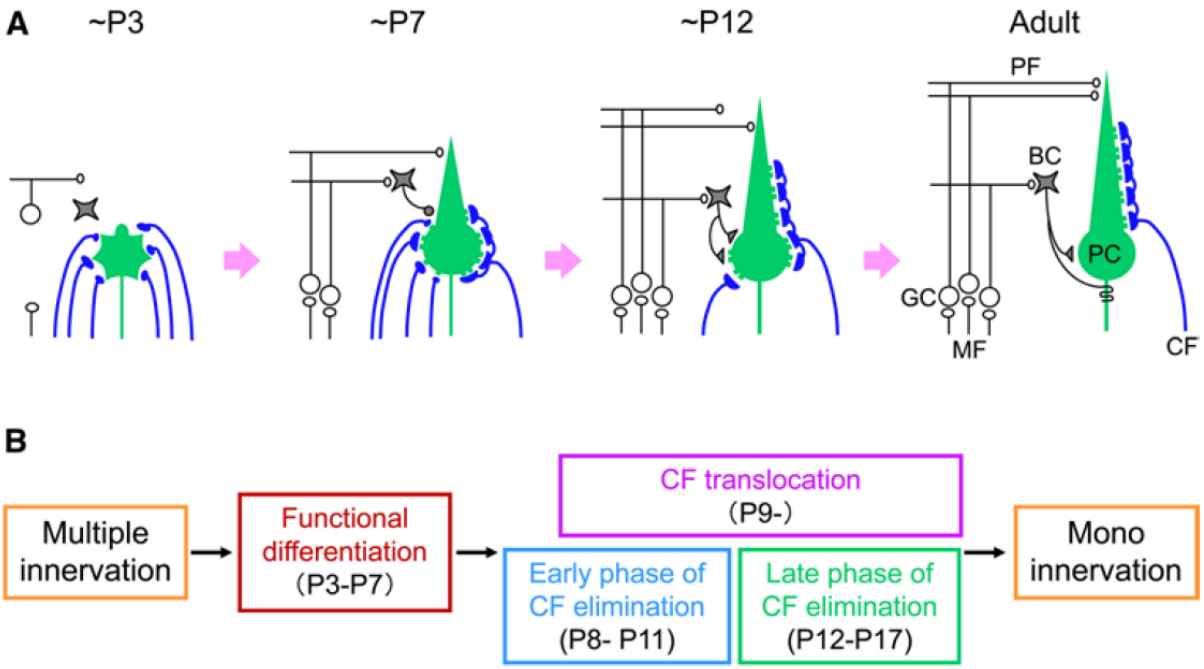

Figure 2. Postnatal refinement of CF to PC synapses.
A Postnatal development of CF-PC synapses in the mouse. CF, climbing fiber; BC, basket cell; GC, Golgi cell; MF, mossy fiber; PC, Purkinje cell; PF parallel fiber. **B** Four distinct phases of postnatal refinement of CF-PC synapses. From Hashimoto and Kano (2013) (reproduction under Creative Commons license CC-BY).

1.3 Temporal and spatial integration of electrical and chemical synaptic input in IO neurons

1.3.1 The glomerulus as the site of multi-synaptic integration

The inferior olive receives excitatory input especially but not exclusively from multiple sensory and motor-sensory sites but also inhibitory input from the CN (see above, section 1.1). The way these innervations are structured on the micro-anatomical and synaptic level is quite extraordinary. The electrical synapses that connect dendrites of neighboring IO neurons are found in dendritic protrusions known as glomeruli. It is on these glomeruli where excitatory and inhibitory synapses converge (de Zeeuw et al. 1990a) (**Figure 3**) and one may wonder about the functional significance of such a unique structural arrangement. For a long time it been assumed that the synaptic input may act on the electrical synapse by modulating its efficacy but experimental prove has been lacking until recently addressed in three coinciding elegant studies.

Turecek et al. (2014) showed that NMDA receptors are located in proximity to electrical synapses and that synaptic or pharmacologic activation of NMDA receptors strengthened the gap junctional coupling on a short time scale. This led to an increase in STO synchrony among neighboring IO neurons and extended the size of the coupled cluster of neurons. Yet, on a longer time scale,

repetitive spike triggering excitatory input can lead to long-term depression of electrical coupling (Mathy et al. 2014).

Glutamatergic input to the glomerulus may therefore be a positive modulator of coupling among IO neurons and synchrony on a short time scale but a negative modulator of coupling when the input is long lasting and repetitive.

Also, the inhibitory synapse that originates from the CN has received attention. Strong inhibition on dendritic structures on both sides of the electrical synapse could practically shunt the movement of charges across it and render the electrical synapse dysfunctional for the time of the inhibition (Llinas 1974). Such inhibition would be a fast handle to disconnect IO neuron ensembles and be able to shape the extent of local synchronous clusters on a short time scale. Best and Regehr (2009) could show that the high firing rate of the GABAergic CN neurons projecting to the IO is translated into an asynchronous synaptic release and into a rather long lasting inhibitory current in IO neurons, a synaptic property perfectly suited for this kind of shunt inhibition.

Indeed, selective optogenetic activation of CN axon terminals within the IO could reliably elicit inhibitory post-synaptic potentials (IPSPs) in IO neurons. As a consequence, the coupling between IO neurons (measured in paired patch clamp recordings) was substantially reduced and showed increased a asymmety during the time of inhibitory synaptic activation. Additionally, optogenetically evoked IPSPs had either a phase shifting effect on STO when only single IPSPs were elicited, or dampened or suppressed STO when trains of IPSPs were elicited (Lefler et al. 2014). These findings indicate that the cerebellum actively controls the coupling and rhythmic activity of IO neurons and ultimately the spatio-temporal elements of the CF signal by the interplay of convergent innervation of excitatory and inhibitory afferents in the proximity of electrical synapses.

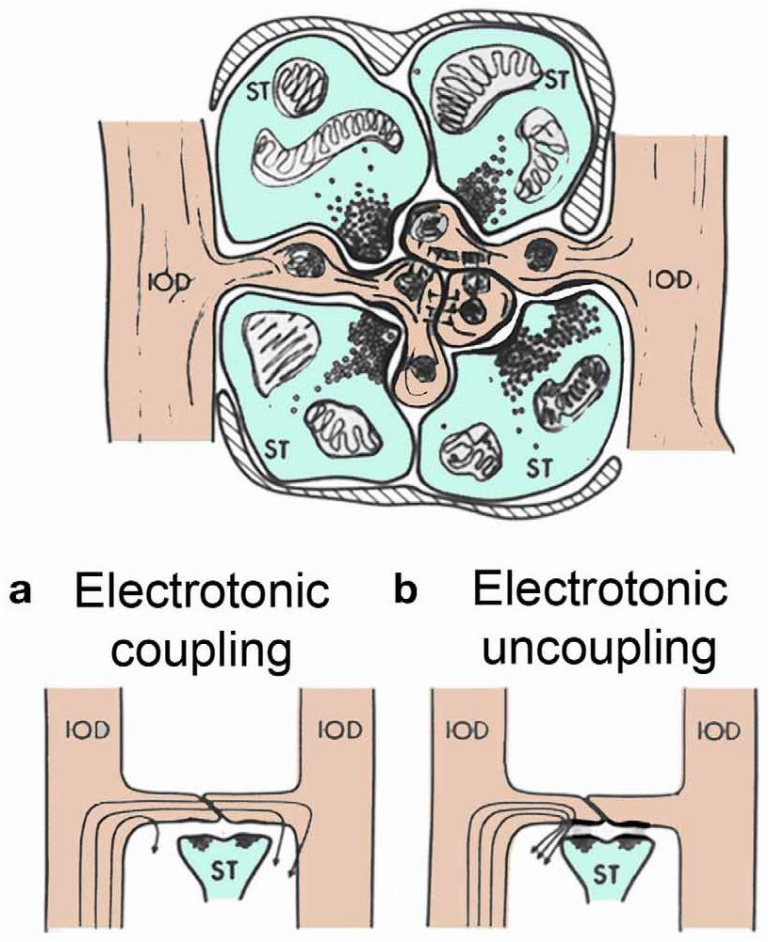

Figure 3. The olivary glomerulus.
Two dendritic spines interconnected by electrical synapses are surrounded by axonal terminals of excitatory and inhibitory nature. **a** Current flow from one dendrite to another is maintained by electrical synapse connection. **b** GABA release at the inhibitory synapse blocks current flow across the electrical synapse by shunting inhibition. From Llinas (2013) (reproduction under Creative Commons license CC-BY).

1.3.2 Retroverting dendrites

IO neurons exhibit a broad heterogeneity in dendritic morphology and directionality (Vrieler et al. 2019). Two main types of IO neurons can be distinguished by their dendritic morphology: Type I features straight dendrites where the Euclidian distance from the soma increases with dendrite length and grade of arborization, whereas Type II shows a dendritic morphology where this "rule" is violated in the way that distal dendritic arbors tend to bend back towards the soma, leading to a curly appearance (Devor and Yarom 2002a; Foster and Peterson 1986). These retroverting dendrites are a rather unique morphological feature in the mammalian CNS yet it is unclear what their functional purpose may be. Here, a possible functional explanation will be outlined that suggests to receive experimental attention.

Spatial and temporal integration of synaptic input at dendritic sites and transmission along the dendritic tree are complex and depend on a multitude of factors such as i) density and spatial distribution of synaptic input ii) set of ion channels, and iii) modulation of their opening probabilities

and kinetics. Moreover, iv) on the balance and spatio-temporal position of excitatory and inhibitory input, v) on the dendritic diameter, or vi) the presence of "hot zones" that govern the current density at distinctive regions.

An electrical synapse between IO neurons N_1 and N_2 could potentially connect one dendrite (D_1) originating from N_1 to a dendrite (D_2) of a neighboring neuron (N_2) in two ways that potentially result in great differences of spatio-temporal integration along a dendrite (**Figure 4**).

(i) At glomerulus site 1 (G_1), an electrical synapse could be formed to make a connection between dendritic spines of D_1 and D_2, where the spine location on D_2 is proximal to the soma of N_2. In this case a depolarizing electrical volley in D_1 would invade the neighboring dendrite D_2 via the electrical synapse and travel along D_2 towards active dendritic zones and/or to the soma in short time. Integration proximal to the soma would likely increase its relative impact on the somatic depolarization and its contribution to sub- as well as supra-threshold events might be high.

(ii) Another dendritic spine originating from the same location on D_1 could be part of a glomerulus site G_2 and would also connect to a dendritic spine of D_2. In this case though, the spine on D_2 would have its base far distant on the retroverting part of D_2 and thus would have a much longer dendritic distance to the soma of N_2. Therefore, the same electrical volley originating in D_1 would be transferred to D_2 but would need far longer to travel along the dendrite until it could contribute to the somatic signal. Moreover, this signal would likely have a totally different spatio-temporal integration profile than the signal in i).

One could also imagine that the different run-time along the dendrites may introduce asymmetry of signal transmission. Backpropagation of signals from the soma towards electrical synapses that are located on distal parts of a dendrite may lead to a significant attenuation compared to signal propagation to proximally located electrical synapses. In the given example, in N_1 a somatic signal of given amplitude may reach G_1 or G_2 with comparable intensity that would allow successful transmission across the respective electrical synapses and that may both be propagated to the soma of N_2 by passive and active dendritic properties. Yet, in the other direction, a somatic signal in N2 would reach G_2 only highly attenuated (compared to G_1), further dampening at the electrical synapse may then reduce the transmission to a great extent or even abolish it.

Current theories of the function of the inferior olive, from pace-making to motor learning, share the idea that timing is a key element (see below, section 1.4). The unique morphology of IO retroverting dendritic trees may be particularly suited to serve that purpose.

Assuming connections like i) and ii) exist in parallel, it is imaginable that the convergent excitatory and inhibitory input (see above, section 1.3.1) could act as a selective switch to channel signals towards either the "short" or "long" route on a millisecond time scale.

On a longer time scale dendro-dendritic connections to a dendrite of the same target neuron could be eliminated at one site G_1 just to be established on a different more distal part of the same dendrite at G_2 but with totally different spatio-temporal contribution to the dendritic integration. Dynamical emergence, relocation, modulation and elimination of dendro-dendritic gap junctions along two adjacent dendrites that share an overlapping space may alter the "run-time" of a current volley (elicited by ions passing the gap junction) along a dendrite and/or change its integration. Such dynamics may result in changes of synchrony and spike timing and might form a means to precisely establish morphological correlates of temporal components of (motor-) learning and/or timing.

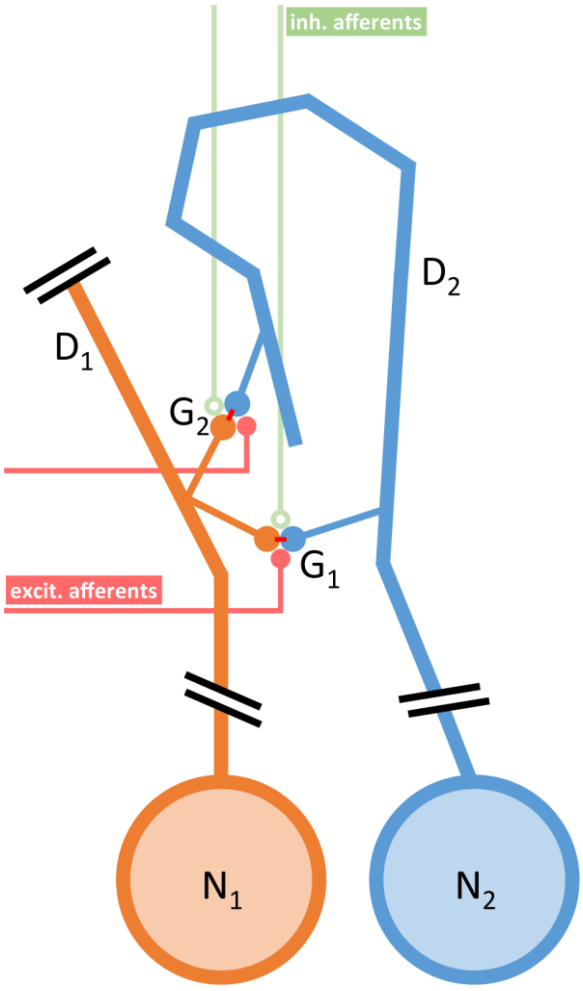

Figure 4. Retroverting dendrites of IO neurons differently connected by glomeruli.
Two IO neurons N_1, N_2 are connected via dendro-dendritic gap junctions (electrical synapses, red) either by glomerulus G_1 or by glomerulus G_2. The spines contributing to G_1 and G_2 have their basis in close proximity on dendrite D_1 - and thus at about the same distance to the soma. In contrast, the spines on the other side of the electrical synapse connect to D_2 at different distance to the soma. Signals from D_1 passing to D_2 via G_2 would have a considerably longer "run-time" towards the soma compared to signals passing via G_1. Selective excitatory and inhibitory inputs to G_1 and G_2 may govern the route signals will take.

1.4 Theories of olivo-cerebellar function

Several, partially competing theories on the function of the IO have been proposed. It has been suggested that the IO plays a pivotal role in cerebellar motor learning (Marr 1969). The theory's key element builds on the convergence of mossy fiber and CF input upon the PC of the cerebellar cortex. On one hand, input from the mossy fibers, which enter the cerebellar cortex via granule cells and project to PC via their parallel fiber (PF) output, would conduct information about the context in which a movement was initiated. On the other hand, information about the movement itself would be received via the CF signal. In the case of coinciding converging input the formation of an association mediated by facilitation of PF synapses would be expected. This association could then be retrieved by PF input alone and elicit a movement. Independently of Marr, Albus (1971) developed a theory where he expanded and modified the concept in the light of the contribution of inhibitory interneurons in memory formation. He proposed a framework where PF synapses on PC and interneurons are weakened if activities of PF and CF coincide. Moreover, CF activity would serve as the unconditioned stimulus and mossy fiber activity as the conditioned stimulus and thus the CF inactivation would constitute the unconditioned response. This concept found first experimental support by Yeo et al. (1985) and also more recently by Zbarska et al. (2008) in studies exploiting the nictitating membrane response of the rabbit. Also, in the non-human primate, altered complex spike activity during saccadic adaptation was observed (Catz et al. 2005) and another study showed that CS suppress simple spikes (SS) in the successive trial during active learning of smooth pursuit eye movements (Medina and Lisberger 2008). Junker et al. (2018) recently confirmed the concept that the CF signal contains information about motor-errors during trial-based saccadic learning. Furthermore, they made the surprising observation that this information is reverberated in successive trials for a prolonged period – which points to the IO as an important instance for the maintenance and coordination of motor-errors. It has also been shown recently that a gradual decrease in complex spike activity takes place during acquisition of conditioned response in a classical conditioning paradigm (Rasmussen et al. 2014). Moreover, IO neurons primarily respond to somatosensory input which may also be indicative of a role in associative learning (Gibson et al. 2004). Yet, the purpose of the resulting CF signal is far from being understood.

Another school neglects the learning theories but views the IO and its CF signal as a pace making entity that mainly serves the purpose of providing a clock for the coordination or spatio-temporal alignment of motor patterns (Lampl and Yarom 1993; Llinas and Muhlethaler 1988; Llinas 2009). Rhythmic firing based on the sub-threshold oscillations and the electrotonic coupling of IO neurons (Bazzigaluppi et al. 2012; Llinas and Yarom 1986; Mathy et al. 2009) are thought to form the basis of this clock. A plethora of experiments support the timing hypothesis. For example, electrical stimulation of the lip induces a CS with an effectiveness that appears to be bound to the underlying

IO rhythmic sub-threshold oscillation setting the pace for input gating (Llinas and Sasaki 1989). Also, simultaneous recordings from PCs while rats performed a licking task revealed synchronous rhythmic CS firing indicating that the IO plays a role in the organization of movement in time (Welsh et al. 1995). During constant speed treadmill locomotion, rats exhibit robust rhythmic discharges of IO neurons at frequencies similar to the step cycle frequencies. This rhythmicity is maintained even at short periods of step irregularity (Smith 1998). Moreover, stimulation of the tongue area of the primary motor cortex provided insight into the way how synchronous CF activity can rhythmically gate mossy fiber signals and thus modulate SS firing rate and rhythm dynamics (Schwarz and Welsh 2001).

As seen, over the last decades many studies on this matter were conducted yielding support to both concepts. Yet, we might well see these two aspects amalgamate into a consistent concept of olivo-cerebellar function in the near future in respect to spatio-temporal integration of somato- and motor-sensory and feedback modalities. A common denominator of both main theories seems to be the timing of activity of IO neurons and a key to a better understanding may lie in the careful examination of synchronicity within this structure.

1.5 Olivary impairment and clinical manifestations

Olivary impairment in patients is rare and most commonly emerges in the form of hypertrophic olivary degeneration (HOD) as a consequence of a lesion along the segment of the so-called Guillain-Mollaret triangle which connects the contralateral dentate nucleus with the ipsilateral inferior olive, passing around the ipsilateral red nucleus.

HOD clinically manifests as palatal tremor, a persistent myoclonus of the palate, or oculopalatal tremor with the addition of synchronous, oscillatory movement of the eyes (pendular nystagmus), and dysmetric saccades.

On the anatomical level HOD appears in the name-giving hypertrophy of the olives, in swelling, vacuolation and shape change of IO neurons, fibrillary gliosis and demyelination; eventually followed by neuronal cell loss in the IO. It is assumed that the pathological changes in the olives are the result of the loss of inhibitory synapses from the dentate nucleus as a consequence of the aforementioned deafferentation.

On the functional level it is suggested that the olives show increased firing activity possibly due to the increased electrotonic coupling following disinhibition due to the deafferentation of CN input and a shift of gap junctions from the dendrite to the soma (de Zeeuw et al. 1990c; Ruigrok et al. 1990). Modelling of abnormal, synchronous firing of IO neurons could attribute pacemaker properties for oculopalatal tremor oscillations to the IO but also indicated the importance of a modulator instance

in the cerebellum (Shaikh et al. 2010). For a comprehensive review, see also Tilikete and Desestret (2017).

Interestingly, subjects exhibiting oculopalatal tremor showed impaired fast and slow motor learning in a saccadic adaptation paradigm presumably due to the stochastic, synchronous CF signal which fails to serve as a meaningful error-signal (Shaikh et al. 2017).

Moreover, a recent post-mortem histological examination of the IO in humans revealed age related accumulation of intraneuronal granules, possibly composed of lipofuscin, as well as cell loss in some subjects. These observations were interpreted as a possible aspect of age-related changes in motor and cognitive performance of the cerebellum (Baizer et al. 2018).

1.6 Experimental lesion of the inferior olive

Full olivectomy results in ataxic and dysmetric movements (Murphy and O'Leary 1971; Wilson and Magoun 1945) and more recent work in the cat could show that destruction of distinct IO sub-nuclei by kainic acid (Horn et al. 2012) or blockade of glutamatergic input to distinct IO sub-nuclei (Horn et al. 2010) impairs grasping or induces ataxic limb movements. Moreover, chemical lesion of the rat IO also results in impaired motor learning (Llinas et al. 1975) and inactivation of the IO by lidocaine has even been shown to inhibit associative learning (Welsh and Harvey 1998). Compensatory mechanisms may take action likely within the CN as SS firing rates in PC are increased during the acute phase after IO lesion but drop to baseline levels after 4 weeks (Benedetti et al. 1984).

In any case, the interpretation of the results is not straight forward as the lesion destroys also the access of information to the cerebellum normally conveyed by the IO. Hence, an interference with relaying of information cannot be separated from processing within the IO.

1.7 Electrical synapses

One of the most remarkable features of IO neurons is that they are coupled via electrical synapses which are formed by dendro-dendritic gap junctions (Llinas and Yarom 1981a; Sotelo et al. 1974) predominantly composed of connexin 36 (Cx36) (Belluardo et al. 2000; Condorelli et al. 1998). These gap junctions connect dendrites within a protrusion called the glomerulus where afferents from the mesodiencephalic junction and from the CN terminate in close proximity (de Zeeuw et al. 1990a; de Zeeuw et al. 1990b).

It was expected that investigation of the role of the extensive but weak gap junctional coupling among IO neurons (Devor and Yarom 2002a; Hoge et al. 2011) would be the key to the understanding of IO function. It could be shown that the characteristic prominent sub-threshold oscillations (STO) are synchronous among neighboring neurons (Devor and Yarom 2002b) and it is

assumed that this synchrony is maintained by electrotonic coupling via gap junctions (Devor and Yarom 2002a) which are perfectly suited for this kind of synchronization due to their low-pass filter properties (Galarreta and Hestrin 1999).

The creation of $Cx36^{-/-}$ mice (Güldenagel et al. 2001) was expected to reveal a phenotype with distinct motor impairments that could elucidate the role of electrical synapses within the olivo-cerebellar circuitry.

On the neuronal level, the elimination of gap junctions in these mice results in hyperexcitability as well as in STO desynchronization (Long et al. 2002) and reduced complex spike synchrony (Marshall et al. 2007). Yet, surprisingly, $Cx36^{-/-}$ mice show only minor impairments in motor learning (Van Der Giessen et al. 2008) as well as abnormal spinocerebellar reflexes (De Gruijl et al. 2014) but they are not ataxic and have only slight deficits in motor performance (Frisch et al. 2005; Kistler et al. 2002). Also, many aspects of the phenotype might be explained by the global loss of Cx36 affecting for example cortical interneurons (Deans et al. 2001) and neurons in the retina (Güldenagel et al. 2001). On the other hand, morphological and functional changes in IO neurons seem to take place during development which are likely capable to partially compensate for the loss of coupling (De Zeeuw et al. 2003), again with relevance for the behavior.

To overcome these putative developmental adaptations counteracting on the Cx36 depletion, alternative strategies were utilized. A dominant negative Cx36 mutation was introduced into the rat IO by local injection of a lentiviral vector which impaired muscle coherence in the low millisecond range (Placantonakis et al. 2004) and abolished robust sub-threshold oscillations (Placantonakis et al. 2006). Nevertheless, reported plaque formation of wildtype and mutant Cx36 protein aggregates alongside incomplete inhibition may have had an unfathomable impact on affected neurons. Moreover, neither detailed description of electrophysiological features (i.e. firing activity or action potential properties) nor behavioral data from animals that were manipulated in such manner are available so far.

1.8 Pharmacological inhibition of gap junctions

Pharmacological inhibition of gap junctions has been utilized in the attempt to gain further insight into their function. Local administration of the non-selective gap junction blocker carbenoxolone revealed their importance for complex spike (CS) synchrony (Blenkinsop and Lang 2006). However, incomplete blockade (Rozental et al. 2001), and complex effects on membrane properties, excitability, calcium oscillations and synaptic transmission (Rouach et al. 2003; Tovar et al. 2009) make it difficult to accept this blocker as a specific tool for a detailed investigation of the effect of electrical synapses on cellular electrophysiological properties i.e. conductances or kinetics of active events. Yet, it is noteworthy that another study could show impaired eye-blink conditioning in human

users of mefloquine, an anti-malaria drug and gap junction blocker of connexins 36, 43 and 50 (van Essen et al. 2010). However, these results should be taken with caution as none of the known gap junction blockers are highly specific (Manjarrez-Marmolejo and Franco-Perez 2016).

1.9 Developmental changes in gap junctional coupling

A potential route to the understanding of the purpose of gap junctional coupling among IO neurons might be to study the emergence and manifestation of gap junctions and the associated neuronal activity during the first weeks of postnatal development – a time period in which adult motor patterns are being established (Westerga and Gramsbergen 1990) and the CF connectivity undergoes major transformations (Hashimoto et al. 2009; Sugihara 2006). While early structural studies suggested the emergence of gap junctions in the IO not earlier than postnatal day 10 (p10) when the glomeruli are formed (Bourrat and Sotelo 1983), it has also been reported that during early postnatal development, clusters of IO neurons exhibit synchronous Ca^{2+}-transients and that the probability of their observation peaked around p12.5 but declined to about zero at p15.5 (Rekling et al. 2012). Moreover, STO seem to emerge between p9 - p16 (Bleasel and Pettigrew 1992). These observations also coincide with an expression of ionotropic glutamate receptors peaking around p10 before decreasing to adult levels prior to p30 (Rao et al. 1995).

1.10 Manipulation of protein expression by RNA interference

As our study uses RNA interference (RNAi) to manipulate IO gap junctions, we briefly describe its functional principle and utilization as a tool to selectively inhibit expression of a target protein.

1.10.1 Principle of RNA interference

RNAi in animals was first described with the finding that the introduction of either sense or antisense RNA had similar degrading effects to a target mRNA transcript in the nematode Caenorhabditis elegans (Guo and Kemphues 1995). Soon after, Craig Mello and Andrew Fire found that double-stranded RNA could block protein expression in C. elegans (Fire et al. 1998) – an achievement they were awarded the Nobel Prize in Physiology or Medicine in 2006. In the attempt to translate the application to mammalian cells it became obvious that short double-stranded RNA sequences (short interfering RNA: siRNA) of about 21 - 23 nucleotides in length and complementary to their target mRNA were determining the target mRNA cleavage site (Elbashir et al. 2001a; Elbashir et al. 2001b; Zamore et al. 2000) leading to a massive reduction in expression of the respective protein.

Attempts to utilize RNAi as a tool to manipulate the protein expression in the mammalian CNS *in vivo* were soon initiated but faced several challenges that also remain to be constraints in possible

human therapeutic application so far. The blood-brain barrier blocks siRNA from reaching cells of the CNS (Pardridge 2002). Moreover, “naked” siRNA injected to the striatum did not prove to be efficient, likely because it is not taken up by neurons (Isacson et al. 2003). Experimentally complex techniques like electroporation of siRNA into neurons have been reported to be effective (Akaneya et al. 2005) but did not reach broader application. Moreover, RNAi mediated by external siRNA is transient and may therefore have reduced effectiveness on target proteins with long half-life.

A potent alternative lies in employing viral vectors as vehicles that transduce target cells with a sequence coding for a short-hairpin RNA (shRNA) that contains a target specific sequence (Elkobi et al. 2008; Kriebel et al. 2011; Xia et al. 2004; Zitman et al. 2014).

Figure 5 shows a simplified illustration of the current understanding of the RNAi pathway mediated by lentiviral vector transduction of the target cell and delivery of the genetic material coding for a designed shRNA, typically under the control of a suitable promoter. The genetic material carried by the lentiviral vector is integrated into the genome of the host cell. The shRNA coding sequence is expressed under the control of a (cell specific) active promoter. The shRNA is transported to the cytoplasm where Dicer cleaves the hairpin loop and releases a double-stranded siRNA. The siRNA is then incorporated into the RISC complex where the guide strand is selected and the passenger strand is released to undergo degradation. RISC binds to a region of the target mRNA that is complementary to the sequence of the guide strand. Within the complementary sequence cleavage takes place and after release from RISC the mRNA fragments undergo degradation. The reduction of target mRNA subsequently leads to a reduction of the respective protein level – the RNAi based knockdown. For a comprehensive review see (Davidson and McCray 2011).

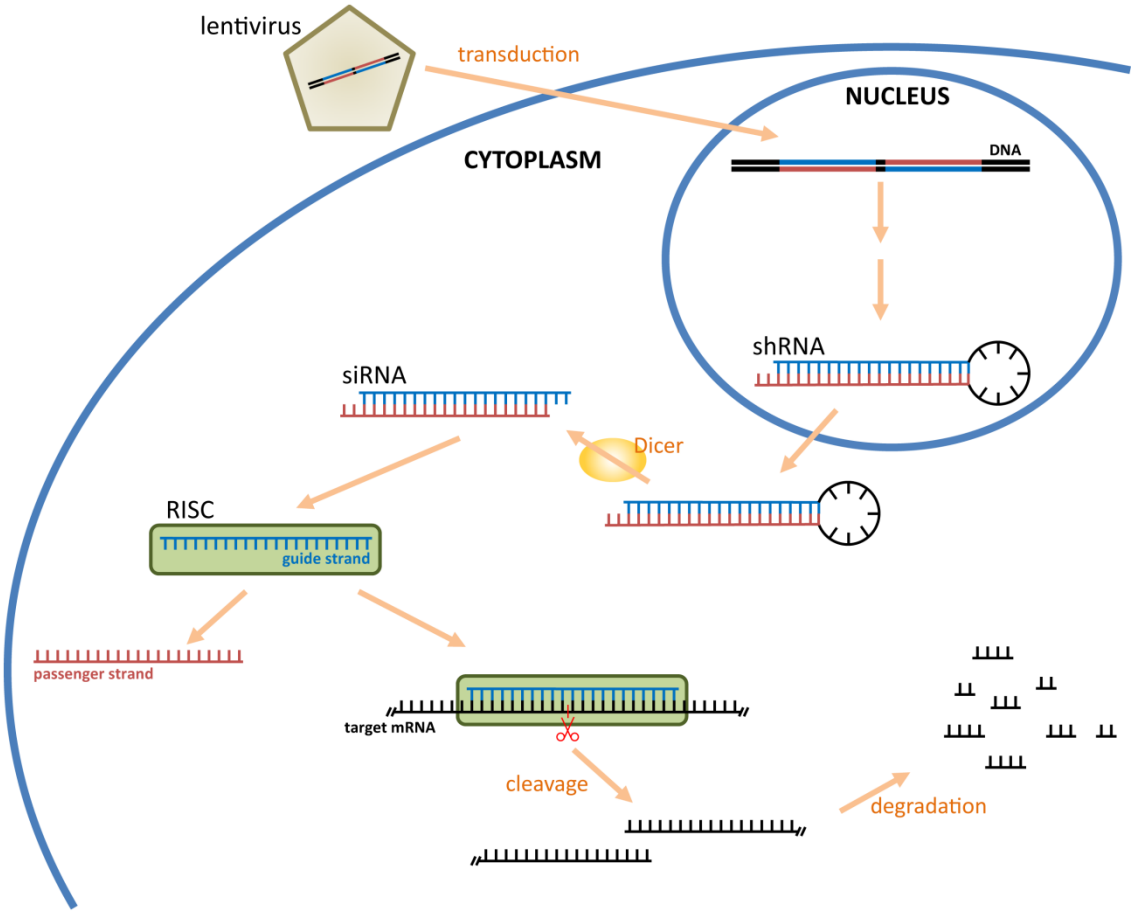

Figure 5. Pathway of RNA interference mediated by transduction of lentiviral vector coding for short-hairpin RNA.

1.10.2 Viral vectors as vehicle for *in vivo* gene delivery to the CNS

Several viral vector types have been used in a wide range of *in vivo* applications, predominantly derived from adenoviruses, adeno-associated viruses (AAV) and lentiviruses. All three vector types are capable to infect dividing and non-dividing cells and are thus suitable for transducing neurons (Lentz et al. 2012). Of these, adenoviral vectors have the highest packaging capacity of ~36 kilobase. Their viral genetic material persists in the nucleus as a linear episome which results in sustained expression and integration into the host genome is unlikely. Yet the major drawback is that they can trigger massive host immune responses against the epitopes of the adenovirus or of the helper vectors that have been used during production. A hard lesson learned from the prominent tragic case of clinical trial participant Jesse Gelsinger who died in 1999 due to massive immune response after adenoviral vector injection.

AAV are rather abundant and most mammals have been exposed and infected by AAV without symptoms. Compared to adenoviral vectors, AAV vectors have a lower risk to trigger immune responses and careful selection of the serotype can further reduce this risk and, moreover, partially direct the efficacy of infection towards certain cell types (Rabinowitz et al. 2002). In general, AAV

vector transduction efficacy is high for neurons and glial cells. Wildtype AAV generally integrate into the genome at a specific site called AAVS1 but insertional mutagenesis has been described as well (Deyle and Russell 2009). This issue is circumvented in recombinant rAAV vectors that hardly integrate in the absence of helper virus but persist as episomes in linear or circular form (Schnepp et al. 2005). Expression is persistent, yet a considerable limitation lies in their lower packaging capability of ~4.7 kilobase restricting its use to shorter sequence length. AAV vector based gene therapy trials covering a broad spectrum of neurological conditions are currently undertaken. In other therapeutic areas two AAV based *in vivo* gene therapies recently received market approvals, namely Glybera (alipogene tiparvovec), a treatment of lipoprotein lipase deficiency (LPLD) from UniQure, and Luxturna (voretigene neparvovec), adressing Leber's congenital amaurosis (LCA) from Spark Therapeutics.

Lentiviral vectors are retroviruses and those used in biomedical applications are typically derived from human immunodeficiency virus (HIV). They have the capability to efficiently infect / transduce non-dividing cells and neurons in particular (Kriebel et al. 2011; Zitman et al. 2014). Like their HIV origin, lentiviral vectors hardly trigger immune responses, and high and robust persistent expression is initiated fast after transduction. Yet, lentiviral vectors regularly integrate into the host cell genome which may have unfathomable consequences if the insertion interferes with coding sequences of the genome - in particular if oncogenes are affected. Only recently, efforts to create non-integrating lentiviral vector were fruitful which promises a great improvement. Lentiviral vectors allow a payload of ~ 8 kilobase, making them suitable for multi-gene transduction and the like. Overall, like AAV vectors, ease and safety of production, purification and handling make them preferred transduction systems for studies in basic research.

1.10.3 Methodological considerations on RNA interference

RNAi based on lentiviral vector mediated delivery of shRNA coding sequences is a strong tool to knock down a target by cleavage of the respective mRNA leading to its degradation. Nonetheless, a few caveats need to be considered:

First, direct application of siRNA has been shown to trigger innate immune responses via activation of interferon pathways resulting in a broad spectrum of adverse effects. Yet, introduction of the RNAi effector via shRNA seems to highly reduce the risk of such immune reactions and should be a minor concern in lentiviral vector / shRNA based RNAi (Ozcan et al. 2015; Sioud 2009).

Second, RNAi, in contrast to a full deletion of a gene as it is the case for knockout animals, is never a complete effector and not all sequences are equally efficient in silencing a target mRNA. Selection of the optimal shRNA / siRNA sequence can be complex and laborious (Elbashir et al. 2001c; Takasaki 2009). Nevertheless, some functional mRNA may escape RNAi and depending on its stability or on

the stability of its resultant peptide or protein some function may persist. In this case, the residual expression may be sufficiently high to counteract the goal to eliminate a certain protein and may lead to false assumptions on the function of the entity under investigation.

Third, off-target silencing has been described. Although the full siRNA guide-strand is typically designed to be complementary to a sequence of the target mRNA, some mismatch is tolerated by the RNAi cellular machinery, especially as siRNAs may act as miRNAs in some instances (Doench et al. 2003). Typically, precautions like BLAST search (U.S. National Library of Medicine) for sequence homology of the target with other non-target sites are performed in the shRNA / siRNA design and selection process to reduce this risk.

Fourth, excessive shRNA transcription may overflow the neuron's internal RNAi pathway and disturb post-transcriptional regulations by intrinsic regulatory RNAs, i.e. miRNAs, with unpredictable consequences on proper cell function (Grimm et al. 2006). This problem needs to be appreciated particularly if many functional copies of the transcript are present in one cell due to high multiplicity of infection by viral vectors. Conclusions drawn on the function of a shRNA target are thus potentially prone to misinterpretations based on manifestations of regulatory RNA malfunction.

Overall, precaution is advised when constructing RNAi effectors but awareness and appropriate measures can largely reduce non-specific and off-target effects to a high degree.

1.11 Scope

We attempted to obtain a deeper insight into the role of gap junctional coupling in the IO by following two strategies: We examined the detailed electrophysiological properties of IO neurons i) in the light of gap junctional coupling, which we suspected to be dynamically regulated in the course of the first postnatal weeks, and ii) in search for other techniques to locally alter the coupling, we performed a knockdown of Cx36 by lentiviral vector shRNA based RNA interference (RNAi).

We assessed the gap junctional coupling by neurobiotin dye-coupling and/or paired whole-cell patch clamp recordings; examined the occurrence and kinetics of regenerative events, namely spontaneous action potentials (sAP) and spikelets (sp) (Llinas et al. 1974; Llinas and Yarom 1981a); the presence, frequency and synchrony of sub-threshold oscillations (STO) (Devor and Yarom 2002b); the putative phase-locking of events to the STO (Bazzigaluppi et al. 2012; Khosrovani et al. 2007; Lampl and Yarom 1993; Llinas and Yarom 1986; Mathy et al. 2009) and whether kinetic parameters of events may encode STO features.

Moreover, we assessed free locomotion in wildtype and Cx36 knockdown rats (LV-shCx36) in order to investigate whether our approach of local Cx36 knockdown taking place later during postnatal development would reveal a more distinct phenotype than observed in the knockout mice.

2. Materials and Methods

2.1 Animals and surgery

CD rats (Charles River Laboratories, Research Models and Services, Germany GmbH, Sulzfeld, Germany) of different age were used throughout all experiments. All experimental and surgical procedures were in accordance with German law and were approved by the local animal care committee (Regierungspräsidium Tübingen). Injection of lentiviral vector solution into the inferior olive was performed at postnatal day 21 (p21) under ketamine and xylazine anesthesia (100 mg/kg and 10 mg/kg body weight, respectively). Supplemental injections were given if necessary to maintain a suitable level of anesthesia which was identified by the loss of hind limb and tail reflexes evoked by strong pinch stimulation. The animals were mounted in a stereotaxic frame and the cranial bone was exposed by a caudo-rostral skin incision. A small trepanation was performed at the horizontal coordinates corresponding to the center of the inferior olive (AP: -9.1 mm, ML: ±0.5 mm relative to bregma). Coordinates were derived from the Rat Brain Atlas (Paxinos and Watson 1998) and adapted to the younger animals by initial electrophysiological mapping. A custom designed injectrode (adapted from Tokuno et al. (1998)), built from a glass-insulated tungsten electrode with resistance ≥1 MΩ (Alpha Omega GmbH, Ubstadt-Weiher, Germany) attached to a sharp-end 30G needle on a syringe (Hamilton Bonaduz AG, Bonaduz, Switzerland), was lowered towards the dorso-ventral center of the IO while the neuronal activity was constantly monitored. The target location was identified by the characteristically low mean firing rate of IO neurons (less than 1 Hz) and the distinctive discharge of pyramidal tract fibers underneath the IO. Once in position, a volume of 2 - 5 µl lentiviral vector solution was injected at a rate of 0.5 µl/min and the injectrode was kept in place for an additional 10 minutes after the injection to allow diffusion and to minimize solution reflux along the injection tract. The wound was sutured and animals were housed individually for 4 days to allow proper recovery and to prevent opening of the suture knots by littermates. A daily dose of about 10 mg/kg carprofen (Rimadyl; Pfizer GmbH, Berlin, Germany) was administered for 2 - 3 days after surgery for analgesia and for reducing the impulse to scratch the wound.

2.2 RNA interference (RNAi)

Modified lentiviral vectors on the basis of the BLOCK-iT™ Lentiviral RNAi Expression System (Life Technologies GmbH, Darmstadt, Germany) were designed to express short-hairpin RNA sequences under the control of the human U6 promoter, and EGFP-WPRE (woodchuck hepatitis virus posttranscriptional regulatory element) under the control of the CAMKIIα promoter (pLenti-hU6-shRNA-CamKIIα-EGFP-WPRE). Three different vectors were generated: A control vector LV-shCTR with the target sequence 5'-AGACGTTTCACGTCGGAGA-3' (Burkarth et al. 2007), and two different

functional vectors LV-shCx36i and shCx36ii with the respective target sequences 5'-GCATTTGTGTGGTGCTCAATC-3' and 5'-GCTCAATCTGGCTGAACTTAA-3'. It was ensured by BLAST search (U.S. National Library of Medicine) that sequences would not have collateral targets. Titers were ~$1.7*10^7$ TU or $4.6*10^{10}$ LP measured with the QuickTiter™ Lentivirus Titer Kit (Cell Biolabs Inc., San Diego, US-CA), an ELISA for the HIV-1 p24 antigen. Prior to insertion into the lentiviral vector backbone, the RNAi efficiency of the different shRNAs was assessed with the psiCHECK™-2 Vector assay (Promega GmbH, Mannheim, Germany) which is based on the relative fluorescence intensities of a reference firefly luciferase and one expressed from a Cx36-Renilla luciferase fusion mRNA, that is degraded in relation to the RNAi efficiency of the tested shRNA. The functional constructs shCx36i & shCx36ii significantly reduced the expression of the fusion protein by RNAi to 7.32 ± 0.66 % & 10.96 ± 0.99 % respectively compared to shCTR based RNAi that maintained 90.50 ± 8.16 % of the fusion protein (mean ± SEM) ($p = 0.004$, Kruskal-Wallis).

2.3 Acute slice electrophysiology

Acute slices from brain stem were prepared from either 2 weeks (p13 - p16), 3 weeks (p20 - p23) or 5 weeks (p32 - p40) old wildtype rats or rats that had received an olivary injection with one of the two functional or with the control lentiviral vector solutions two weeks earlier (5w-shCx36 or 5w-shCTR; p33 - p36). The animals were decapitated under deep ketamine anesthesia. The brain was quickly removed and transferred to ice-cold, oxygenated (95 % O_2, 5 % CO_2) cutting artificial cerebrospinal fluid (cACSF) containing (in mM) 252 sucrose, 5 KCl, 1.25 NaH_2PO_4, 3.5 $MgSO_4$, 26 $NaHCO_3$, 10 D-Glucose, 0.5 $CaCl_2$. The pia mater and big blood vessels were removed around the brainstem with sharp forceps and coronal slices of 290 µm were cut on a microtome (VT1000S; Leica Microsystems GmbH, Wetzlar, Germany). The slices were transferred to oxygenated ACSF at room temperature containing 126 NaCl, 5 KCl, 1.25 NaH_2PO_4, 2 $MgSO_4$, 26 $NaHCO_3$, 10 D-Glucose, 2 $CaCl_2$ and kept for at least 1.5 h for recovery. Slices containing IO nuclei were transferred to a recording chamber and were continuously perfused with oxygenated, warmed ACSF (35 °C). The preparation was visualized via a motorized (Luigs and Neumann GmbH, Ratingen, Germany) microscope (Axioscope; Carl Zeiss MicroImaging GmbH, Jena, Germany) with a water-immersion objective (40x, numerical aperture: 0.75, Zeiss) and illuminated by a halogen light source (Zeiss) attached to a Dodt-Gradient-Contrast System (Luigs und Neumann), infrared filter and infrared-sensitive CCD camera (Newvicon C2400-07-C; Hamamatsu, Japan). A UV-light source (HBO50, Zeiss) and appropriate filters were used to discriminate between EGFP positive neurons that were transduced with the lentiviral constructs and EGFP negative neurons that were non-transduced. Somatic whole-cell patch clamp recordings (pairs and single) were performed with pulled glass electrodes (resistance 2 – 4 MΩ) and amplified by using two current clamp bridge amplifiers (BA-1S; NPI electronic GmbH, Tamm,

Germany). The recordings were digitized at a sampling rate of 12.5 kHz on a PC controlling a 1401plus data acquisition system and running Spike2 software (Version 7; Cambridge Electronic Design, Cambridge, UK). The intracellular solution in the patch electrode contained (in mM) 131 K-Gluconate, 5 K-HEPES, 5 NaCl, 5 EGTA, 4 K-ATP, 0.3 Na-GTP, 0.5 $CaCl_2$ adjusted to pH 7.3 with KOH. In one electrode of a pair as well as in all single recordings neurobiotin (Vector Laboratories Inc., Burlingame, US-CA) was added to the intracellular solution to reveal the transfer of this dye to neighboring neurons via gap junctions (dye-coupling) and to identify the position of the labelled neuron within the IO as well as to reveal the neuron's dendritic morphology.

The quality of the recording was assured by a stable resting potential and a high signal-to-noise ratio, indicating high seal quality. Only neurons with overshooting rebound action potentials (peak amplitude >0 mV) elicited by negative step current injections were included in the analysis.

After recording, the electrodes were carefully retracted to ensure resealing of the cell membrane and thus preserving the integrity of the soma. The slices were transferred back to oxygenated, room temperature ACSF and kept for 60 min. to allow sufficient spread of neurobiotin into the dendritic processes and to potential neighboring neurons connected by gap junctions. Thereafter, the slices of the experimental day were transferred to well plates and fixated in 4 % paraformaldehyde in 0.1 M phosphate buffer (PFA) over night and then transferred to 30 % sucrose in 0.1 M phosphate buffer (PB) for dehydration for at least two days or until the slices had sunk to the bottom of the well. Slices were either immediately stained by immunohistochemistry or stored at -80 °C for batch processing.

2.4 Data analysis

Regenerative events (sAP and sp) were detected in continuous recordings from IO neurons and their parameters (amplitude, (10 - 90 %) rise time, 10 - 90 % slope, decay time, half-width, area) were determined using Mini Analysis (Synaptosoft Inc., Fort Lee, US-NJ). Event frequencies were determined by dividing the number of detected events by the recording time. Average waveforms, dominant STO frequencies, STO synchrony, event vs. STO-phase relationships, and electrotonic coupling were analyzed and visualized in Spike2, IGOR Pro 5 (WaveMetrics Inc., Lake Oswego, US-OR) or MATLAB (The MathWorks Inc., Natick, US-MA) using custom written scripts. Data is typically presented as mean ± SEM (standard error of the mean) unless indicated otherwise.

2.5 Histology

Rats that received an olivary injection of one of the lentiviral vector solutions 3 weeks earlier were deeply anaesthetized with ketamine and transcardially perfused with ice-cold 0.1 M PB followed by ice-cold 4 % PFA for about 20 min. The brains were removed and post fixed in 4 % PFA for one day

and then dehydrated in 30 % sucrose in 0.1 M PB until they had sunk to the ground of the flask. Brains were frozen in 2-methylbutane and 35 µm slices in the coronal plane were cut from the brainstem region containing the IO on a sliding microtome (SM200R; Leica) and kept in 0.1 M phosphate buffered saline (PBS). The slices were permeabilized and blocked with 0.4 % Triton X-100 (Sigma-Aldrich Chemie GmbH, Taufkirchen, Germany), 10 % goat serum (Gibco, Life Technologies), 1 % bovine serum albumin fraction V (Carl Roth GmbH + Co. KG, Karlsruhe, Germany) in 0.1 M PBS for 3h and thereafter immunohistochemically stained over night at room temperature for microtubule-associated protein 2 (MAP2) and connexin 36 (Cx36) with the following primary antibodies: mouse anti-MAP2 (2a+2b) (1:1000; Sigma, Cat.-No M1406) and rabbit anti-Cx36 (1:125; Zymed, Life Technologies, Cat.-No. 51-6200). After washing in 0.1 M PBS the slices were incubated for 3h with the following secondary antibodies: goat anti-mouse IgG (H+L) Cy5 conjugate and goat anti-rabbit IgG (H+L) Cy3 conjugate (1:500 each; both Zymed, Life Technologies, Cat.-Nos. 81-6516 and 81-6115, resp.).

Slices from patch-clamp recordings were stained according to the same protocol mentioned above with the primary antibody mouse anti-MAP2 (2a+2b) and secondary antibody goat anti-mouse IgG (H+L) Cy5 conjugate as well as neurobiotin binding Alexa Fluor 555 conjugated streptavidin (1:500; Life Technologies, Cat.-No. S32355) to stain for neurobiotin filled structures.

All immunostained brain slices were covered in Fluorescent Mounting Medium (Dako Deutschland GmbH, Hamburg, Germany) and multi-fluorescence 3D image stacks were obtained using a confocal laser scanning microscope (LSM 510 Meta; Zeiss). The point spread of the fluorescence signals within these image stacks was reduced by software based deconvolution in AutoQuant (Media Cybernetics Inc., Bethesda, US-MD).

The obtained 3D stack images of the IO were processed and analyzed in ImageJ (NIH, Bethesda, US-MD) and Imaris (Version 7; Bitplane AG, Zurich, Switzerland). For determining Cx36 expression and knockdown, sub-volumes were generated by co-localization of either MAP2 stained structures and lentivirally transduced structures that were EGFP positive, or by co-localization of MAP2 stained structures and EGFP negative structures. The obtained sub-volumes, named “transduced” and “non-transduced”, resp., were used as masks for the discrimination of the Cx36 associated immunofluorescence. Cx36 spots were then detected and examined in these two sub-volumes employing the built-in Imaris spot detection module with identical detection criteria applied to the sub-volumes. For dye-coupling, Alexa Fluor 555 positive somata were reconstructed plane-wise by semi-automatic “magic-wand” edge discrimination under visual inspection (IMARIS). Relative intensities were determined, and Euclidian distances of the soma centers to the primary neuron were calculated by ImarisXT and supplied MATLAB routines.

2.6 Locomotion analysis

Locomotion was recorded and analyzed on an automated system (CatWalk; Noldus Information Technology BV, Wageningen, NL) detecting the spatial and temporal dynamics of the limb contact with a side-illuminated glass walkway via a high-speed CCD camera underneath. Briefly, in the dark, animals were placed on one end of the walkway and had to walk freely the full length towards the other side where a food reward was offered (Dein Bestes, Drop-Mix; dm-drogerie markt GmbH + Co. KG, Karlsruhe, Germany). Three habituation and training days preceded a test day. Data was averaged from 3 continuous runs of one session. Data from individual paws of an animal was pooled for the parameters stand, swing & cycle time, swing speed, stride length and mean print area. Moreover, the parameters couplings (diagonal, girdle & ipsilateral), base of support, step regularity index and cadence as well as support pattern and step sequence were analyzed.

2.7 Statistics

Statistical analysis was performed using standard software packages SPSS (IBM, Armonk, US-NY) for Fisher's exact test and SigmaStat/Plot (Systat Software Inc., San Jose, US-CA) for (paired) two-tailed Student's t-test, Mann–Whitney U test (MWU), one-way ANOVA (followed by Tukey's post-hoc multiple comparison), Kruskal-Wallis ANOVA on Ranks (and Dunn's post-hoc multiple comparison) unless otherwise stated. The CircStat MATLAB circular statistics toolbox (Berens 2009) was utilized where circular statistics were appropriate. Experimental values are either presented as mean ± standard error for Gaussian distributed data or as median (25 % - 75 % percentile) for non-Gaussian distributed data unless otherwise stated. Box plots around the median span from the 25^{th} to the 75^{th} percentile (Q1 - Q3) flanked by whiskers extending from 10^{th} - 90^{th} percentile. Additionally dots indicate the 5^{th} and 95^{th} percentile and red dashed lines represent means. Statistical significance is indicated as *p<0.05, **p<0.01, ***p<0.001.

3. Results

Aiming for a better understanding of the relevance of gap junctional coupling for the function of the IO we employed wildtype (WT) rats of either two (2w), three (3w) or five (5w) weeks of age, as well as 5 weeks old rats where gap junction expression was manipulated by RNAi (5w-shCx36) or their respective controls (5w-shCTR). In the latter two groups, two weeks prior to assessment, rats received olivary injections of lentiviral vectors coding either for functional short-hairpin RNA (LV-shCx36) to knock down connexin 36 (Cx36) or for a non-functional control (LV-shCTR). Whole-cell patch clamp recordings were performed on single neurons and on pairs of neurons in acute slices from animals of the subject groups. In the context of the degree of gap junctional coupling, we investigated the presence and properties of spontaneous action potentials and spikelets in IO neurons across the age and treatment groups. Moreover, we examined the occurrence and synchrony of sub-threshold oscillations (STO) and explored the relationship of occurrence and properties of spontaneous action potentials or spikelets with the phase or amplitude of STO. Last, we assessed free locomotion in 5 weeks old WT, LV-shCx36 or LV-shCTR rats to gain insight into possible implications of RNAi mediated uncoupling of olivary neurons on motor coordination.

3.1 Spontaneous activity is altered during postnatal maturation

We examined the spontaneous activity in IO neurons from postnatal week 2, 3 & 5 WT and 5w-shCx36 rats by measuring the incidence probability, the frequencies and the detailed properties of two spontaneous regenerative event types: spontaneous action potentials (sAP) and spikelets (sp).

3.1.1 Spontaneous activity and membrane excitability

We found that the majority of IO neurons of postnatal week 2 (2w) rats were not spontaneously active at all: 50 % (9/18) of recorded IO neurons were silent throughout the recording, whereas 33 % (6/18) showed only sp and 17 % (3/18) showed sAP & sp, no neuron showed only sAP. In contrast, neurons from postnatal week 3 (3w) rats were more likely to exhibit regenerative events: only 13 % (2/15) were silent and the majority of neurons showed either only sp (27 %, 4/15) or sAP & sp (60 %, 9/15), no neuron showed only sAP. The contingencies of events were significantly different between 2w and 3w ($p = 0.022$, Fisher's exact test).

To our surprise we again found a lower probability to observe regenerative events in neurons from postnatal week 5 (5w) rats: 54 % (23/43) of neurons were silent, 21 % (9/43) showed only sp and 23 % (10/43) showed sAP & sp. We also observed one case (2 %) with sAP but no sp. The contingencies of events were significantly different between 3w and 5w ($p = 0.017$, Fisher's exact test). To test whether the degree of electrotonic coupling would influence the occurrence of

regenerative events, we examined the situation in neurons of 5 weeks old rats in which gap junctional coupling via Cx36 had been knocked down by RNAi (5w-shCx36): we found that more neurons were spontaneously active compared to the 5w group. Only 30 % (7/23) of neurons were silent, 26 % (6/23) showed only sp and 35 % (8/23) showed sAP & sp. Moreover, 9 % (2/23) showed sAP but no sp. Yet, despite the increased activity seen in the 5w-shCx36 group, contingencies of events between 5w and 5w-shCx36 did not significantly differ (p=0.226, Fisher's exact test) (**Figure 6A**).

In general, frequencies of sAP were low in IO neurons from all WT age groups and also in the case of RNAi induced uncoupling. Whereas we could not find significant differences (p = 0.372, Kruskal-Wallis (KW)), we could observe a tendency for lower mean sAP frequencies in neurons from 2w and 5w rats (0.0046 ± 0.0026 Hz, n = 3 and 0.0079 ± 0.0039 Hz, n = 11, resp.) and for higher mean sAP frequencies in neurons from 3w rats (0.0206 ± 0.0128 Hz, n = 9). In line with this observation sp mean frequencies, albeit also not significantly different among the groups (p = 0.08, KW), were also lower in neurons from 2w and 5w rats (0.0120 ± 0.0054 Hz, n = 9 and 0.0114 ± 0.0054 Hz, n = 19, resp.) and higher in neurons from 3w rats (0.0350 ± 0.0143 Hz, n = 13) (**Figure 6B**).

The interrelation of sAP and sp frequencies in the WT age groups becomes more obvious when plotted against each other (**Figure 6C and D**). In neurons from 2w and 5w rats the mean sAP frequencies were lower than in neurons from 3w rats and so where the mean sp frequencies (**Figure 6C**).

Moreover, neuron-by-neuron based Pearson correlation of sAP and sp frequencies for each age group (the respective fraction of neurons where sp & sAP could be observed) revealed that in 5w (r = 0.72, p = 0.019, n = 10) but not earlier (2w: r = 0.32, p = 0.795, n = 3; 3w: r = 0.1, p = 0.805, n = 9) sAP and sp frequencies were significantly correlated (**Figure 6D**). In the wildtype, recording of sp in IO neurons from 5w rats may therefore serve as a reliable predictor of local sAP activity.

After uncoupling, albeit not significantly different, the mean sAP frequency was found to be higher in 5w-shCx36 neurons (0.0220 ± 0.0171 Hz, n = 10), resembling and even exceeding the activity seen in 3w neurons. Interestingly this higher sAP activity was not translated into higher sp activity which, in contrast, was lower (0.0087 ± 0.0028 Hz, n = 14) than in any WT group (**Figure 6B**) and compared to their 5w WT counterpart, the uncoupled neurons did not show a linear relationship between sAP and sp mean frequencies any more (**Figure 6C**), nor did the individual neuron-by-neuron analysis of sAP and sp frequencies identify any significant correlation (r = 0.3, p = 0.47, n = 8) (**Figure 6D**).

What may be the basis of the dynamical change in spontaneous activity that we could observe? To address this question we looked at the averaged VI-curves of neurons from the four different groups. The VI-curves were obtained by fitting sigmoidal regression models (and their 95 %

prediction boundaries) to the steady response voltage deflections elicited by series of rectangular current pulse injections of increasing amplitude (-100 to 100 pA, 10 pA steps) into the whole-cell recorded neurons (**Figure 7**). We observed a general and dynamical change of membrane excitability during postnatal development and after uncoupling.

Quite intriguing, the excitability was highest in the 2w group and decreased in the course of maturation (3w and 5w), evident by flattening of the VI-curves. Uncoupling (5w-shCx36) on the other hand led to an increased excitability and resulted in a VI-curve largely identical to the one found for 3w neurons. It revealed that at 2w neurons were per se highly excitable but this did not translate into high sAP or sp activity. On the other hand, the neurons at 3w were less excitable than at 2w but nevertheless exhibited high sAP and sp activity. At 5w excitability was lower than in all the other examined groups and congruently sAP and sp activity was low. In contrast, uncoupled 5w-shCx36 neurons increased their sAP frequency which went along with an increased excitability while their sp frequency was the lowest observed across the groups.

Taken together we conclude that the spontaneous activity is dynamically altered during the first postnatal weeks and shows a maximum around postnatal week 3 followed by a subsequent reduction by postnatal week 5. Uncoupling of neurons by RNAi increases spontaneous activity and disrupts the close relationship between sAP and sp frequencies observed in the age matched WT group. Uncoupling moreover leads to changes in the membrane excitability resembling the excitability observed in younger animals.

Results

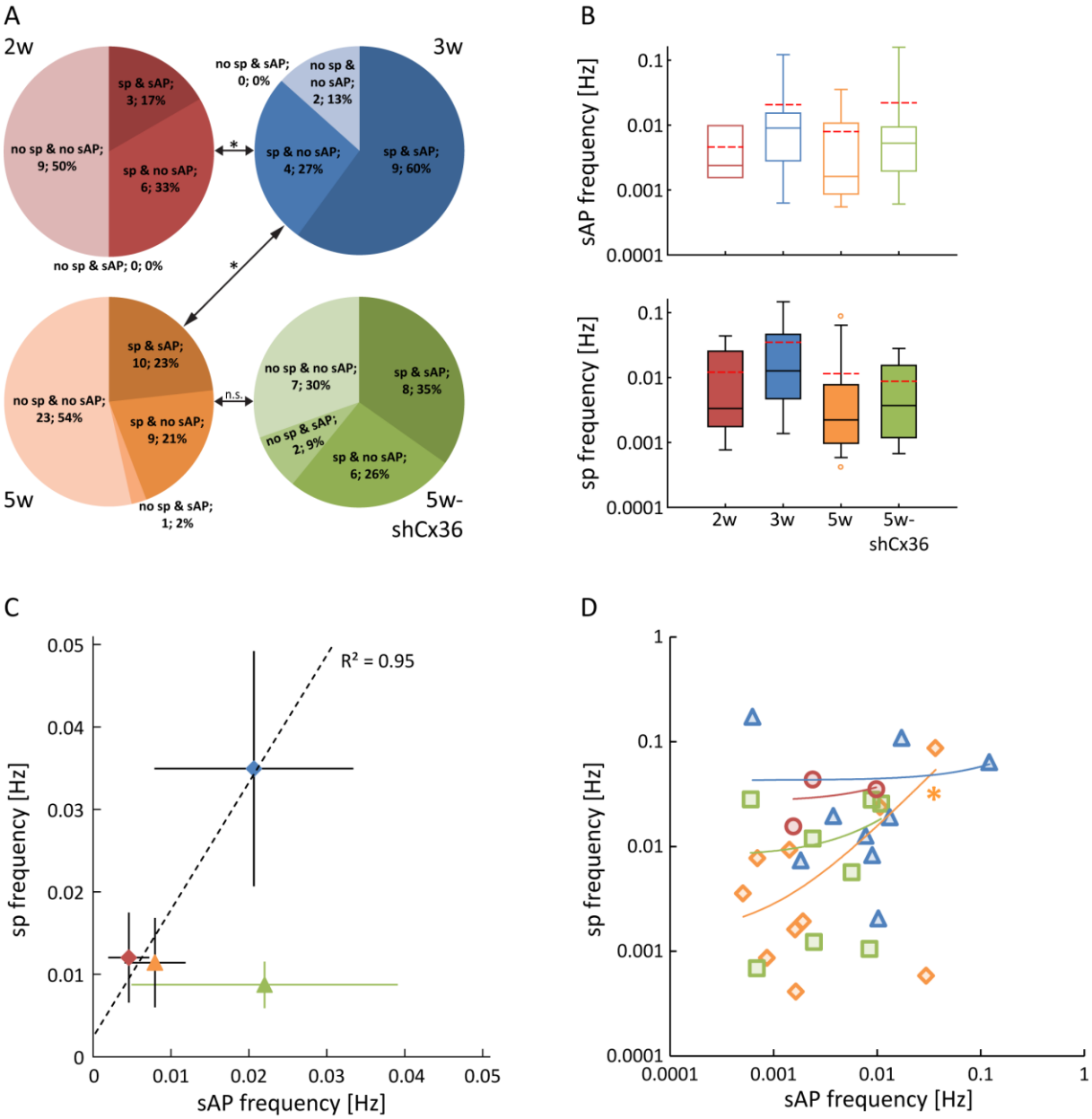

Figure 6. Probability and frequency of regenerative events (spontaneous action potentials (sAP) and spikelets (sp)) change during maturation.
A Absolute numbers of neurons and the respective probabilities in percent to observe sAP and/or sp during recordings from neurons of the different age or treatment groups investigated. Neurons from 2 and 5 week old animals (2w and 5w) showed a low probability of regenerative events, whereas higher event probabilities were observed in neurons from 3 week old animals (3w) - and to some extent also in neurons from 5w-shCx36 animals (*$p < 0.05$, Fisher's exact test). **B** Corresponding regenerative event frequencies for the different age groups. sAP and sp frequencies were changing in a similar fashion in the course of maturation, yet uncoupling led to an increase of sAP but not sp frequency. **C** sp vs. sAP mean frequencies for the different age or treatment groups. Black dashed line, linear regression for the means of the WT groups. Error bars indicate SEM. **D** Significant correlations of sp & sAP frequencies within the groups could only be found in the more mature 5w group (*$p < 0.05$, Pearson correlation). Colors: red, postnatal week 2 (2w); blue, week 3 (3w); orange, week 5 (5w); green, week 5 and knockdown of Cx36 (5w-shCx36).

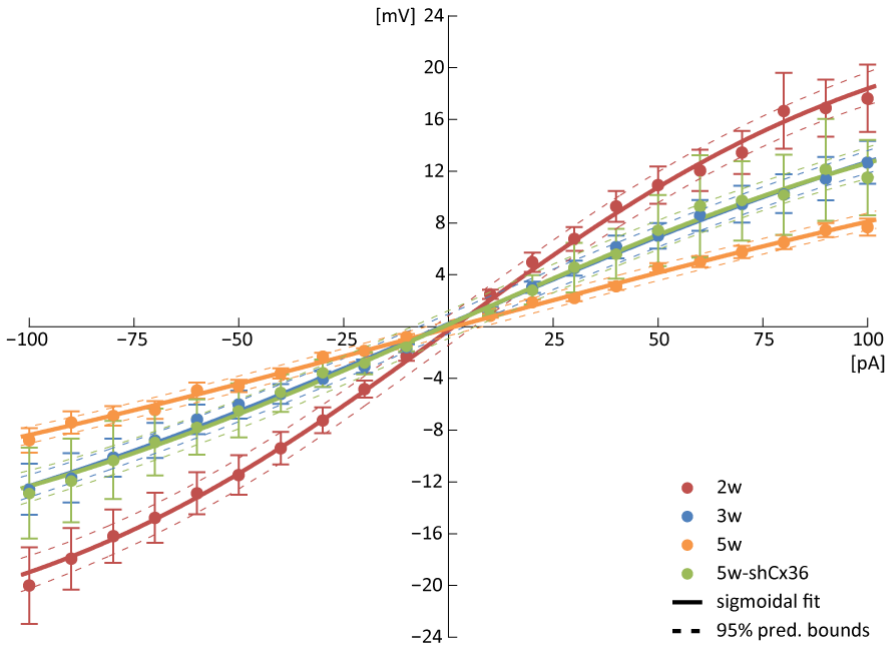

Figure 7. Voltage-current relationship (VI-curves) obtained from neurons of the different age groups and after Cx36 knockdown.
VI-curves generated from steady-state voltage deflections elicited by rectangular current pulse injections of -100 to 100 pA in 10 pA steps. While the VI-curves became more flat in the course of maturation, Cx36 knockdown led to a steeper curve largely identical to the one of 3w animals. Each data point represents mean ± SEM. Each series was fitted by a sigmoidal function. Dashed lines: 95% prediction bounds. Colors: red, postnatal week 2 (2w); blue, week 3 (3w); orange, week 5 (5w); green, week 5 and knockdown of Cx36 (5w-shCx36).

3.1.2 Kinetics of regenerative events

We further examined the properties of regenerative events in neurons from the three WT age groups and from the uncoupled 5w-shCx36 neurons to get a better understanding of possible changes in their kinetics. As shown in **Figure 8**, the grand averages of sAP and sp from the different groups make evident that substantial changes occur during development or after RNAi mediated uncoupling. Assessing the *amplitude* as well as the components of the depolarizing and repolarizing phase of sAP and sp in more detail, we found that the kinetic parameters exhibited a rather complex picture for both event types (**Figure 9**).

In general, we observed that the sAP *amplitude* significantly increased with age (2w, 3w, 5w vs. each other: all $p < 0.05$, KW) and the depolarization became faster by 5w as *rise time* & *10 - 90 % rise time* significantly decreased and the *10 - 90 % slope* significantly increased (each: 2w vs. 3w: ns; 2w or 3w vs. 5w, $p < 0.05$, KW). The repolarization phase also became faster between 3w and 5w. The *decay time* was similar in neurons from 2w and 3w but significantly shorter in 5w. The *half-width* was also similar in 2w and 3w but significantly narrower in 5w (each: 2w or 3w vs. 5w: $p < 0.05$, KW). Interestingly, the "long" 75 % quartile as well as the grand average of waveforms (**Figure 8**) indicate that a great proportion of sAPs from 3w had much longer *decay times*, which likely reflect sAP with

long after-depolarization (ADP) (Llinas and Yarom 1981a). In accordance, the *area* was significantly larger in 3w than in 5w, yet similar to 2w (2w or 3w vs. 5w: $p < 0.05$, KW) (**Figure 9A**).

A similar picture could be drawn for sp kinetic parameters. The *amplitude* also significantly increased with age (2w, 3w, 5w vs. each other: all $p < 0.05$, KW). Like for sAP, the depolarization of sp also became faster with age, but the major change seemed to have happened between postnatal weeks 2 and 3. The *rise time* significantly decreased between 2w and 3w (2w vs. 3w or 5w: $p < 0.05$; 3w vs. 5w: ns, KW) & *10 - 90 % rise time* significantly decreased as well (2w, 3w, 5w vs. each other: all $p < 0.05$, KW). Congruently, the *10 - 90 % slope* significantly increased from 2w to 3w but stayed at the same level at 5w (2w vs. 3w or 5w: $p < 0.05$; 3w vs. 5w: ns, KW). The repolarization phase also became faster in the course of postnatal development. The *decay time* was found to be similar in 2w and 3w and significantly decreased in 5w (2w vs. 3w: ns; 2w or 3w vs. 5w: $p < 0.05$, KW), while the *half-width* constantly decreased with age (2w, 3w, 5w vs. each other: all $p < 0.05$, KW). The *area* significantly increased from 2w to 3w and significantly decreased in 5w to the lowest value measured (2w, 3w, 5w vs. each other: all $p < 0.05$, KW), indicating that features of sAP like the longer ADP at 3w that led to longer *half-width* and larger *area* might be reflected in the observed larger *area* of sp (**Figure 9B**).

To investigate whether gap junctional coupling had an impact on sAP or sp properties, we analyzed the same parameters in 5w-shCx36 IO neurons. In uncoupled 5w-shCx36 neurons sAP *amplitudes* were significantly smaller than in 5w and similar to 2w and 3w and the *rise time* was significantly longer than in 5w and similar to 2w and 3w (each: 5w vs. 5w-shCx36: $p < 0.05$; 2w or 3w vs. 5w-shCx36: ns, KW). Yet, *10 - 90 % rise time* & *10 - 90 % slope* were unchanged in respect to 5w and consequently significantly shorter / higher (resp.) than in 2w and 3w. Likewise the *decay time* was unchanged in respect to 5w hence also significantly shorter than 2w and 3w (each: 2w or 3w vs. 5w-shCx36: $p < 0.05$; 5w vs. 5w-shCx36: ns, KW). In contrast, the *half-width* was significantly wider compared to 5w but still significantly narrower than in 2w and 3w (2w, 3w or 5w vs. 5w-shCx36: all $p < 0.05$, KW). The *area* was not different from 5w and significantly smaller than in 2w and 3w (2w or 3w vs. 5w-shCx36: $p < 0.05$; 5w vs. 5w-shCx36: ns, KW) (**Figure 9A**).

The spikelets, albeit at lower frequency but still found in 5w-shCx36 neurons (**Figure 6A, B**), had a significantly higher *amplitude* than in 2w, 3w, or 5w (2w, 3w or 5w vs. 5w-shCx36: all $p < 0.05$, KW). The depolarization was even faster as rise time & 10 - 90 % rise time were significantly lower and *10 - 90 % slope* was significantly higher than in any other group (each: 2w, 3w or 5w vs. 5w-shCx36: all $p < 0.05$, KW). *Decay time* and *half-width* were not different from 5w and therefore also significantly smaller than in 2w and 3w (each: 2w or 3w vs. 5w-shCx36: $p < 0.05$; 5w vs. 5w-shCx36:

ns, KW). The *area* was significantly larger than in 5w, likely due to the higher *amplitude*, but also significantly smaller than in 2w or 3w (2w, 3w or 5w vs. 5w-shCx36: all $p < 0.05$, KW) (**Figure 9B**).

Over all, we found a speed-up of sAP waveforms and faster kinetics during postnatal maturation and saw the same dynamics in sp (**Figure 8**). Despite uncoupling we still saw spikelets but their properties did not necessarily modulate in the same way as the spontaneous action potentials did.

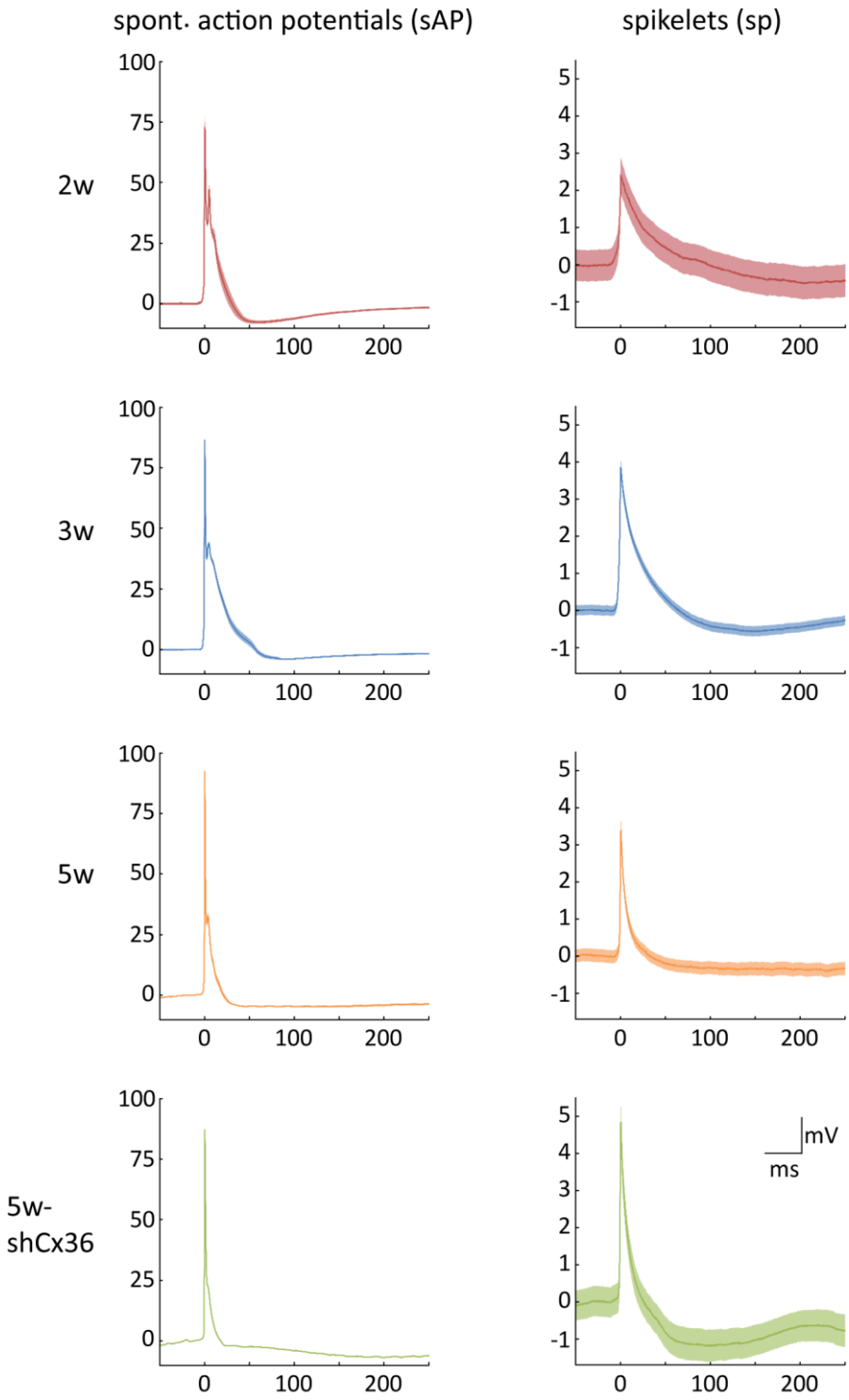

Figure 8. Grand averages of sAP and sp waveforms.
During maturation sAP *amplitudes* (left column) increased and the depolarizing plateau (likely calcium current mediated) became shorter. Secondary peaks reflect *wavelets* present in some sAP. *Amplitudes* of sp were highest at 3w and repolarization became faster during maturation (right column). Uncoupling decreased sAP *amplitude* but increased sp *amplitude*. Colors: red, postnatal week 2 (2w); blue, week 3 (3w); orange, week 5 (5w); green, week 5 and knockdown of Cx36 (5w-shCx36).

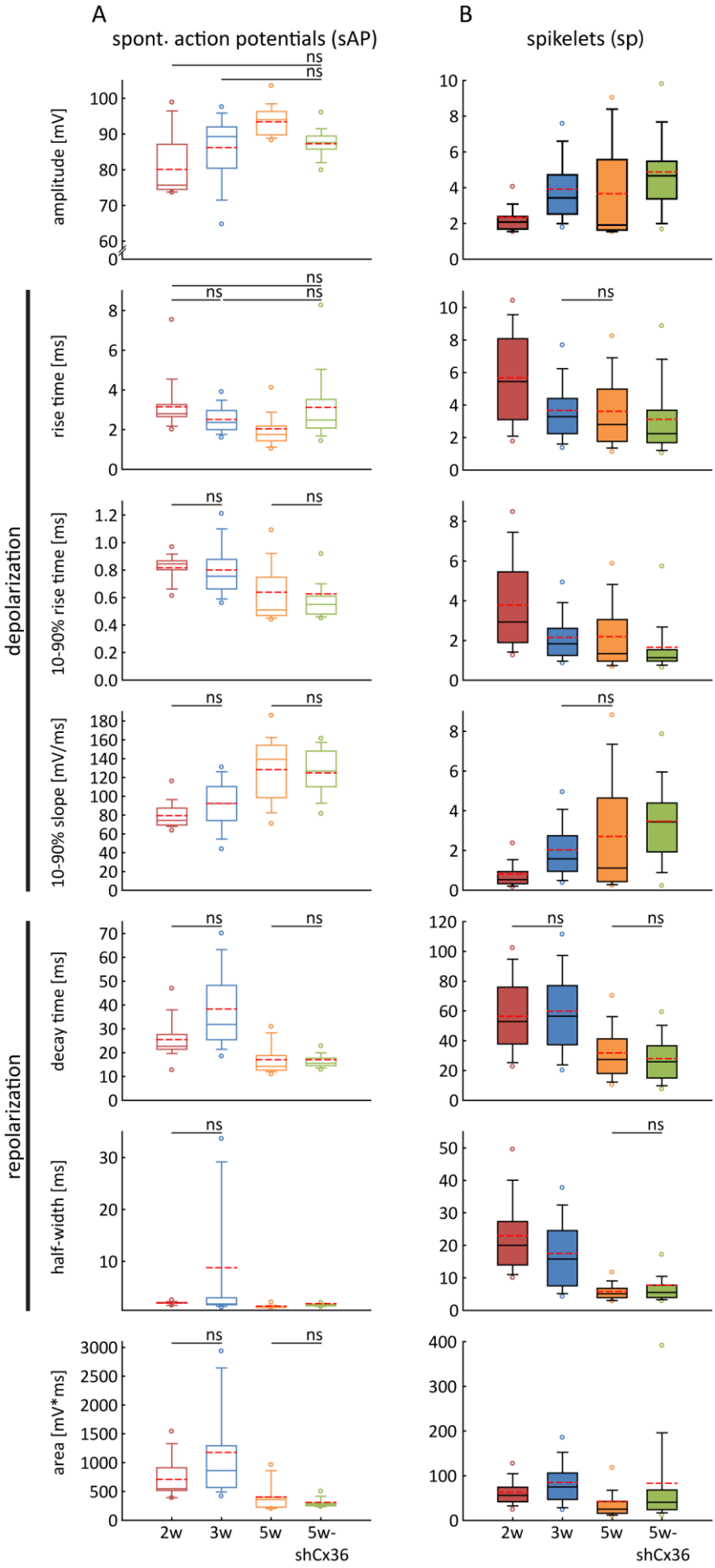
A
spont. action potentials (sAP)
B
spikelets (sp)
depolarization
repolarization
amplitude [mV]
rise time [ms]
10-90% rise time [ms]
10-90% slope [mV/ms]
decay time [ms]
half-width [ms]
area [mV*ms]
ns
2w
3w
5w
5w-shCx36

Figure 9. Kinetics of spontaneous regenerative events.
A Spontaneous action potential (sAP) *amplitudes* increased during maturation and de- as well as repolarization became faster, reflected in the parameters *10 - 90 % rise time* and *10 - 90 % slope*, or *decay time* and *half-width*, respectively. Notably, greater variabilities in *decay time* and more so in *half-width* and *area* in the 3w group originate from a fraction of sAP with long depolarization plateaus. Cx36 knockdown led to significantly lower sAP *amplitudes* but had only modest impact on the kinetics (significantly increased *half-width*). **B** Spikelet (sp) *amplitudes* increased during maturation and de- as well as repolarization became faster in congruence with the sAP dynamics seen in A. Cx36 knockdown led to significantly higher sp *amplitudes*, and thus to significantly higher *area*, but to faster depolarization without affecting the repolarization phase. Bars indicate non-significance (ns), missing bars indicate $p < 0.05$. Colors: red, postnatal week 2 (2w); blue, week 3 (3w); orange, week 5 (5w); green, week 5 and knockdown of Cx36 (5w-shCx36).

3.2 Gap junctional coupling

We examined dye-coupling during the first postnatal weeks and assessed dye-coupling and electrotonic coupling in 5w and 5w-shCx36 or 5w-shCTR IO neurons.

3.2.1 Dye-coupling

We examined the extent of gap junctional coupling in neurons of rat acute slice preparations from postnatal week 2, 3 & 5 and in 5w-shCx36 or 5w-shCTR neurons by filling one IO neuron of each recorded pair or every single recorded neuron with neurobiotin which is known to diffuse to neighboring neurons if they are connected by functional gap junctions (Devor and Yarom 2002a; Vaney et al. 1998).

Following immunohistology, we took image stacks of the primary neurons and the surrounding volume with a confocal laser scanning microscope. If labeled, we reconstructed the somata of the secondary neighboring neurons and assessed their mean labeling intensity and the Euclidian distance of their soma center from the soma center of the primary neuron as illustrated in the examples in **Figure 10A**.

Interestingly, no case of dye-coupling could be observed in neurons from 2w rats (0/13). In contrast, in 3w rats we found 63.6 % (7/11) of primary neurons being surrounded by secondary labeled neighboring neurons. In neurons from 5w rats, however, only 21.4 % (3/11) of filled primary neurons showed dye-coupling. In 5w-shCx36 neurons the dye-coupling was further reduced to only 8.3 % (1/12) compared to 16.7 % (1/6) of neurons from the 5w-shCTR control animals. The residual dye-coupling might be explained to occur through some persisting Cx36-channels still present due to residual expression after exploiting RNAi (a typical constraint of the technique). In line with the incidence rate of dye-coupling, we could observe differences in the mean number of dye-coupled neurons per case. At 3w when the coupling probability was highest, we also found the largest extent of the coupled clusters with 4.1 ± 1.2 secondary neurons. The extent dropped to 2.0 ± 0.6 secondary neurons in 5w animals and was even less (1 secondary neuron) in the only 5w-shCx36 neuron that

showed dye-coupling but was higher in the one case of dye-coupling we found in a 5w-shCTR neuron (5 secondary neurons) (**Figure 10B**).

We also found somewhat higher mean labeling intensities in secondary neurons of 5w rats compared to 3w (688 ± 184 a.u., n = 6 vs. 317 ± 48 a.u., n = 29, resp.), to 5w-shCx36 (37 a.u., n = 1) , or to 5w-shCTR (124 ± 40 a.u., n = 5), indicating that even if the size of the coupled cluster may be smaller in 5w neurons, coupling among members of the cluster may be stronger than at 3w or after uncoupling (**Figure 10C**).

The medians of the distance between the primary and secondary neurons were similar among the groups (p = 0.203, KW) (**Figure 10D**).

Moreover, the mean intensity of the labeling did not significantly correlate with the distance from the primary neuron soma center in neither of the groups (3w: r = -0.11, p = 0.57, n =29; 5w: 0.02, p = 0.973, n = 6; 5w-shCx36: not enough data points, n = 1, 5w-shCTR: r = -0.45, p = 0.446, n = 5; Pearson correlation).

Our observations indicate changes in the degree of coupling within the first postnatal weeks with a sudden onset of dye-coupling between postnatal week 2 and 3. After high coupling around postnatal week 3, an apparent decline in coupling incidences and in the extent of the coupled clusters could be observed. Manipulation of Cx36 expression had modest effects on the already low degree of dye-coupling (number of coupled neurons) at postnatal week 5 and low amounts of dye passing through the few remaining gap junctions may have fallen below the detection limits.

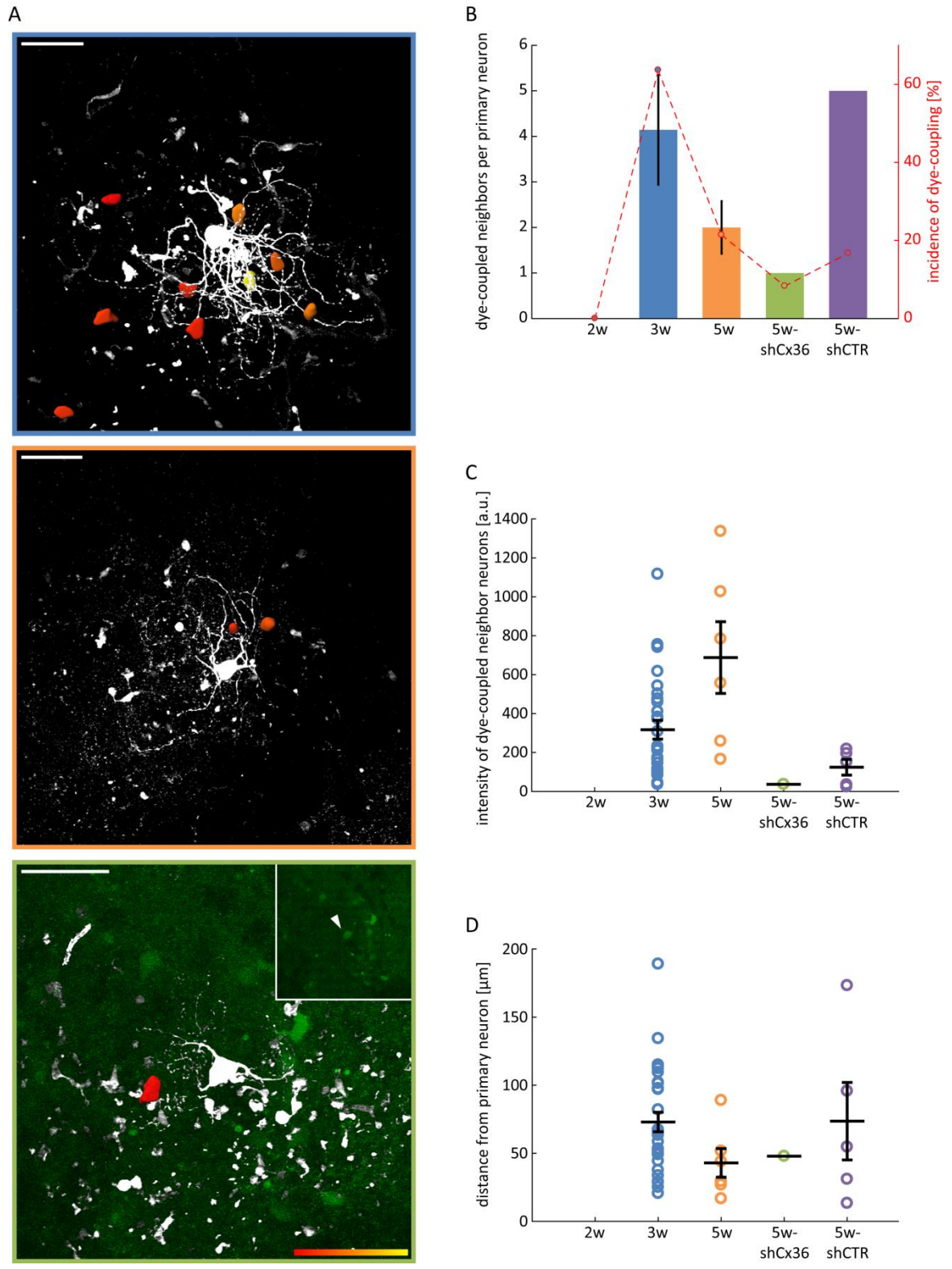

Figure 10. Neurobiotin dye-coupling of IO neurons.
A Three examples of IO neurons filled with neurobiotin during whole-cell recording (white), and reconstructed somata of dye-coupled neighboring neurons. Examples from 3w (top), 5w (middle) and after Cx36 knockdown, 5w-shCx36 (bottom); inset: GFP fluorescence alone, verifying the positive transduction of the recorded neuron (arrowhead). Intensity heat-map: red (low) to yellow (high), a.u.; scale bars 50 µm. **B** Number of dye-coupled neighboring neurons per recorded and neurobiotin filled IO neuron (mean ± SEM) as well as incidence of dye-coupling in percent of filled neurons (red dashed line). **C** Intensity of somatic neurobiotin in dye-coupled neighboring neurons. **D**, soma-somatic distance between dye-coupled neighboring and primary neurons (black bars: mean ± SEM). Colors: blue, week 3 (3w); orange, week 5 (5w); green, week 5 and knockdown of Cx36 (5w-shCx36); purple, week 5 and control vector (5w-shCTR).

3.2.2 Electrotonic coupling

To assess the degree of electrotonic coupling, we performed whole-cell current clamp recordings of pairs of IO neurons in acute slices from 5w rats and from rats that received a local olivary injection of one of the lentiviral vector constructs at p21 (5w-shCx36i, 5w-shCx36ii, 5w-shCTR) (**Figure 11A**).

Injections of negative rectangular current pulses into the primary neuron of a patched pair from 5w rats resulted in its hyperpolarization - most often with a prominent initial sag followed by a steady hyperpolarization that lasted for the duration of the current pulse (300 ms). Thereafter, most often rebound Ca^{2+}-depolarizations were observed that triggered (sodium current) action potentials depending on their strength (Llinas and Yarom 1981b). In the coupled secondary cell current-flow through open functional gap junctions led to similar yet attenuated membrane potential changes – a steady hyperpolarizing junctional potential lasting as long as the current injection in the coupled primary neighbor was followed by a depolarizing junctional potential (DJP) at the rebound. In contrast, if any, only highly attenuated changes in membrane potential in the secondary neurons could be observed in pairs with at least one 5w-shCx36 neuron indicating strong uncoupling by Cx36-specific RNAi (**Figure 11B**).

Electrotonic coupling via gap junctions was determined by reciprocal measurements of the ratios of steady voltage deflections in the primary and secondary neuron after current injection into the primary neuron - yielding two directional coupling coefficients (CC [%]) per pair (**Figure 11C & D**). Uncoupling by RNAi significantly reduced the electrotonic coupling among coupled pairs by ~70 %. On average, pairs with at least one 5w-shCx36 neuron had significantly lower CCs compared to neuron pairs from 5w WT (mean: 0.44 ± 0.08 % (median: 0.39, 0.14 - 0.63 %), n = 22 vs. 1.43 ± 0.31 % (1.6, 0.38 - 1.91 %), n = 16, resp., p = 0.01), or compared to pairs with at least one 5w-shCTR neuron (1.64 ± 0.44 % (1.89, 0.38 - 2.84 %), n = 10, p = 0.007). No significant differences between the CCs of 5w WT and 5w-shCTR could be detected (p = 0.856, ANOVA & Tukey's post-hoc multiple comparison) (**Figure 11C**).

Moreover, we could not see any dependency of the coupling strength on the soma-somatic distance between the members of the pair in 5w (r = -0.26, p = 0.327, n = 16), or 5w-shCx36 (r = -0.24, p = 0.275, n = 22) but a significant negative correlation in 5w-shCTR (r = -0.86, p = 0.001, n = 10). The mean distances between neurons were 5w: 22.6 µm (range: 9.3 - 38.1 µm), 5w-shCx36: 23.4 µm (9.9 - 44 µm), 5w-shCTR: 26.2 µm (13.3 - 40.0 µm) (**Figure 11D**).

Resting membrane potentials were stable during development (2w: -50.6 ± 0.6 mV, n = 18; 3w: -50.3 ± 0.9 mV, n = 15; 5w: -50.3 ± 0.7 mV, n = 43) and neither transduction with the functional nor with the non-functional lentiviral construct had any impact (5w-shCx36: -50.7 ± 1.2 mV, n = 23; 5w-shCTR: -50.5 ± 1.1 mV, n = 11) (**Figure 11E**).

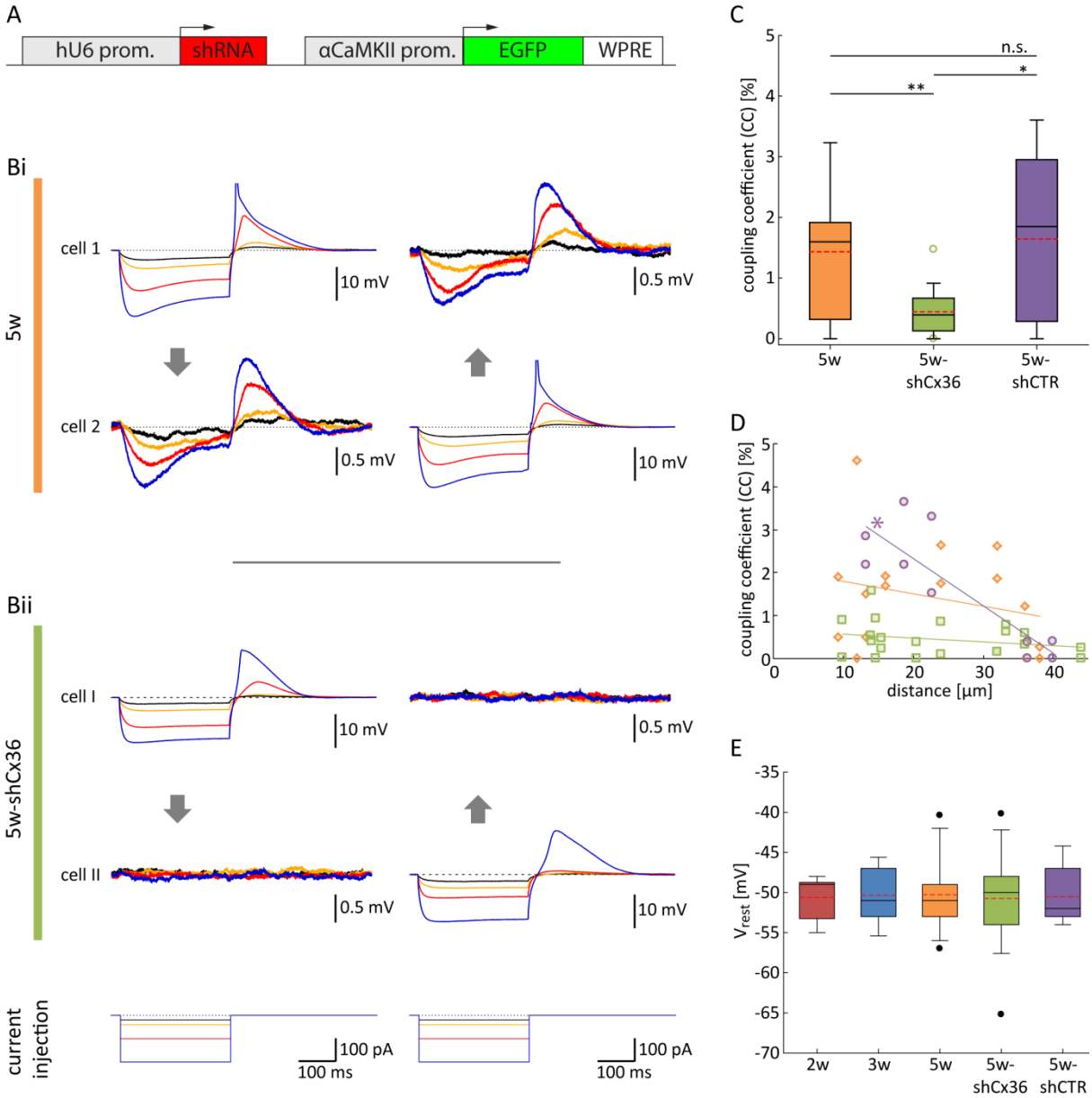

Figure 11. Local knockdown of connexin 36 in the inferior olive.
A Lentiviral vector construct. The respective shRNA (shCx36 or shCTR) driven by the human U6 promoter (hU6), and the reporter EGFP driven by the CaMKIIα promoter (pLenti-hU6-shRNA-CamKIIα-EGFP-WPRE) were brought to expression in IO neurons by local *in vivo* stereotaxic microinjection. **B** Examples of electrotonic coupling of neighboring pairs of simultaneously whole-cell recorded IO neurons, 5w WT pair (Bi) or 5w-shCx36 knockdown pair (Bii). Hyperpolarizing current steps (lower section) were injected to one neuron at a time and the voltage deflections in both cells were recorded. **Bi** In the 5w WT neuron pair gap junction mediated electrotonic coupling was evident by voltage deflections in the secondary neuron. **Bii** In the pair with one 5w-shCx36 neuron (cell I) no such deflections in the secondary cell could be recorded. Grey arrows indicate direction of current flow expected from presumed presence of functional gap junctions. **C** Coupling coefficients (voltage deflection in the secondary neuron divided by the deflection in the primary neuron at -100 pA current injection into the primary neuron) of pairs with a 5w-shCx36 neuron were significantly lower compared to 5w or 5w-shCTR pairs (*$p < 0.05$). **D** Coupling coefficients (two for each pair in the respective direction of current flow) in respect to the distance between the soma centers of the two neurons for 5w, 5w-shCx36 and 5w-shCTR. **E** Resting membrane potentials of IO neurons were similar in all groups. Colors: blue, week 3 (3w); orange, week 5 (5w); green, week 5 and knockdown of Cx36 (5w-shCx36); purple, week 5 and control vector (5w-shCTR).

3.3 Sub-threshold oscillations: occurrence and synchrony

Sub-threshold oscillations (STO) are thought to play a key role in synchronizing the supra-threshold activity among coupled IO neurons. In our study STO were mainly observed from postnatal week 3 (3w) on. Only 11 % (2/18) of recorded neurons from 2w rats were oscillating during the recording compared to 80 % (12/15) of neurons from 3w rats ($p = 0.0009$, Fisher's exact 2-sided). Between 3w and 5w (81 % (35 of 43)), no significant difference in the proportion of oscillating neurons was observed ($p = 1$). Interestingly, uncoupling of neurons did not lead to changes in STO probability. In 5w-shCx36 neurons 78 % (18 of 23) exhibited robust STO and 9 % (2) small amplitude STOs of low power and low temporal stability. This STO probability was not significantly different from wildtype 5w neurons ($p = 0.189$) (**Figure 12A**). Despite no changes in STO probability, uncoupling increased the dominant STO frequency in 5w-shCx36 neurons: whereas the medians of dominant frequencies were similar in neurons from WT rats independent of age (2w: 2.22 (1.43 - 3.00) Hz; 3w: 2.55 (1.72 - 3.12) Hz; 5w: 2.62 (1.82 - 3.98) Hz), uncoupled 5w-shCx36 neurons had a significantly higher dominant frequency of 3.72 (2.72 - 4.46) Hz compared to neurons from 5w animals ($p = 0.024$, KW for 3w, 5w, 5w-shCx36 & Dunn's post-hoc vs. 5w) indicating that uncoupling made them oscillate at their intrinsic or resonant frequency rather than at the common dominant frequency of the electrotonically coupled cluster (**Figure 12B**). We found that the relative power of STO dominant frequency was lower in the 2 neurons from 2w rats that oscillated at all (0.029 & 0.324 mV^2) compared to the other groups. The mean dominant STO frequency powers of neurons from 3w (0.401 ± 0.043 mV^2, $n = 12$) and 5w (0.390 ± 0.022 mV^2, $n = 35$) were not significantly different nor did uncoupling significantly reduce the power in 5w-shCx36 neurons (0.354 ± 0.035 mV^2, $n = 20$) compared to the age matched wildtype or 3w ($p = 0.578$, ANOVA) (**Figure 12C**).

Paired recordings from 5w WT and uncoupled 5w-shCx36 neurons were also used to investigate the synchrony of STO among neighboring neurons. We calculated the cross-correlation coefficient (CCC) of STO and derived the phase lag [°] of the two waveforms from the time between the maximum CCC and zero taking into account the local dominant frequency. We could not find significant differences between the groups in median CCC (5w: 0.945 (0.913 - 0.953), $n = 5$ vs. 5w-shCx36: 0.952 (0.811 - 0.978, $n = 11$, $p = 0.777$, MWU) or the mean phase lag (5w: 8.286 ± 3.991° vs. 5w-shCx36: 9.850 ± 3.200°, $p = 0.780$, t-test). However, we examined possible correlations with either the mean CC of the pair; the soma-somatic distance of the pair; or, for pairs with 5w-shCx36 neurons, the local transduction density.

Whereas phase lags in wildtype neuron pairs were small even in cases of low CCs ($r = 0.12$, $p = 0.854$, $n = 5$), we observed a trend to increased phase lags with smaller CCs in pairs with 5w-shCx36 neurons ($r = -0.49$, $p = 0.125$, $n = 11$). Only weak, non-significant correlations of the phase lag

with the soma-somatic distance of the pair were found for 5w WT or 5w-shCx36 pairs (r = 0.30, p = 0.627 & r = 0.27, p = 0.426 resp.).

In line with this observation, CCCs derived from oscillating 5w WT pairs were very robust even in cases of low CCs (r = 0.35, p = 0.565) pointing to a strong drive to maintain synchrony by the local cluster of neurons interconnected via gap junctions, in which both members of the recorded pairs may potentially have been embedded, despite low direct electrotonic coupling. In pairs with 5w-shCx36 neurons this population-drive for synchrony may have gotten disrupted by decreasing the coupling to neighboring neurons of the cluster, as we saw a significantly correlated decrease in CCCs with smaller coupling (r = 0.62, p = 0.040).

CCCs of 5w WT pairs also did not show any dependence on the soma-somatic distance of the pair (r = 0.02, p = 0.976) whereas CCCs of pairs with 5w-shCx36 neurons seemed more influenced by distance (r = -0.43, p = 0.190).

For pairs with 5w-shCx36 neurons, we were able to relate phase lags and CCCs to the normalized local transduction density (cells/4*10^5 µm³). We found trends to an increase in phase lag and to a decrease in CCC with higher local transduction density (r = 0.57, p = 0.141 & r = -0.54, p = 0.169 resp., n = 8) adding further support to our hypothesis that the local coupled cluster is the primary driving force for synchrony rather than the one-by-one gap junctional coupling of individual IO neurons to a particular neighbor (**Figure 12D**).

In general phase lag and CCC were independent of STO dominant frequency as we could not find any significant correlations of neither phase lag (5w: r = 0.06, p = 0.920; 5w-shCx36: r = -0.44, p = 0.176) nor CCC (5w: r = -0.04, p = 0.950; 5w-shCx36: r = 0.16, p = 0.635) with the STO dominant frequency.

We may conclude that synchrony of pairs within the extent of proposed clusters depends on the electrotonic coupling of the cluster members and that this coupling is dominated by gap junctions composed of Cx36. Thus, artificial RNAi-mediated uncoupling that is wide-spread enough to disrupt such a cluster abolishes synchrony among these neurons. Furthermore, maintenance of STO seems to be an intrinsic property of IO neurons, rather than a feature emerging from electrotonically coupled clusters, and this property seems to be robustly established after postnatal week 2. Intrinsic dominant frequency however seems to depend on coupling as uncoupled 5w-shCx36 neurons showed increased dominant STO frequencies.

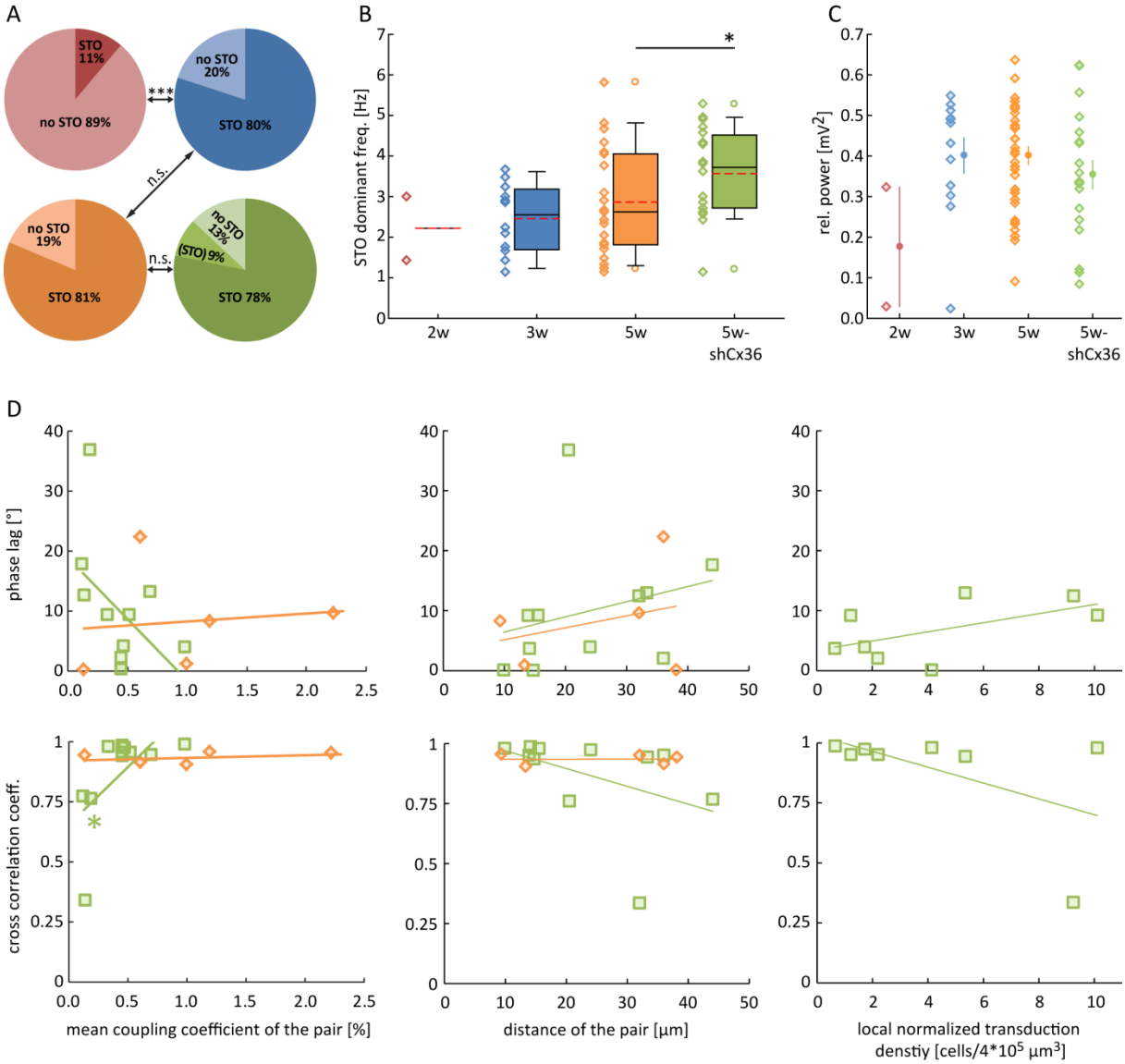

Figure 12. Sub-threshold oscillations (STO) in IO neurons.
A Probabilities of STO observation during whole-cell recording of neurons from 2w, 3w, 5w and 5w-shCx36 animals. Only a few 2w neurons exhibited STO in contrast to the majority of 3w, 5w, or 5w-shCx36 neurons. **B** Dominant frequencies of STO were similar in 2w, 3w and 5w neurons but significantly higher in 5w-shCx36 compared to 5w. **C** Relative power of STO were independent of age and coupling. **D** STO synchrony in pairs of IO neurons. Phase lag (upper row) and cross correlation coefficient (lower row) plotted against either the mean coupling coefficient, the soma-somatic distance of the pair, or the local normalized transduction density for 5w and 5w-shCx36. In 5w pairs phase lag and cross correlation were largely independent of coupling or distance whereas in 5w-shCx36 pairs higher phase lag and lower cross correlation were prominent at low coupling, greater distance or higher local transduction density. *p<0.05; ***p<0.001. Colors: blue, week 3 (3w); orange, week 5 (5w); green, week 5 and knockdown of Cx36 (5w-shCx36).

3.4 Phase-locking of regenerative events to sub-threshold oscillations

The probability for observing spontaneous action potentials in IO neurons has been described to be higher around the peak of the sub-threshold oscillation (STO) which is when the neuron is more depolarized (Llinas and Yarom 1986) and is likely independent of the phase of the synaptic input (Lampl and Yarom 1993). We examined the event vs. STO-phase relationship for sAP and sp in IO

neurons from 3w & 5w and from 5w-shCx36 neurons, as we did not observe any regenerative events during STO in the 2 oscillating neurons from 2w rats. Examples of sAP and sp occurrence during STO in two different neurons recorded in 5w animals are shown in Figure 13.

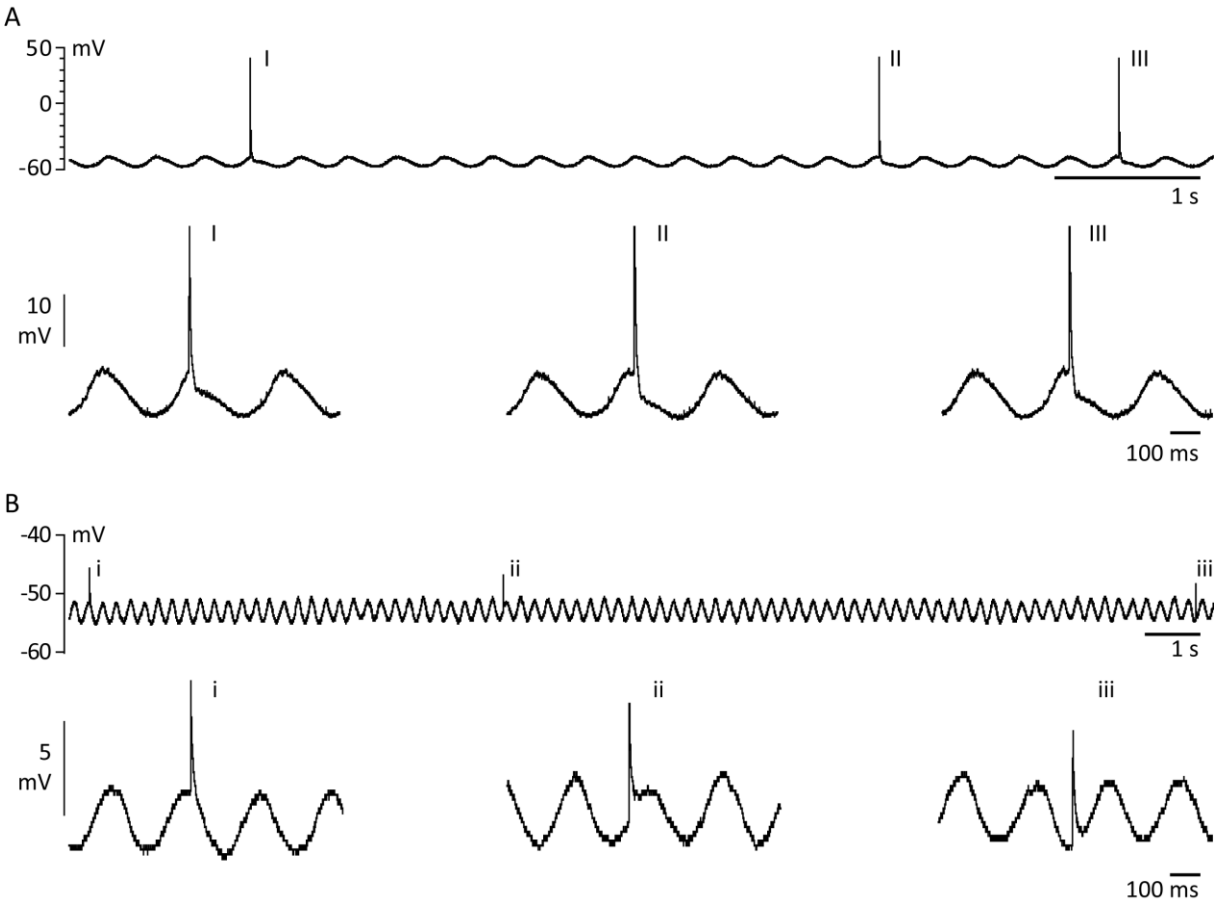

Figure 13. Occurrence of regenerative events during STO.
A Three sAP (I, II, III) during STO recorded in an olivary neuron from the 5w group. sAP have been truncated for clarity in the magnifications (lower row). sAP typically occurred around the peak of the STO-phase. B Three sp (i, ii, iii) during STO recorded in a different olivary neuron from the 5w group. sp could be observed over the full STO-phase but occurrence probability was higher after the STO peak.

Figure 14A shows the occurrence of regenerative events in respect to the STO-phase and the corresponding histograms of the event probabilities.

We employed circular statistics to describe the relation between STO-phase and event parameters (Berens 2009; Zar 1999) by utilizing the following measures: Alongside the *mean resultant vector* (the analogon to the mean in circular statistics) and its *circular standard deviation*, we used *skewness* and *symmetry around the median* to examine the symmetry (negative value: asymmetry to the right, positive value: asymmetry to the left), while *vector length* and *kurtosis k* provided a good intuitive measure of the peakedness of the distribution ($0 \leq k \leq 1$; where $k \to 1$: distr. with narrow peak (leptokurtic) and slim tails; $k \to 0$: distr. with broad peak and broad tails (platykurtic)). Moreover, *Rao's spacing test on uniformity* was employed to

assess whether the occurrence of events was phase-locked or randomly distributed over the STO-cycle and was chosen due to its robustness irrespective of the underlying distribution.

We found that for sAP the positions of the *mean resultant vectors* were right before the peak of the STO-cycle (defined as π) in all 3 groups and event distributions were quite symmetric ($p > 0.05$ in all cases, test for *symmetry around the median*). Nevertheless, a small positive *skewness* in the 3w group revealed a slight leftward asymmetry thus indicating that the neurons were more likely to fire on the rising phase of the STO than on the falling. Moreover, the *vector length* and *kurtosis* increased from 3w to 5w indicating an increased phase-locking to the STO peak by changing from a less peaked platykurtic to a more peaked leptokurtic distribution. This phase-locking was independent of coupling as the distribution of of sAP in uncoupled 5w-shCx36 neurons showed similar *vector length* and a leptokurtic distribution (**Figure 14B**). *Rao's Spacing test* found that sAP of the 3w group but not of the 5w & 5w-shCx36 groups were uniformly distributed over the STO cycle which indicates that at 3w randomness of firing dominated over event-STO phase-locking.

These observations raise the question whether spikelets, the presumed electrotonically transmitted echo of the firing of coupled neighboring neurons, would show a congruent event distribution over the STO cycle.

We found the *mean resultant vectors* of sp in all groups pointing to a position right after the peak of the STO-cycle, which is reasonable assuming some delay by the transmission through gap junctions and along the dendritic structures. Similar to our observations on sAP, a small leftward asymmetry (small positive *skewness*) was observed for sp of the 3w group while sp of the 5w group were quite symmetric. This observed asymmetry at 3w was significant with the test for *symmetry around the mean*. Interestingly, we could see a small leftward shift in *skewness* of sp in the 5w-shCx36 group despite that no such asymmetry could be seen in sAP. Although we found that the sp *vector lengths* were almost identical among the groups and only slightly increasing from 3w to 5w, we found that, in line with the picture of the sAP, the distribution of sp in the 3w group was platykurtic as well, whereas the distribution in the 5w group was also more leptokurtic. Interestingly, uncoupling of neurons seemed to have resulted in a lower sp phase-locking, as the distribution of sp in the 5w-shCx36 group was found to be platykurtic, resembling the lower phase-locking seen in the 3w group (**Figure 14B**). We tested for uniformity as before: *Rao's Spacing test* found sp of the 3w group to be uniformly distributed. This changed with maturation as at 5w sp were not uniformly distributed. Interestingly, uncoupling seemed to have had an impact on the phase-locking as we observed a uniform distribution of sp in 5w-shCx36 despite the non-uniform sAP distribution.

Taken together we found a lower degree of STO phase-locking of sAP and sp in neurons from 3w rats. In neurons from 5w rats, a high degree of phase-locking was found for sAP and sp. Uncoupling

destroyed this close relationship: while phase-locking of sAP, likely a property of the single neuron and not a phenomenon associated with gap junctional coupling, was unaltered in these neurons, sp were phase-locked to a lower degree which may largely be due to the reduced or eliminated STO synchrony after uncoupling.

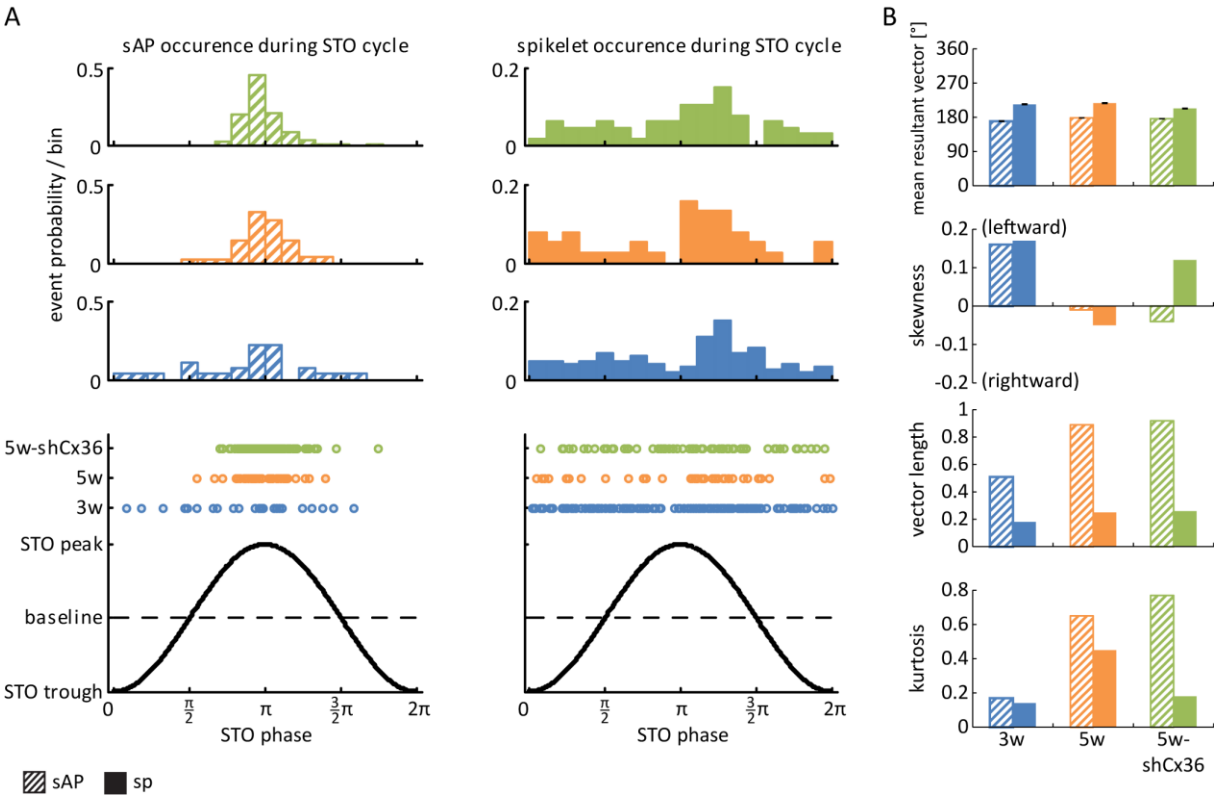

Figure 14. Regenerative events in relation to the phase of the STO cycle.
A Events detected in 3w (blue), 5w (orange) and 5w-shCx36 (green) relative to their occurrence in the "underlying" STO cycle and the respective probability histograms (top). sAP were uniformly distributed in 3w but were STO peak aligned in 5w and 5w-shCx36; sp were uniformly distributed in 3w but STO peak aligned in 5w, uncoupling (5w-shCx36) resulted in a uniform sp distribution. **B** Circular measurements of the event distributions over the STO cycle. In all groups, the mean resultant vectors (circular means) of sAP and sp were located before and after the STO peak, respectively. In the 3w group, small positive (leftward) skewness, short vector length and platykurtosis of sAP and sp indicate a more uniform distribution of events over the STO cycle. In the 5w group in contrast, a skewness close to zero, longer vector length (in sAP) and leptokurtosis reflect a narrow distribution around the STO peak. Uncoupling (5w-shCx36) did not change the distribution of sAP but sp were more likely to occur on the rising phase of the STO cycle (leftward skewness) and showed a more uniform distribution (platykurtic).

3.5 Parameters of regenerative events are sensitive to the STO state

It remains unclear whether certain parameters of sAP and sp would convey information about the actual phase or amplitude of the STO at the time of the event - an information about the oscillatory state that then potentially could be transmitted to electrically coupled neighboring neurons and/or, via CF and their collaterals, to the target neurons (PC and neurons of the CN). Yet, aside from the experimental description and quantification of the wavelets riding atop the characteristically long

ADP (Bazzigaluppi et al. 2012; Mathy et al. 2009) and a recent attempt to identify the mechanisms that may link wavelet properties to STO phase by modeling (De Gruijl et al. 2012), we are not aware of any study addressing this aspect in detail.

We therefore examined the same parameters as described above for sAP and sp the in context of the phase or amplitude of the STO by fitting either a combination model of sine and cosine or a linear regression model and calculating the circular-linear or the linear correlation, respectively (**Figure 16 & Figure 17**).

We observed clear differences in the sensitivity of parameters to STO phase or amplitude arising during postnatal development between 3w and 5w and also found alterations after uncoupling by RNAi (5w-shCx36).

3.5.1 sAP vs. STO phase

The size of the *sAP amplitude* was significantly correlated with the STO phase in a positive manner (amplitudes were highest around the peak of the STO cycle) at 3w ($r = 0.54$, $p = 0.008$, $n = 27$) whereas this relationship was inverted at 5w ($r = 0.41$, $p = 0.009$, $n = 56$) with lower amplitudes around the STO peak. Uncoupling however resulted in a loss of this correlation ($r = 0.16$, $p = 0.085$, $n = 187$).

Regarding parameters associated with the depolarizing component of sAP, the *rise time* was not significantly correlated with the STO phase (3w: $r = 0.29$, $p = 0.324$; 5w: $r = 0.33$, $p = 0.051$), yet its fast component, the *10 - 90 % rise time*, was significantly smaller around the STO peak in 3w ($r = 0.71$, $p = 0.001$) and 5w ($r = 0.43$, $p = 0.006$) alike. This was also reflected in the significantly higher *10 - 90 % slope* in 3w ($r = 0.76$, $p < 0.001$) around the STO peak. Interestingly, the 5w group did not show a significant correlation here ($r = 0.08$, $p = 0.822$). Uncoupling resulted in a low but highly significant correlation of the *rise time* with the STO phase ($r = 0.33$, $p < 0.001$), yet in a reduced correlation of the *10 - 90 % rise time* ($r = 0.23$, $p = 0.007$) while the *10 - 90 % slope* was also not significantly correlated with the STO phase ($r = 0.18$, $p = 0.055$).

The *decay times* were significantly shorter around the STO peak in 3w ($r = 0.69$, $p = 0.002$) with high correlation and in 5w ($r = 0.41$, $p = 0.01$) with lower correlation. After uncoupling this correlation was even lower albeit being highly significant ($r = 0.3$, $p < 0.001$). The *half-width* was not significantly correlated with the STO phase in either of the WT groups (3w: $r = 0.22$, $p = 0.525$; 5w: $r = 0.29$, $p = 0.101$). The vividly discussed *number of wavelets* was not significantly correlated in 3w ($r = 0.47$, $p = 0.053$) in contrast to a significant correlation in 5w ($r = 0.43$, $p = 0.005$, $n = 57$) with less wavelets (only the initial sodium spike and no wavelets at all in most cases) around the peak of the STO cycle and more wavelets if sAP occurred not around the peak. Moreover, we found a quite substantial difference in the distribution of the *numbers of wavelets* between the 3w and 5w groups. Whereas in

3w most sAP had one or more wavelets, most sAP in 5w did not exhibit wavelets, but if they did, either one or around 4 wavelets were observed (**Figure 15**).

Uncoupling led to a significant correlation of the *half-width* ($r = 0.19$, $p = 0.04$) being smaller at the peak of the STO, an even stronger correlation of the *number of wavelets* ($r = 0.5$, $p < 0.001$) with the STO phase, as well as a lack of higher numbers of wavelets per sAP (**Figure 15**). The *area*, however, was not correlated in 3w ($r = 0.37$, $p = 0.158$) but in 5w ($r = 0.46$, $p = 0.003$) with areas being smaller around the STO peak, which is in line with the lower amplitudes observed. Uncoupling did not alter this correlation ($r = 0.4$, $p < 0.001$) (**Figure 16, left**).

Taken together, in IO neurons recorded from slices of 3w old animals sAP de- and repolarized faster and their amplitudes were higher if occurring around the peak of the STO cycle. This was also true for neurons from 5w animals with the exception that correlations were weaker and, most prominently, that the amplitudes were lower when occurring around the peak. Uncoupling of neurons from their local cluster eliminated the significant correlation for the *sAP amplitude*, reduced correlation of the *10 - 90 % rise time* but on the other hand established significant correlations for *rise time* (lower around the STO peak) and *half-width* (smaller around the peak).

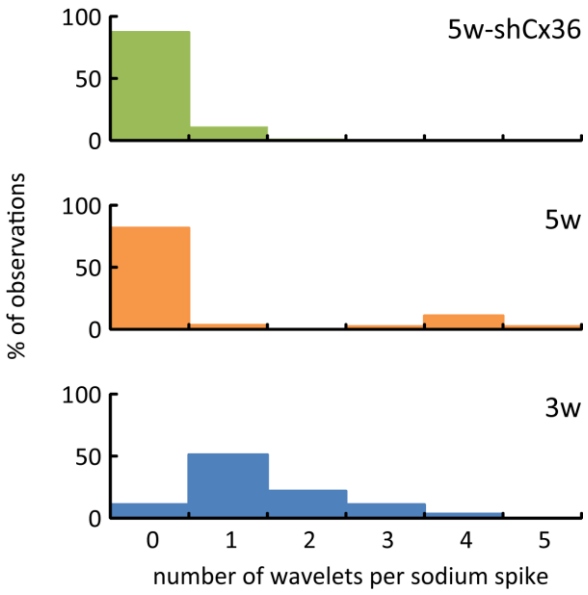

Figure 15. Distribution of numbers of wavelets during STO.
In the 3w group most sAP showed a sodium spike followed by one wavelet. In contrast, in the 5w and 5w-shCx36 groups the majority of sAP did not exhibit wavelets and those that did, showed either one or around 4 wavelets. In 5w-shCx36 neurons no sAP with high numbers of wavelets were observed.

3.5.2 sAP vs. STO amplitude

We found that the *sAP amplitude* had a significant positive correlation with the STO amplitude in 3w ($r = 0.55$, $p = 0.003$) but not in 5w ($r = -0.09$, $p = 0.494$). Uncoupling resulted in a weak but significant negative correlation ($r = -0.2$, $p = 0.006$).

Results

Like in the case of the association with the STO phase , no significant correlation was found for the *rise time* in the WT groups (3w: r = -0.22, p = 0.271; 5w: r = 0.13, p = 0.35) but was seen for the *10 - 90 % rise time* (3w: r = -0.59, p = 0.001; 5w: r = -0.36, p = 0.007) and consequently for the *10 - 90 % slope* (3w: r = 0.67, p < 0.001; 5w: r = 0.35, p = 0.008). After uncoupling, a significant correlation of the *rise time* (r = 0.26, p < 0.001) with the STO amplitude was observed but correlations of the *10 - 90 % rise time* (r = -0.03, p = 0.68) or of the *10 - 90 % slope* (r = 0.03, p = 0.706) vanished.

Moreover, we found a highly significant negative correlation of the *decay time* with the STO amplitude for 3w (r = -0.78, p < 0.001) but not for 5w (r = -0.17, p = 0.226), which was unchanged after uncoupling (5w-shCx36: r = -0.05, p =0.489).

Whereas the *half-width* was significantly negatively correlated in 3w (r = -0.49, p = 0.01) but not in 5w (r = -0.24, p = 0.073), we did not find significant correlations of the *number of wavelets* with the STO amplitude in the WT groups (3w: r = 0.24, p = 0.238; 5w: r = 0.11, p = 0.413). Surprisingly, uncoupling resulted in a small but significant positive correlation of the *half-width* (r = 0.19, p = 0.011) and also in a significant negative correlation of the *number of wavelets* (r = -0.24, p < 0.001) with the STO amplitude.

We did not observe significant correlations of the *area* with the STO amplitude in the WT groups (3w: r = 0.17, p = 0.387; 5w: r = 0.04, p = 0.792) but did so after uncoupling (5w-shCx36: r = -0.15, p = 0.043).

Taken together, sAP de- and repolarized faster in IO neurons recorded from slices of 3w animals and their amplitudes were higher if they occurred at higher STO amplitude. While 5w neurons still depolarized faster at higher STO amplitude, they did not seem to be sensitive to STO amplitude in respect to the sAP repolarization or in respect to the *sAP amplitude*. Uncoupling of neurons from their local cluster eliminated correlations of the fast components of the depolarization but on the other hand established significant positive correlations for *rise time* (lower around the STO peak) and *half-width* (smaller around the peak) as well as negative correlations for the *sAP amplitude*, *area* and for the *number of wavelets* (**Figure 16, right**).

Results

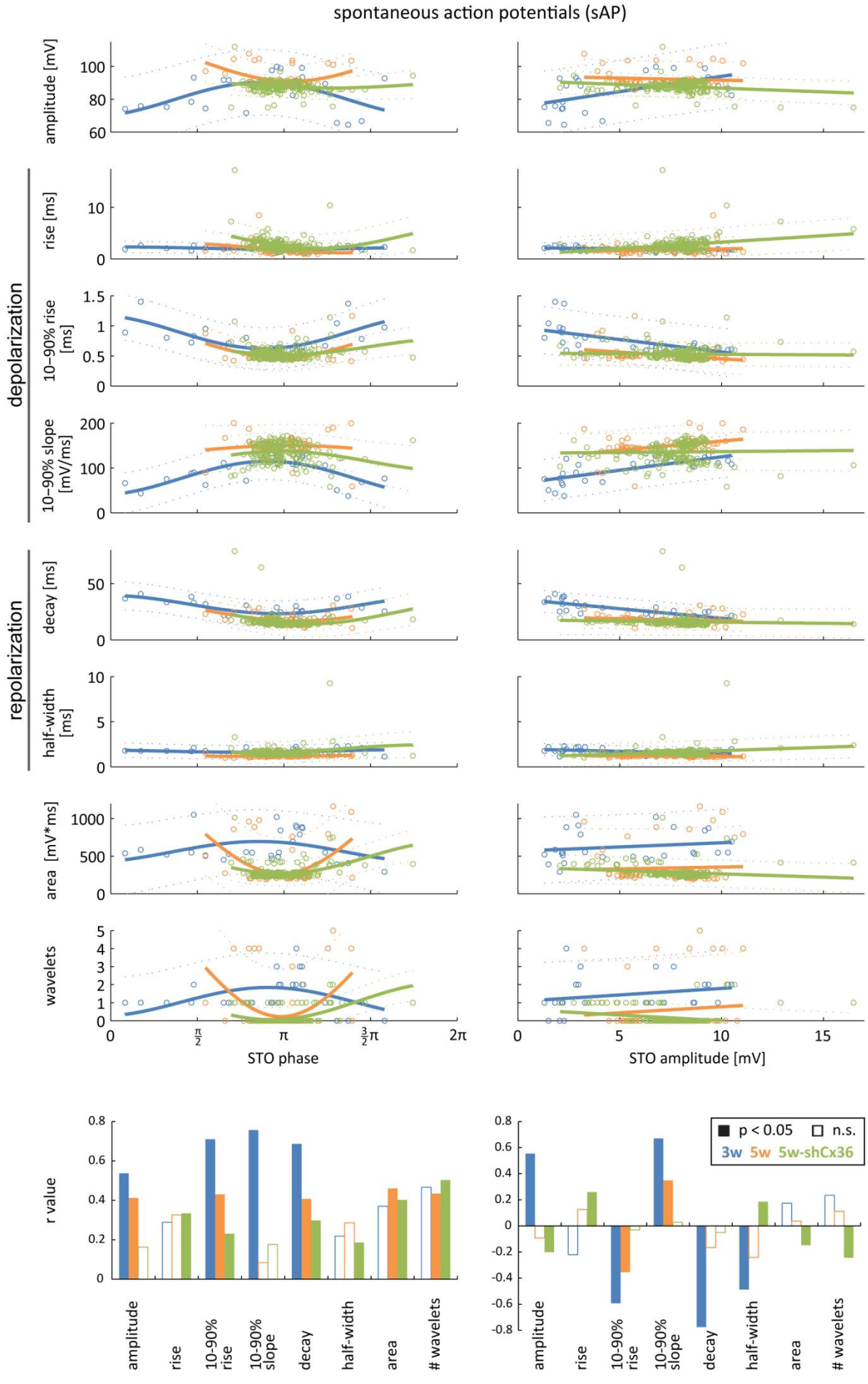
spontaneous action potentials (sAP)
depolarization
repolarization
amplitude [mV]
rise [ms]
10–90% rise [ms]
10–90% slope [mV/ms]
decay [ms]
half-width [ms]
area [mV*ms]
wavelets
STO phase
STO amplitude [mV]
r value
p < 0.05
n.s.
3w 5w 5w-shCx36
amplitude
rise
10-90% rise
10-90% slope
decay
half-width
area
wavelets

Figure 16. Parameters of sAP in respect to STO phase and amplitude.
Parameters of sAP kinetics were plotted against the STO phase (left) or amplitude (right) and fitted by a combined sine and cosine function or by a linear function, respectively. R-values of the fits are plotted in the lower bar charts. Filled bars indicate significance ($p < 0.05$). In 3w neurons, sAP de- and repolarized faster and had higher *amplitudes* when they occurred around the peak of the STO cycle or when the STO amplitude was higher. In 5w neurons, sAP were also faster when they occurred around the peak of the STO cycle but then their amplitudes were lower; only depolarization was faster at higher STO amplitudes. Uncoupling (5w-shCx36) led to smaller correlations in general and to the establishment of new significant correlations without affecting the notion that kinetics were faster around the STO peak. Yet, no correlation of the sAP *amplitude* with the STO phase was present any more. Moreover, a stronger sensitivity of sAP *amplitude*, *rise time*, *half-width* and *area* to the STO amplitude were observed. In 3w neurons, no significant correlations between the *number of wavelets* and the STO state could be found. In contrast, less wavelets could be observed around the peak of the STO cycle in 5w and 5w-shCx36 neurons and the *number of wavelets* was negatively correlated with the STO amplitude in 5w-shCx36 neurons. Colors: blue, week 3 (3w); orange, week 5 (5w); green, week 5 and knockdown of Cx36 (5w-shCx36).

3.5.3 sp vs. STO phase

We asked whether we might find similar sensitivities of the spikelet parameters to STO phase or amplitude (**Figure 17**). Analyzed in an identical manner, we found that sp *amplitudes* were correlated to the STO phase only at younger age with higher *amplitudes* at the upward STO half-cycle (3w: $r = 0.26$, $p = 0.008$, $n = 145$; 5w: $r = 0.34$, $p = 0.114$, $n = 38$) and uncoupling did not have any impact (5w-shCx36: $r = 0.25$, $p = 0.123$, $n = 67$).

From the parameters of the depolarization only the *rise time* was significantly correlated in both WT groups (3w: $r = 0.41$; 5w: $r = 0.61$; both: $p < 0.001$) with longer *rise times* if sp occurred on the upward STO half-cycle. Uncoupling did not affect this correlation (5w-shCx36: $r = 0.488$, $p < 0.001$). Neither the *10 - 90 % rise time* (3w: $r = 0.06$, $p = 0.797$; 5w: $r = 0.23$, $p = 0.362$) nor the *10 - 90 % slope* (3w: $r = 0.1$, $p = 0.475$; 5w: $r = 0.32$, $p = 0.152$) exhibited any significant correlation with the STO phase, and uncoupling had no impact on these parameters either ($r = 0.28$, $p = 0.075$ & $r = 0.17$, $p = 0.364$, resp.).

The sp *decay time* was significantly correlated with the STO phase, being longer at the upward STO half-cycle, in both WT groups (3w: $r = 0.43$, 5w: $r = 0.65$; both $p < 0.001$) as well as after uncoupling (5w-shCx36: $r = 0.43$, $p = 0.002$). Likewise, the *half-width* was larger during the upward STO half-cycle with significant correlations in both age groups (3w: $r = 0.38$, $p < 0.001$; 5w: $r = 0.47$, $p=0.014$). Uncoupling eliminated this correlation ($r = 0.24$, $p = 0.151$). The *area* was significantly correlated in all WT groups (3w: $r=0.56$, $p<0.001$; 5w: $r = 0.52$, $p = 0.006$) and after uncoupling ($r = 0.55$, $p < 0.001$), being larger at the upward STO phase (**Figure 17, left**).

In general, and in contrast to sAP, differences in sp parameters appeared not to be associated with the peak of the STO phase but rather with whether a sp occurred on the up- or downward half-cycle of the STO and fast components did not play a role possibly due to the low-pass filter properties of the gap junctions through which they putatively are transmitted. We found *sp amplitudes* to be sensitive to the upward STO half-cycle only in 3w but not in 5w or after uncoupling, sensitivity of

rise time and *decay time* as well as *area* was independent of age or coupling. Only the sensitivity of the *half-width* to the STO phase was eliminated by uncoupling.

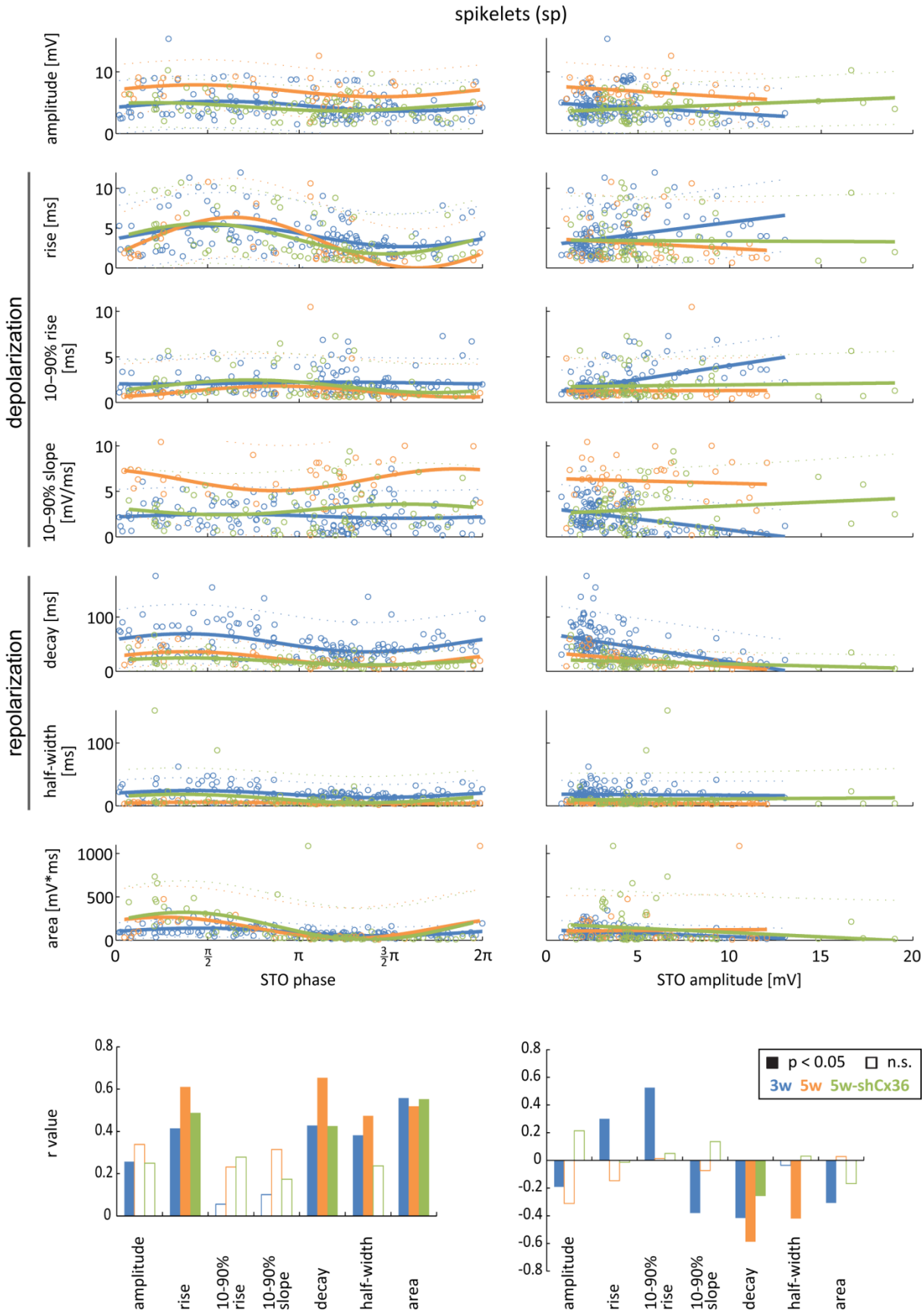

Figure 17. Parameters of sp in respect to STO phase and amplitude.
Data was processed and plotted as in Figure 16. In 3w neurons, sp had higher *amplitudes*, were slower (longer *rise time*) and lasted longer (longer *decay time* and *half-width*) when they occurred on the upward half of the STO cycle. Moreover, sp showed lower *amplitudes*, slower depolarization but shorter *decay time* when they occurred at higher STO amplitude. In 5w neurons, similar to 3w, sp were also slower and lasted longer when they occurred on the upward half of the STO cycle. sp repolarized faster (shorter *decay time* and *half-width*) when they occurred at higher STO amplitude. Uncoupling (5w-shCx36) did not disrupt the correlation of longer *rise time* or longer *decay time* with the STO cycle (each slightly smaller but significant), but no correlation could be found for the *half-width* any more. Only *decay times* were found to be shorter when occurring at higher STO amplitude. The *area* was larger in neurons from all groups when sp occurred on the upward half but only significantly negatively correlated with higher STO amplitude in 3w. Colors: blue, week 3 (3w); orange, week 5 (5w); green, week 5 and knockdown of Cx36 (5w-shCx36).

3.5.4 sp vs. STO amplitude

The sp *amplitude* showed a weak yet significant negative correlation with the STO amplitude in 3w ($r = -0.19$, $p = 0.022$) but not in 5w ($r = -0.31$, $p = 0.058$) or after uncoupling (5w-shCx36: $r = 0.21$, $p = 0.082$).

Parameters of the depolarization were found to be significantly correlated only in the 3w group (positive for *rise time* and *10 - 90 % rise time*; negative for the *10 - 90 % slope*) and uncoupling did not have an impact on any of the parameters: *rise time* (3w: $r = 0.3$, $p < 0.001$; 5w: $r = -0.15$, $p = 0.379$; 5w-shCx36: $r = -0.01$, $p = 0.912$), *10 - 90 % rise time* (3w: $r = 0.53$, $p < 0.001$; 5w: $r = 0.01$, $p = 0.935$; 5w-shCx36: $r = 0.05$, $p = 0.686$) and *10 - 90 % slope* (3w: $r = -0.38$, $p < 0.001$; 5w: $r = -0.07$, $p = 0.662$; 5w-shCx36: $r = 0.14$, $p = 0.273$).

The *decay time* had a significant negative correlation with the STO amplitude in 3w ($r = -0.42$, $p < 0.001$) and 5w ($r = -0.59$, $p < 0.001$). Uncoupling reduced this correlation (5w-shCx36: $r = -0.26$, $p = 0.035$). In contrast to 3w ($r = -0.04$, $p = 0.673$), the *half-width* in 5w ($r = -0.42$, $p = 0.009$) had a significant negative correlation with the STO amplitude and uncoupling eliminated this correlation ($r = 0.03$, $p = 0.803$). The *area* was significantly negatively correlated only in 3w ($r = -0.31$, $p < 0.001$) but not in 5w (5w: $r = 0.03$, $p = 0.69$) or after uncoupling (5w-shCx36: $r = 0.17$, $p = 0.176$) (**Figure 17, right**).

Aside from the *half-width*, all sp parameters were sensitive to the STO amplitude in the 3w group but only *decay time* and the *half-width* were sensitive in the 5w group. Uncoupling had modest impact on these relationships whilst eliminating the sensitivity of the *half-width*.

In summary, we found that at younger age (3w), when electrical coupling is high among IO neurons, sAP were bigger and faster if they occurred around the STO peak or if the STO amplitude was high. Later (5w), when neurons seem to be only moderately coupled, this association was weaker or even reversed (sAP amplitude vs. STO phase). Correlations of wavelets with the STO phase were found only in 5w, where more wavelets were present when the sAP were not occurring at the STO peak. When neurons were uncoupled from their neighbors, the speed of the sAP was largely independent

of the STO phase or amplitude at the time of the event. Interestingly, in 5w-shCx36 neurons the half-width was smaller at the STO peak but higher at higher STO amplitude. Moreover, the *area* and the *number of wavelets* became more sensitive to STO amplitude indicating that the changes described above that go along with the uncoupling (higher excitability, faster STO frequency) may impact the sensitivity of these parameters to STO phase and amplitude.

We could describe a rather complex pattern of developmental changes in sAP parameter sensitivity and could show that the manipulation of the degree of gap junctional coupling had an impact on this sensitivity. Yet, so far we do not know which mechanism in the end may bridge the gap between parameter sensitivity to STO features and the degree of coupling, but assuming that coupled neurons behave like a syncytium, event probability and kinetics may synchronize as well across the coupled cluster. On the other hand, common input with high temporal precision could also likely serve as an explanation but further experiments and different approaches are surely necessary to address this question.

3.6 Connexin 36 immunohistology

To histologically verify the efficacy of RNAi, confocal laser scanning microscopy image stacks of IO regions were obtained from brain slices of LV-shCx36 rats three weeks after olivary injection of the lentiviral vector constructs (either vector constructs shCx36i (n = 10) or shCx36ii (n = 12)). Slices were immunostained for Cx36 (Meier et al. 2002) and the widely used dendritic marker MAP2. On the basis of MAP2 staining, transduced structures exhibiting the co-expressed EGFP (*MAP2 & EGFP*) were separated from non-transduced structures (*MAP2 only*) by thresholding and co-localization, resulting in two volume masks. **Figure 18A** depicts a typical example of one transduced LV-shCx36ii-EGFP neuron and its surrounding volume stained for MAP2 and Cx36. The Cx36 signal was co-localized with either the *MAP2 & EGFP* or the *MAP2 only* volume mask and Cx36 spots were detected in an automatized approach (**Figure 18B**) revealing a substantial reduction in Cx36 spot density from 2.41 spots/1000 µm^3 in *MAP2 & EGFP* structures compared to 1.21 spots/1000 µm^3 in *MAP2 only* structures. It may not surprise that Cx36 immunopuncta were still found after RNAi knockdown due to some residual Cx36 expression and their focal accumulation in gap junctions. More interestingly may therefore be to examine the intensity and diameter of these detected spots as scaffold structures of GJ may still persist even in the case of Cx36 knockdown. The example showed an increase of the spot diameter from 0.87 ± 0.01 µm in *MAP2 only* spots to 0.94 ± 0.03 µm in *MAP2 & EGFP* spots. This increase went along with a significantly reduced mean spot intensity of 1092 ± 67 a.u. (n = 20) in *MAP2 & EGFP* spots compared to 1417 ± 34 a.u. (n = 110) in *MAP2 only* spots ($p < 0.001$, t-test) (**Figure 18C**).

Alike, analysis of the population dataset revealed reductions of the relative number of Cx36 spots per volume in IO tissue transduced with LV-shCx36i (*MAP2 & EGFP*: 1.45 ± 0.33 spots/1000 µm^3 vs. *MAP2 only*: 1.73 ± 0.40 spots/1000 µm^3, n = 10, p = 0.316) or LV-shCx36ii (*MAP2 & EGFP*: 1.27 ± 0.33 spots/1000 µm^3 vs. *MAP2 only*: 2.9 ± 0.66 spots/1000 µm^3, n = 12, p = 0.03). Transduction with the LV-shCx36i or LV-shCx36ii construct similarly resulted in significantly increased spot diameters of about +14 % (1.24 ± 0.11 µm vs. 1.09 ± 0.08 µm, p = 0.001) or +19 % (1.08 ± 0.1 µm vs. 0.91 ± 0.06 µm, p = 0.004), respectively compared to non-transduced structures. Moreover, the mean spot intensity was significantly reduced by about -26 % (1092 ± 55 a.u. vs. 1482 ± 66 a.u., p < 0.0001) for LV-shCx36i and by about -27 % (649 ± 85 a.u. vs. 889 ± 76 a.u., p = 0.001) for LV-shCx36ii (paired t-tests each). (Figure 18D)

We saw that transduction with the LV-shCx36 constructs not only led to reductions of Cx36-spots in the respective (dendritic) structures but also led to decrease of the intensity of these immunospots indicating that there are not only fewer gap junctions but that they may also contain less Cx36 channels.

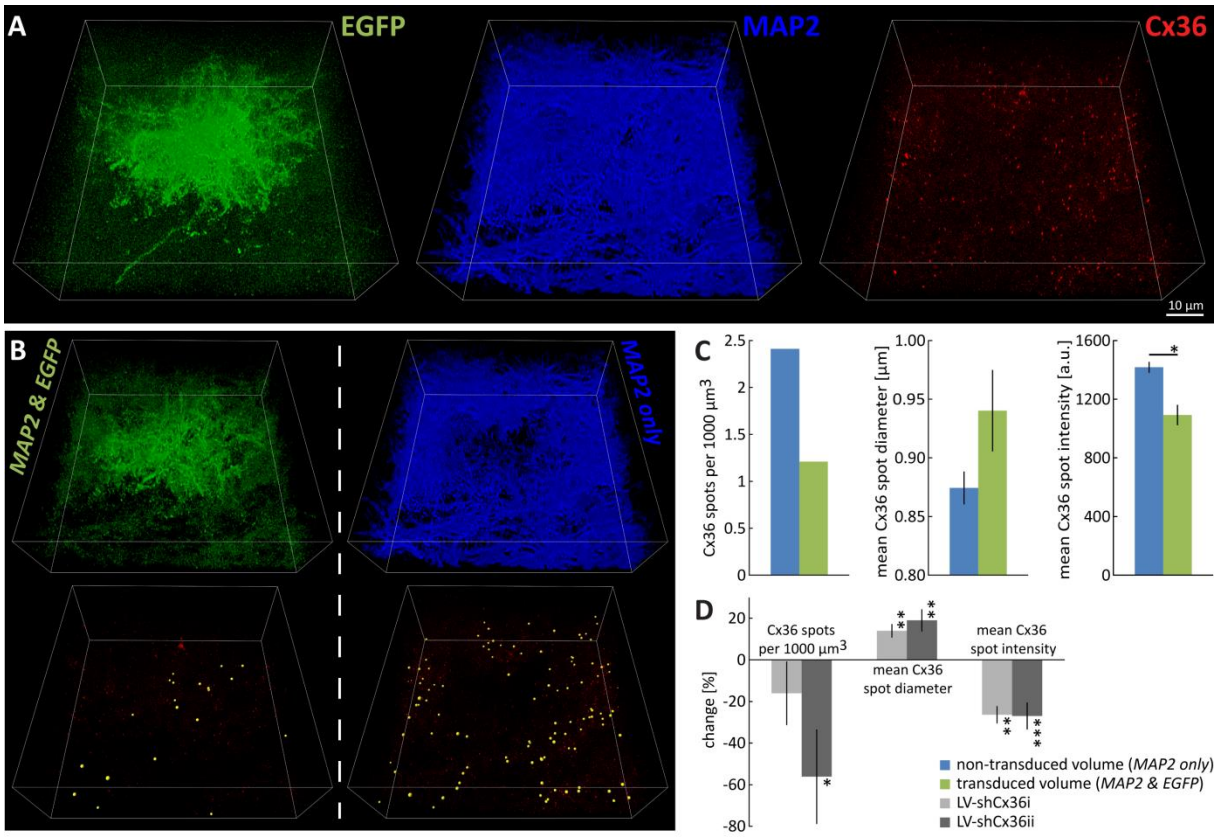

Figure 18. Immunohistology of Cx36 in LV-shCx36 transduced IO neurons to assess *in vivo* efficacy of RNAi. A, B, C Typical example of one LV-shCX36 transduced IO neuron. A Intrinsic EGFP fluorescence of a transduced neuron was imaged alongside immunostaining for the dendritic marker MAP2 and for Cx36. B Two sub-volumes were calculated based on co-localization of *MAP2 & EGFP* (green) or its inverse with *MAP2 only* (and no EFGP) (blue). These 3D masks were used to split the Cx36 signal into two sub-volumes (transduced, lower left and non-transduced, lower right) on which identical spot detections were performed. C In this example effective RNAi of Cx36 is evident by reduced spot density (Cx36 spots per 1000 µm3), and lower mean spot intensity. Interestingly the mean spot diameter was slightly larger. D Population data. Both lentiviral constructs

used yielded effective RNAi performance with reduced number of Cx36 spots, increased diameter and lower mean spot intensity. *p < 0.05; **p < 0.01; ***p < 0.001.

3.7 Spatial and temporal analysis of free locomotion

Rats were subjected to spatio-temporal locomotion analysis to investigate whether the knockdown of Cx36 and the resulting uncoupling would influence the coordination during free locomotion. We compared wildtype animals (n = 16) with animals that received a unilateral injection of either the functional LV-shCx36 (n = 11) or the non-functional LV-shCTR (n = 8) lentiviral vector solution in the right IO under electrophysiological guidance.

Locomotion was recorded 11 days (p32) after injection following initial days of habituation and training (**Figure 19A**). The parameters utilized to determine possible alterations in gait were *stand*, *swing* & *cycle times*, *swing speed*, *stride length*, *mean print area*, *couplings* (*diagonal*, *girdle* & *ipsilateral*), *base of support*, *step regularity index*, *cadence*, *support pattern* and *step sequence* (**Figure 19C**).

Moreover, we attempted attribute observed locomotor changes to distinct IO sub-nuclei by subsequent histological characterization of the extent of the transduction and identification of affected IO sub-nuclei. Hereby, we could classify LV-shCx36 animals into 3 sub-groups based on the major transduction in either only the dorsal olive (*DAO only*, n = 2), the dorsal and principal olive (*DAO+PO*, n = 7) or where the medial olive was also transduced (*MAO*, n = 2) (**Figure 19B**).

Surprisingly, at first glance, no obvious impairment of motor function became apparent in either of the LV groups, when the animals were actively exploring their home cage. They were able to keep balance and even climbed along the bar-lid of the cage. No direct signs of ataxia could be observed. Consequently, we could not detect significant changes in virtually any of parameters analyzed when the treatment groups (LV-shCx36 or LV-shCTR) were compared to the wildtype (without differentiating for the sub-nuclei transduced), with the exception of *step regularity* and *support pattern*. LV-shCTR groups were not significantly different from the wildtype in any of the parameters assessed. We could detect subtle, yet significant changes in *step regularity*, decreasing from 99.85 ± 0.15 % in WT (and 100 ± 0 % in LV-shCTR) to 99.01 ± 0.42 % in LV-shCx36 rats (p = 0.034, KW). In detail, when differentiating for the transduction of the IO sub-nuclei, it was seen that the LV-shCx36(*DAO only*) animals exhibited the lowest step regularity (98.48 ± 1.52 %). Moreover, we observed alterations of the *support pattern* in the LV-shCx36 group. The percentual *diagonal support* was significantly higher in the LV-shCx36 group compared to the WT group (72.7 ± 3.4 % vs. 64.6 ± 1.6 %, p = 0.034, ANOVA & Dunnett's post-hoc test), indicating that these animals needed additional stability along their cross-axis. Furthermore, when looking at the performance of the individual animals, the front paw *base of support* in LV-shCx36 rats, albeit not significantly different

from the WT in the group means, became significantly smaller with increased degree of transduction ($r = -0.72$, $p = 0.013$), which suggests that the more widespread the transduction was, the more did the animals keep their feet together avoiding far reaching movements in the lateral domain. The hind paw *base of support* was not different among groups.

Taken the sub-groups into consideration, we found that the mean stand times of LV-shCx36(*MAO*) rats were significantly longer compared to the wildtype (210 ± 4 ms vs. 181 ± 4 ms, $p = 0.003$, resp., KW & Dunn's). This prolonged stand time also had an impact on the duration of the cycle time (LV-shCx36(*MAO*): 346 ± 4 ms vs. WT: 315 ± 4 ms, $p = 0.021$, KW & Dunn's) whereas swing times were not significantly affected but were slightly longer in the LV-shCx36(*MAO*) group (145 ± 2 ms vs. WT: 136 ± 2 ms, $p > 0.05$, ANOVA). In line with this observation the *swing speed* was slower, albeit not significantly, in the LV-shCx36(*MAO*) group (77 ± 0.9 cm/s vs. WT: 87.1 ± 1.7 cm/s, $p > 0.05$, KW). In this group, the *cadence* was also slightly but not significantly reduced as well compared to the wildtype (LV-shCx36(*MAO*): 11.6 ± 0.3 steps/s vs. 13.7 ± 0.4 steps/s, resp., $p > 0.05$, ANOVA). It seems that if medial parts of the IO were transduced, longer *stand times* and a general trend to slow down movement speed may reflect the need to compensate for possible difficulties in coordination. This finding is in accordance with observations on the consequences of pharmacological lesions of the IO in the cat (Horn et al. 2012). The mean *stride length* in the LV-shCx36(*DAO+PO*) group was significantly longer than in the WT group (120.8 ± 1.1 mm vs. 115.1 ± 1.1 mm, $p = 0.003$, resp., KW & Dunn's) (**Figure 19C**).

Moreover, we calculated the locomotion parameters for front and hind paws separately and did not detect significant differences among the groups (**Figure 20**).

Furthermore, we investigated the laterality of locomotion parameters by calculating their ratios of the left and right paws for all paws as well as for the front and hind paws. For the front paws, we found a leftward bias for longer *stride length* in the LV-shCx36(*DAO only*) group compared to the wildtype (3.8 ± 2.8 % vs. -0.5 ± 0.5 %, resp., $p = 0.019$, ANOVA & Dunnett's). In line with this finding, a leftward bias could be seen for the mean *print area* (all paws) in the LV-shCx36(*DAO only*) group (24.3 ± 9.9 % vs. WT: -2.7 ± 2.8 %, $p = 0.004$, ANOVA & Dunnett's) mainly caused by the bias for the front paws (34.5 ± 19.3 % vs. WT: -3.2 ± 4.7 %, $p = 0.03$, ANOVA & Dunnett's). Interestingly, the observed significant directional bias was leftward - contralateral to the injection site in the right IO (**Figure 20**). However, *couplings* which reflect the inter-paw coordination and which were expected to be most susceptible to manipulations of olivary electrical coupling were not affected at all. Likewise did the *step sequence*, another reliable measure of coordination, not exhibit any major changes (**Figure 19C**).

We conclude that unilateral uncoupling of IO neurons did not have a distinct impact on inter-paw coordination. Nevertheless, given that *stand times* were longer in LV-shCx36(*MAO*) animals and that

we could observe a general slowdown of the *step cycle*, we speculate that these changes may reflect some adaptation to overcome possible difficulties arising from the uncoupling of IO neurons and that this adaptation may stabilize the paw coordination providing the animals more time to precisely control movement and limb interplay.

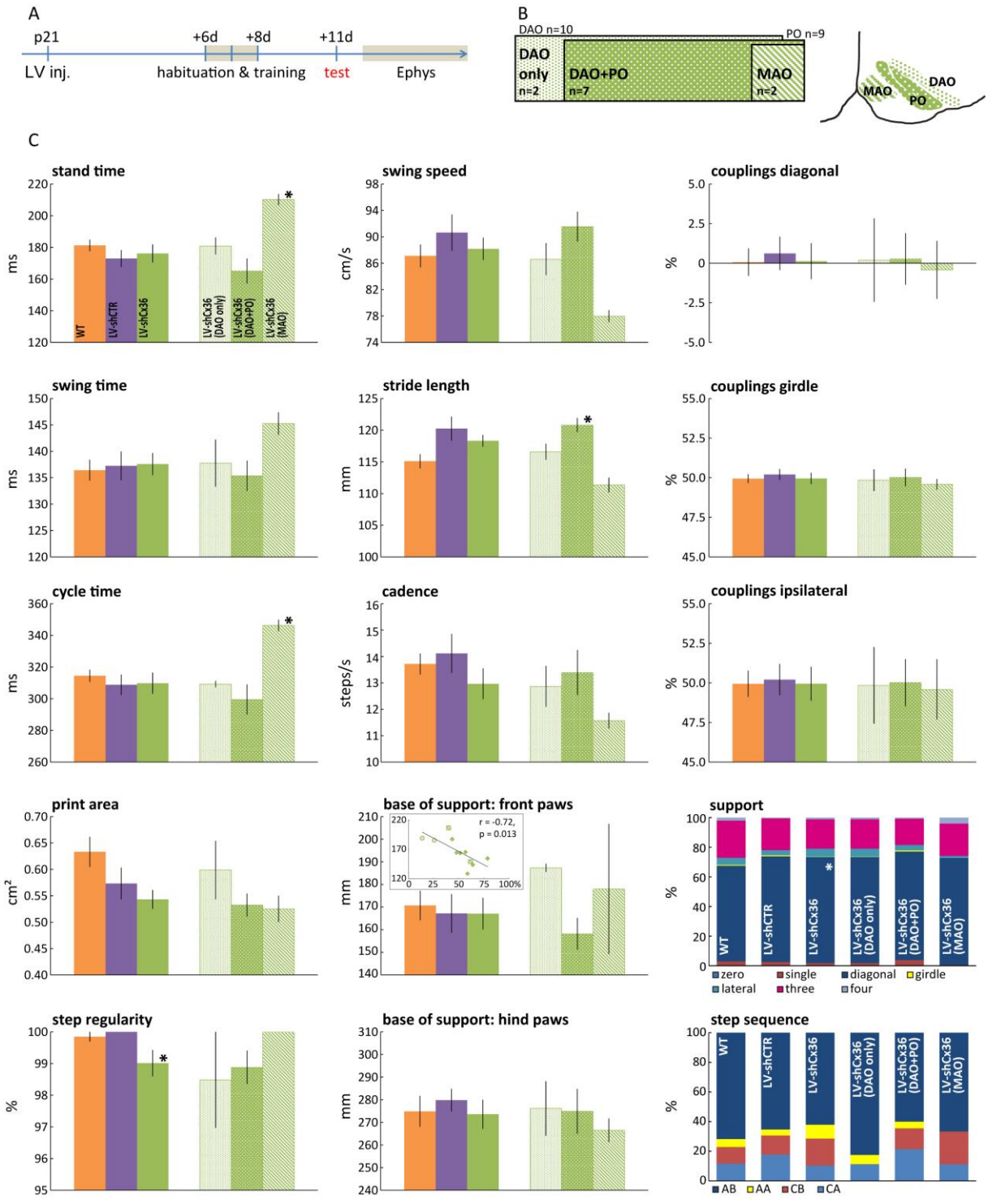

Figure 19. Analysis of free locomotion revealed small changes in motor performance.
A Timeline of intervention and examination. Rats received a lentiviral injection (LV-shCx36 or LV-shCTR) into the right IO at p21 and were subjected to three consecutive habituation and training sessions 6, 7 and 8 days after the injection. Test examination took place 11 days after the injection (p32). **B** Graphical depiction of the

number of animals that were grouped based on which IO sub-nuclei were transduced. Three groups were distinguished: LV-shCx36(*DAO only*), where detectable transduction could only be seen in the dorsal olive (n = 2); LV-shCx36(*DAO+PO*), where dorsal and principle olive were transduced (n = 7); and LV-shCx36(*MAO*), where the medial olive was also transduced (n = 2). **C** Parameters derived from spatio-temporal locomotion analysis: *stand*, *swing* and *cycle time*, *print area*, *step regularity*, *swing speed*, *stride length*, *cadence*, *base of support* of front paws (inset: base of support vs. overall degree of IO transduction) and hind paws, *diagonal*, *girdle* and *ipsilateral couplings*, *support pattern* and *step sequence* for WT (orange), LV-shCTR (purple), LV-shCx36 (green) and the respective LV-shCX36 sub-groups as described in B. *p<0.05 vs. WT.

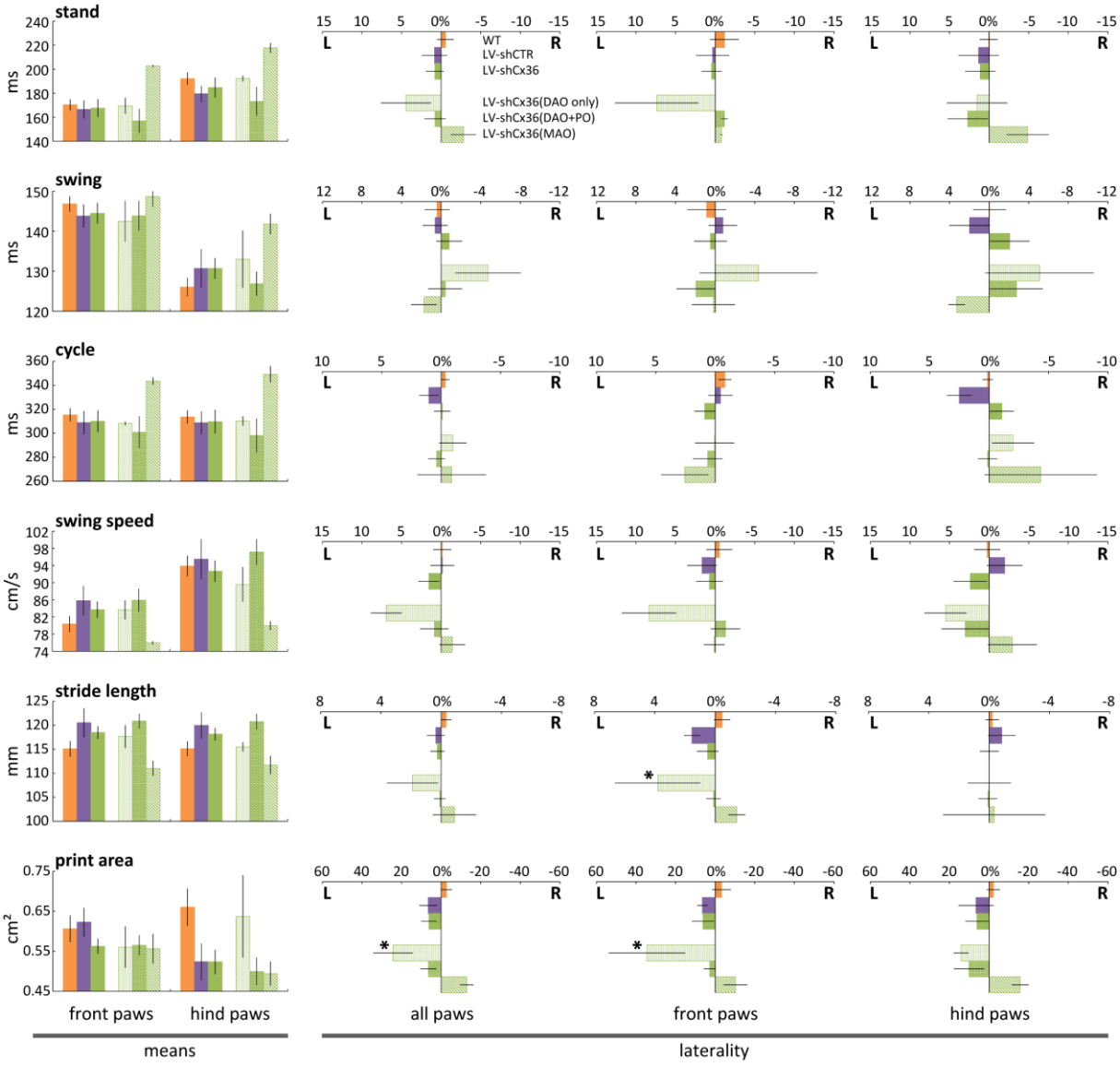

Figure 20. Free locomotion parameters separated for front and hind paws and their laterality.
Locomotion parameter means of *stand*, *swing* and *cycle time*, *swing speed*, *stride length* and *print area* separated for front and hind paws and the laterality calculated as ratio of the respective means for all paws (see **Figure 19C**) or separated for front and hind paws. WT (orange), LV-shCTR (purple), LV-shCx36 (green) and the respective LV-shCX36 sub-groups. *p<0.05 vs. WT.

4. Discussion

We investigated the developmental dynamics of gap junctional coupling in the IO of juvenile rats covering a period between postnatal weeks 2 and 5 and attempted a local knockdown of connexin 36, the major gap junction forming protein in the IO. We could show: (i) that the probability of occurrence and the frequencies of spontaneous regenerative events (actions potentials and spikelets) are positively associated with the degree of gap junctional (dye-) coupling but that the kinetics of these parameters follow a more complex pattern of alteration; (ii) that gap junctional coupling is highest around postnatal week 3 and decreases thereafter; (iii) that robust STOs are present from postnatal week 3 on and that they are intrinsically maintained even after knockdown of Cx36 (at increased dominant frequency); (iv) that STO synchrony among IO neurons is preserved even in low coupled wildtype pairs but not so after Cx36 knockdown; (v) that the STO phase-locking of regenerative events and their parameters is subject to change during maturation and that knockdown of Cx36 has an impact on the alignment of sp to the STO peak; and finally (vi) that unilateral knockdown of Cx36 in the IO has some but only minor consequences on free locomotion and that the observed effects may depend on transduction of particular sub-nuclei with the lentiviral vector.

4.1 Regenerative events are associated with gap junctional coupling

To our best knowledge we are the first to report that the spontaneous activity of IO neurons recorded from acute slices is markedly altered over the course of the first postnatal weeks and that the kinetics of these regenerative events undergo changes during that period.

Neurons from 2 weeks old animals, where dye-coupling was virtually absent, had a low probability of exhibiting either sAP or sp and the respective event frequencies were also low. In the course of maturation sAP and sp probabilities and event frequencies increased, as seen in neurons from 3 weeks old animals which showed a higher degree of dye-coupling. Thereafter, in slices from 5 weeks old animals where dye-coupling was found to be lower, sAP and sp probabilities and frequencies decreased again to levels similar to those in the 2 weeks old animals. The close linear relationship between mean sAP and sp frequencies across the groups indicates that both sAP and sp reflect the general state of spontaneous activity of IO neurons and that they are closely interrelated in the normally developing IO. We also observed a change in the kinetics of regenerative events during maturation. sAP and sp amplitudes increased and de- and repolarizations became faster in a corresponding manner as the animals got older. Astonishingly knockdown of Cx36 in 5w-shCx36 neurons led to even faster kinetics.

Moreover, the general excitability of neurons, reflected in the slope of the VI-curves, steadily decreased over the course of maturation but interestingly did this neither correspond to the increased activity nor to the higher dye-coupling seen in the 3 weeks old animals. Here we may have

observed the effect of general mechanisms linked to the maturation of neurons in terms of dendritic geometry (Metzger 2010; Puram and Bonni 2013), altered expression of P/Q-type and T-type calcium channels which respectively generate high- or low-voltage activated currents (Cho et al. 2011; Rossi et al. 1994; Vincent et al. 2000), or alterations of channel kinetics (Cho et al. 2011) i.e. by exchange of ion channel subunits (Chen et al. 2006).

Immunohistology in the rat IO had shown that expression of NMDA receptor subunits NR1 (GluN1) and NR2A/B (GluN2A/B) increased, and that AMPA/KA subunits GluR4 decreased and GluR5/6/7 increased from p7 to adulthood - with changes pronounced between p14 and p21 (Chen et al. 2006). It is well conceivable that these alterations of receptors have effects on spontaneous activity, alter event kinetics and affect the maintenance of STO (Placantonakis and Welsh 2001; Turecek et al. 2014; Zhu et al. 2014).

To our surprise, 5w-shCx36 neurons had a membrane excitability (steeper VI-curve) resembling the VI-relationship of 3w neurons which may explain the observed similar mean sAP frequencies. The steeper VI-curve may be the direct consequence of uncoupling of the neurons from their electrical syncytium formed with the ”normally” gap junction coupled neuron cluster. This would increase the input resistance and hence also the general excitability. In contrast, despite an increased input resistance, no increase in IO sAP frequency was described in $Cx36^{-/-}$ mice (De Zeeuw et al. 2003; Long et al. 2002) (yet, no reports on sp occurrence are available) but neurons from these animals responded abnormally to hyperpolarizing current injections with a prominent sag that resulted in triggering a low-threshold calcium spike eventually giving rise to a sodium action potential. Yet, the reported increase in membrane area and the observed thicker proximal dendrites may have substantially changed the physiological properties of these neurons (De Zeeuw et al. 2003) adapting them to deal with the lack of coupling. Block of Cx36 function by dominant-negative inhibition also did not produce abnormal spiking nor did it affect the firing rhythmicity (Placantonakis et al. 2004). In contrast, one study carried out in $Cx36^{-/-}$ mice *in vivo* (Marshall et al. 2007) reported lower complex spike firing rates in PC (indirectly reflecting IO activity) and attributed them to the loss of electrical coupling.

On the other hand, the faster kinetics observed in 5w-shCX36 neurons could be explained by a lower membrane capacitance that would be expected if the capacitance mediated by functional gap junctions is eliminated or highly reduced. Membrane capacitance was previously described to be about 50 % lower in $Cx36^{-/-}$ mice (Bazzigaluppi et al. 2012). A lower capacitance would lead to faster charging of the membrane and thus would speed up membrane potential changes resulting in faster parameters of de- and repolarization.

It seems that neurons react to uncoupling by altering their excitability. It is reasonable to assume that this is not simply due to isolation from the coupled cluster - as we find a similar VI-relationship in

3w neurons that are intensely coupled (based on NB dye-coupling) - but that it may more likely be an active adaptation to the "lack" of coupling. Considering recent findings describing active feedback mechanisms that act on the gap junctions to regulate the degree of coupling on different timescales (O'Brien 2014) we speculate that the chronic uncoupling by RNAi used here could have resulted in a severe disturbance of these mechanisms and subsequently have led to the activation of pathways that may regulate the density and/or the excitability of membrane ion channels resulting in the observed change in responsiveness to sub-threshold current injections.

4.2 Dye-coupling, electrotonic coupling and the presence of gap junctions

There are quite contradicting studies on the question of the presence and extent of functional gap junctions in young rats. Ultra-structural electron microscopy on one hand could not provide evidence for gap junctions in rats younger than p7 and in the course of maturation immature "kissing" junctions are formed around p10 but mature gap junctions are seen not earlier than from p15 on (Bourrat and Sotelo 1983). On the other hand, functional calcium imaging as well as paired recordings in the IO of animals between p0.5 and p15.5 indicate the presence of gap junctions even at very young age. Synchronous clusters of activity were observed with increasing probability until p12.5 followed by a sudden drop (Rekling et al. 2012). *In situ* hybridization also indicates the presence and constant increase of Cx36 mRNA from p1 to p21 (Van Der Giessen et al. 2006) but when exactly functional gap junctions, capable of transmitting dye and/or electrical signals, are formed remains controversial. Our data from postnatal week 2 (p13 to p16) animals identified a period during development where we could not detect dye-coupling, indicating the lack of functional gap junctions - and only sparse presence of STO. This picture changed dramatically at 3 weeks (p20 to p23) when not only more than 60 % of neurons showed dye-coupling but also the majority of them maintained stable STO.

It has been widely accepted that dye-coupling in the IO depends on the presence of functional open gap junctions (Leznik and Llinas 2005) composed of Cx36 (De Zeeuw et al. 2003; Placantonakis et al. 2006). Yet, while clear differences in dye-coupling could be seen between those groups with low (2w, 5w, 5w-shCx36) and high coupling (3w), it was impossible for us to quantify any differences in dye-coupling between the 5w and 5w-shCx36 groups despite the difference in electrotonic coupling found in recorded neuron pairs from 5w-shCx36 rats compared to the higher electrotonic coupling in 5w. While this study could not address the detailed relationship of dye- and electrotonic coupling, one has to appreciate that both phenomena are not interchangeable in a one-to-one fashion.

Since most studies which examined neurobiotin dye-coupling in the rat IO used animals younger than 3 weeks (Devor and Yarom 2002a; Hoge et al. 2011), one cannot rule out that pronounced dye-

coupling is a feature mainly found in neurons of the immature IO within that particular time frame and that there might be differences in the way small molecules diffuse through gap junctions in more mature neurons. Yet, a study in older rats (4-10 weeks) found dye-coupling similar to the situation in younger animals (Placantonakis et al. 2006). However, in that study acute slices where cut in the parasagittal plane, in contrast to slicing in the coronal plane performed here, and the degree of coupling among neurons in a cluster may have an axial polarity.

Our RNAi approach effectively reduced the electrotonic coupling between IO neurons indicating that gap junctions composed of Cx36 could be eliminated to a large degree and, as indicated previously (Long et al. 2002), that other connexins i.e. Cx57 (Zappala et al. 2010) or Cx43 (Van Der Giessen et al. 2006), both expressed in the mouse IO, play a negligible role in the (electrical) coupling among IO neurons and likely serve other purposes.

4.3 Nature of spikelets

Spikelets were first observed in the hippocampus (Spencer and Kandel 1961) and later also in the IO (Llinas et al. 1974; Llinas and Yarom 1981a) but not investigated in detail. More recently, Chorev et al. (2007) found spikelets in the rat IO *in vivo* and it seems that they are already present in acute slices of very young mice (Kølvraa et al. 2013; Rekling et al. 2012) but a detailed description is yet missing. A body of evidence generated from examination of hippocampal and cortical pyramidal cells (MacVicar and Dudek 1981; Mercer et al. 2006), Golgi cells of the dorsal cochlear nucleus (Yaeger and Trussell 2016) and the cerebellum (van Welie et al. 2016), and IO neurons (Llinas et al. 1974) suggests that spikelets originate from gap junctional transmission of APs in connected neighboring neurons. Moreover, in combined dual intra- and extracellular recordings performed *in vivo* in hippocampal CA1 pyramidal neurons, spikelets could be associated with preceding extracellular potentials having their source in firing neurons nearby, likely coupled via gap junctions (Chorev and Brecht 2012) and neurons in the Mesencephalic Trigeminal Nucleus show spikelets elicited by the transmission of action potentials via soma-somatic gap junctions (Curti et al. 2012).

We found spikelets in all age groups and their occurrence and frequencies were closely associated with the degree of dye-coupling in wildtype neurons which strongly indicates that gap junctional coupling may be the underlying mechanism. Careful analysis of the event parameters revealed a speed up of spikelet kinetics similar to that seen for sAP which further supports the hypothesis that electrical coupling is the underlying mechanism that links sAP and spikelets. We could further observe that in neurons from 3 weeks old rats sAP on average exhibited a longer ADP which seemed to be echoed by a larger area of the spikelets speaking for electrical coupling as the source of spikelets. Yet, general changes of excitability may affect sAP and spikelets in a comparable manner even if spikelets are solely elicited without the contribution of gap junctions.

Yet, to our great surprise we also observed spikelets in 5w-shCx36 neurons which challenges the idea that gap junctional coupling is the underlying mechanism of spikelet generation.

Even more so, spikelets were not attenuated in 5w-shCx36 neurons compared to 5w as one would expect from the low-pass filter properties of gap junctions (Galarreta and Hestrin 1999) and the lack or massive reduction of gap junctions should result in higher dampening of fast components. During paired recordings we could see such dampening of DJPs in coupled neurons when rebound AP were elicited in connected neighboring neurons. Interestingly, the kinetics of these DJPs differed substantially from the waveforms of spikelets. Instead, we found that the spikelet amplitudes were higher and their depolarization even faster whereas the parameters of the repolarization phase did not change at all. An active component involved in the generation, propagation, or shaping of spikelets, as described in voltage-dependent "boosting" of junctional potentials (Curti and Pereda 2004; Dugue et al. 2009; Mann-Metzer and Yarom 1999), may explain our observations. In cerebellar Golgi cells such amplifications depend on sodium channels (Dugue et al. 2009), but the presence and nature of a similar mechanism in the IO would need further detailed investigation.

On the other hand, the stronger excitability of 5w-shCx36 neurons might partly explain the stability or speeding-up of the kinetics. These changes have their main effect on membrane resistance change in the dendritic compartment but less so in the soma. Thus, sAP in the soma may be less affected than spikelets travelling along the dendritic tree.

Two alternative explanations on the origin of spikelets will be further considered here: First, axo-axonal coupling via gap junctions in the vicinity of the axon initial segment could lead to transfer of AP from connected neighboring neurons and subsequent antidromic invasion of charges into the soma would appear as spikelets (Schmitz et al. 2001). Yet, only shown in hippocampal pyramidal cells, it remains open whether a similar mechanism might exist in IO neurons and if, which connexins (different from Cx36) would contribute. Second, the observed spikelets could be regenerative potentials originating in the dendrite and being triggered by synaptic input and/or junctional potentials and maintained by the boosting mechanism described above (Chorev et al. 2007). However, Rash et al. (2007) found persisting spikelets in the suprachiasmatic nucleus (where electrotonic coupling is abundant) during whole-cell recordings with the sodium channel blocker QX-314 in the pipette solution and these spikelets could only be eliminated when AP generation was blocked by bath application of the sodium channel blocker tetrodotoxin (TTX), speaking for triggering of spikelets by coupled neighboring neurons.

We may infer from our observations and from the mentioned previous reports that spikelets likely have an active component located in the dendrite and that transfer of potentials via distal GJ may need amplification in the dendrite (especially given the long and often retroverting dendritic branches in IO neurons) to transmit to and invade the soma.

Even after RNAi mediated uncoupling, few remaining GJ-channels may still be able to locally trigger such a dendritic spikelet which would then propagate to the soma and therefore result in a waveform that may not be altered much. While uncoupling via RNAi may not fully diminish but strongly reduce I_{GJ}, these proposed amplification units may be able to compensate by changing their gain or their sensitivity to smaller input (through the remaining weak GJ). Such amplification mechanisms may not be activated at rebound induced deflections or APs which might explain why we could not observe similar kinetics / waveforms in our paired recording experiments.

While pharmacological inhibition of gap junctions would potentially be suited to answer the question whether spikelets are transmitted across gap junctions the uncertainty about their off-target effects on various receptors and conductances largely disqualifies gap junction blockers like i.e. carbenoxolone, which also acts on AMPA, NMDA and $GABA_A$ receptors with consequences on action potential properties and firing rate (Tovar et al. 2009), from use in this respect.

4.4 STO properties and synchrony

Sub-threshold oscillations were nearly absent in neurons from 2 weeks old animals and robust STO were established thereafter, as from 3 weeks on most neurons showed STO in congruence with previous reports (Bleasel and Pettigrew 1992; Pettigrew et al. 1988) and increased expression of NMDAR (Chen et al. 2006), shown to induce oscillations in the IO (Placantonakis and Welsh 2001; Zhu et al. 2014), may contribute.

In contrast to other studies that suspected electrical synapses to be essential for STO generation (Bleasel and Pettigrew 1992; Devor and Yarom 2002b; Llinas and Yarom 1986; Placantonakis et al. 2006) but in accordance with others who did not (Leznik and Llinas 2005; Long et al. 2002) STO were not eliminated by our RNAi based uncoupling approach. Rather we found that the dominant STO frequency in these neurons increased while the power remained unchanged. Comparable shifts towards higher STO frequencies within the same neuron were previously observed in the presence of the gap junction blocker 18β-glycyrrhetinic acid (Leznik and Llinas 2005). In contrast, picrotoxin application ($GABA_AR$ antagonist) led to reduced inhibition, increase in cluster size and lower STO frequencies (Leznik et al. 2002). Our results with the RNAi approach indicate that these shifts were likely not off-target effects of the uncoupling agents used in the other studies, but solely attributable to changes in coupling strength and extent. Uncoupled neurons may oscillate at their intrinsic dominant frequency and this frequency seems to be higher compared to the common dominant frequency of a coupled cluster of neurons, a concept also supported by recent modelling approaches (Torben-Nielsen et al. 2012).

Our recordings of pairs of neurons indicate that the synchrony of STO depends not only on the degree of coupling between the assessed pair but also on the local extent of coupling, thus on the

size of functional clusters which may act as units with a common STO frequency (Devor and Yarom 2002b) forming the basis for synchronized common response patterns. Reduced complex spike synchrony of PC *in vivo* was thus found after olivary injection of the gap junction blocker carbenoxolone (Blenkinsop and Lang 2006) or in $Cx36^{-/-}$ mice (Marshall et al. 2007).

Whereas STO cross-correlation in wildtype neuron pairs was surprisingly high even in cases where the pair was only weakly coupled, the cross-correlation collapsed in 5w-shCx36 neuron pairs with low coupling coefficient. Moreover, synchrony seemed to partially depend on the local density of neurons transduced with the viral vector construct and thus on the local degree of (un-) coupling surrounding the cells that have been recorded; or in other words, on the capability of the neurons to participate in local cluster formation.

4.5 Relationship between properties of events and STO

On the basis of our comprehensive examination of event occurrence, event kinetics as well as STO properties at different time points during postnatal development or after RNAi mediated uncoupling, we investigated whether event occurrence and kinetics were associated with the STO phase at the time of occurrence.

We could see that in 3w neurons the distribution of occurrence of sAP was uniform and not associated with the phase of the STO cycle, in contrast to the situation in 5w and 5w-shCx36 neurons where sAP occurred predominantly around the STO peak. Such phase-locking was described before (Bazzigaluppi et al. 2012; Khosrovani et al. 2007; Lampl and Yarom 1993; Llinas and Yarom 1986; Mathy et al. 2009) and was found to be disturbed in $Cx36^{-/-}$ mice (Bazzigaluppi et al. 2012). Moreover, a recent study suggests that phase-locking of olivary activity finds its reflection in quasiperiodic CS activity in awake mice (Negrello et al. 2019) which might form the substrate for reverberation of motor error information (Junker et al. 2018). Based on our observations, it seems that electrotonic coupling did not play a major role in the phase-locking of sAP but the increased alignment to the STO peak during early development may rather reflect a feature of general maturation of membrane conductances. Interestingly, we found a different picture for the phase-locking of spikelet occurrence. In 3w neurons, at a time point during postnatal development when gap junctional coupling was highest, the uniform distribution of spikelets resembled the distribution found for sAP. In 5w neurons, at overall moderate coupling, a non-uniform, peak aligned distribution of spikelet occurrence (with a reasonable delay right after the STO peak) may have its source in the transmission of highly STO-phase-aligned sAP from coupled neighboring neurons. When uncoupled by RNAi (5w-shCx36) the electrotonic transmission route was cut off and those spikelets that were still present were uniformly distributed despite the preserved STO-phase alignment of sAP in these neurons. Coding of the STO state by sAP may be a robust and coupling independent feature in more

matured IO neurons that seems to be largely unaltered by RNAi mediated knockdown of Cx36 while the occurrence of sp may depend on coupling and thus be impaired if gap junctions are reduced.

It should further be considered that the uniform distributions of sAP and spikelets in respect to the STO phase in the 3w neurons were observed within a period of postnatal development where refinement and maturation of the CF-PC connection take place (Hashimoto et al. 2009; Sugihara 2006)

We further assessed whether certain event kinetic parameters would be sensitive to the STO state. This would support the idea that information about the oscillatory state of the IO neuron and likely the common oscillatory state of the coupled cluster could potentially be transmitted via the CF signal to PC where it would elicit complex spikes with distinct features that recently have been associated with learning (Rasmussen et al. 2013). We found a rather complex picture but could identify some general relationships:

Irrespective of age or coupling state sAP were faster in all groups when occurring around the peak of the STO cycle. Moreover, kinetics were faster at higher STO amplitude in 3w neurons but this sensitivity was lost in 5w and 5w-shCx36 neurons. On the other hand, sp were in general slower and lasted longer when occurring during the upward part of the STO phase and were only considerably sensitive to the STO amplitude in 3w neuron.

The number of wavelets following the initial sodium component of the sAP was less around the STO peak in 5w and 5w-shCx36 in contrast to both other studies also examining this relationship where either no correlation was found (Bazzigaluppi et al. 2012) or more wavelets at the STO peak were observed (though under artificial STO generation by sinusoidal current injection) (Mathy et al. 2009). Modeling of IO networks of electrically coupled three-compartment neurons proposed that, (i) the number of wavelets would be higher if sAP occur on the rising phase of the STO cycle when an electrically coupled network was stimulated, but that this relationship would be attenuated if only a single cell was stimulated, (ii) that the bandwidth of possible wavelet numbers would be lower at single cell stimulation, and (iii) that there would be an inverse correlation of the number of wavelets with the STO amplitude (De Gruijl et al. 2012). While, as described above, the correlation of wavelets with the STO phase was found differently in our experiments, we could confirm the two other model predictions: First, we observed about 4 - 5 wavelets as the maximum in the 5w group but not more than 2 wavelets in the 5w-shCx36 group. We may therefore have provided experimental evidence that the possible number of wavelets that can be produced in a particular neuron depends on the coupling state of its local neuron cluster, as the transmission of common activity elicited by simultaneous input to a coupled cluster of neurons across functional gap junctions may participate in wavelet formation. Second, we could observe an inverse correlation of the number of wavelets with the STO amplitude. However, this inverse correlation was only found in the 5w-shCx36 group, but

not in the 3w or 5w groups, indicating that this feature may be a property of uncoupled neurons. However, the model predicted this relationship across different sizes of electrically coupled networks.

One may wonder whether the kinetics of sAP or spikelets may have any potential impact on the CF signal. If a sAP lasts longer it might elicit a CF burst that has more components, lasts longer and/or has a higher frequency. As such, it could transmit information about the oscillatory state to PC as already outlined with the sole focus on potential coding by wavelets (Mathy et al. 2009). CS waveform and duration correlate with CS firing frequency in the non-human primate (Warnaar et al. 2015) and recent reports showed that cerebellar plasticity and motor learning depend on the duration of the complex spike (Yang and Lisberger 2014) and on the number of spikes in the CF signal (Rasmussen et al. 2013). Whereas multiple CF burst-pulses facilitated cerebellar learning, single pulses led to an extinction of the learned response (Rasmussen et al. 2013). Most recently, convincing data on the positive correlation of CS synchrony and the number of CS wavelets was reported (Lang et al. 2014).

Similar, spikelets that last longer on the upward part of the STO cycle could promote threshold crossing by coinciding depolarizing input and thus increase firing probability.

Nevertheless, this study does and cannot address the question on the purpose of such coding and its functional relevance on the level of the target structures of the CF – the cerebellar cortex and cerebellar nuclei, the latter via collaterals. Studies manipulating the kinetics of sAP or spikelets, ideally *in vivo*, could shed light on this exciting aspect of olivo-cerebellar signal processing.

4.6 Gait

Early studies have suggested that the IO is involved in the timing of movements (Soechting et al. 1976) possibly by providing a coordinated output to muscle groups via the cerebellar cortex (Welsh et al. 1995). Furthermore, during treadmill locomotion firing rates of IO neurons match the step cycle frequency (Smith 1998) and groups of PC are co-activated by synchronous CF input (Ozden et al. 2012). This co-activation is reduced in the ataxic and dystonic *tottering* mouse mutant emphasizing the relevance of orchestrated CF input for motor performance (Hoogland et al. 2015).

$Cx36^{-/-}$ mice provided an opportunity to test the involvement of Cx36 based coupling in locomotion. But in line with the compensation seen on the cellular level (Kistler et al. 2002), motor performance was found not to be impaired as these mice had a wildtype-like free locomotion walking pattern and rotarod dwell time (Frisch et al. 2005; Kistler et al. 2002; Van Der Giessen et al. 2008). We also tested our LV-shCx36 animals for possible gait impairment. Across all animals tested (without differentiating for the IO sub-nuclei affected), we could observe a slight reduction of step

regularity and a significantly higher percental diagonal support. Moreover, the base of support for the front paws was negatively correlated with the degree of local transduction. Given the histological data of each individual subject animal, we could distinguish three groups (*DAO only*, *DAO+PO*, *MAO*) based on the transduced sub-nuclei. We could draw a rather complex picture of specific impairments: longer stand and cycle times were detected when the MAO was also transduced, while stride length was affected only in the LV-shCx36(*DAO+PO*) group. In the LV-shCx36(*DAO only*) group bias of the left front paw for longer stride length and correspondingly for increased mean print area were observed contralateral to the manipulated right IO.

The changes seen in the LV-shCx36(*MAO*) group are not surprising as it has been shown in the cat that most MAO neurons have wide-spread receptive fields spanning several limbs and body parts and are primarily activated when limb muscles and deeper structures are stimulated (Gellman et al. 1983). Uncoupling of neurons in this sub-nucleus may therefore more likely cause perturbations in gait when feedback from muscles and joints may not be integrated properly any more in a timely precise manner.

Congruently, Horn et al. (2010) showed that unilateral block of glutamatergic input to distinct IO sub-nuclei in the cat resulted in locomotion deficits such as limping of the contralateral leg, waddling and dragging (rostral MAO) and severe imbalance between the sides of the body (caudal MAO). A rather similar picture could be drawn by excitotoxic focal lesioning of IO sub-nuclei by kainic acid (Horn et al. 2012). In this study strong immediate effects were followed by initial compensation that then revolved into progressive ataxia on the long run indicating substantial adaptations.

Nevertheless, while we saw electrophysiological changes on the cellular level due to the RNAi based Cx36 knockdown, we cannot rule out that complex unexplored adaptations during the 11 days between injection of the lentiviral vector construct and locomotion assessment took place that could have partially compensated for the loss of coupling and yielded the mild phenotype observed here. It has been suggested that $Cx36^{-/-}$ mice may compensate the lack of gap junctional coupling by either regulating the genes that govern membrane properties and ion channel composition, or that during maturation a selection of certain neurons / neuronal progenitor cells may take place towards neurons that are intrinsic oscillators (De Zeeuw et al. 2003). We can rule out the latter in our approach because the RNAi effector was introduced postnatally after differentiation of olivary neurons has long been completed but suggest that uncoupling from postnatal week 3 on (and electrophysiological assessment at postnatal week 5) may have led to compensatory changes within existing neurons.

4.7 Immunohistology of Cx36 distribution

Comparison of Cx36 immunolabeling between transduced and non-transduced MAP2 positive (dendritic) structures yielded some insight into potential regulatory adaptations that might have happened after the RNAi based change in Cx36 expression. We could observe a reduction in the Cx36 spot density, hence in the number of Cx36 positive gap junctions, albeit this decrease was less than what would have been expected from the strong reduction in electrotonic coupling.

Unexpectedly, we saw an increase of the mean Cx36 spot diameter in transduced structures but also a pronounced decrease in the mean Cx36 spot labeling intensity. Given that the pore-constituting connexins within the gap junction are embedded in a scaffold that has yet only been partially dissected and understood (Ciolofan et al. 2006; Herve et al. 2012; Li et al. 2004; Lynn et al. 2012), we suggest that in the remaining detected gap junctions fewer connexins were incorporated, resulting in a lower spot intensity, but that, on the other hand, these connexins were distributed over an enlarged gap junction field. Whether such enlargement poses an active adaptation to the shortage of connexin in transduced structures or whether reduced stability of the scaffold due to the lack of connexin could lead to a deformation affecting the size of the gap junction plaque has to be left open here and would need to be addressed elsewhere.

4.8 Conclusion

The purpose of gap junctional coupling among IO neurons within the cerebellar orchestra still remains rather obscure.

In the hope for a better understanding, we tried to identify changes in activity and kinetics of regenerative events in IO neurons that could be associated with the degree of coupling. We found that spontaneous action potentials and spikelets were most frequently observed in neurons from three weeks old (3w) rats compared to two weeks (2w) and five weeks old (5w) rats. This time course was in congruence with the highest dye-coupling observed at that time point during postnatal development. The observed onset of STO after 2w falls into the time period of transition from early juvenile into a mature walking pattern (Westerga and Gramsbergen 1990). Moreover, the high spontaneous activity accompanied by a high degree of coupling observed around 3w is in accordance with the observation of a steep increase in CS firing rate of PC at that time (Arancillo et al. 2015). The higher activity may play an important role in the later phase of the reshaping / consolidation of the climbing fiber innervation to PC when the transition from multiple CF innervations towards single “winner” CF innervation takes place (Hashimoto et al. 2009; Sugihara 2006). Moreover, mGluR1 dependent segregation and refinement of synaptic territories of climbing fibers and parallel fibers on Purkinje cell dendrites around this developmental stage may depend on increased olivary / climbing fiber activity (Ichikawa et al. 2016).

Discussion

In paired patch clamp recordings from 5w neurons STO were found to be highly synchronous even when the coupling between the two recorded neurons was weak indicating a strong population drive. After uncoupling by RNAi, such robustness was eliminated and the neurons were more likely to show less synchronous STO.

Postnatal maturation of the IO resulted in faster kinetics of sAP and sp alike. Apparent phase-locking of sAP or sp to the peak of the STO cycle could not be observed earlier than at 5w. Uncoupling led to a loss of sp STO phase-locking while sAP STO phase-locking persisted.

We could identify parameters of sAP and sp kinetics that showed sensitivity to the STO phase or amplitude at the time of the event occurrence. In neurons of all age groups and after uncoupling sAP were faster when they occurred at the STO peak. In the 3w neurons sAP were faster at higher STO amplitude but this effect was reduced in 5w and sAP were even attenuated at higher STO amplitude in the case of uncoupling. Wavelets could be observed at all age groups and after uncoupling, and the number of wavelets per sAP was negatively correlated with the STO peak in 5w regardless of coupling and negatively correlated with the STO amplitude in 5w-shCx36. In contrast, sp kinetics were not found to be sensitive to the STO peak but to the rising or falling part of the oscillation cycle. Spikelets from all age groups or after uncoupling were slower when occurring on the rising part of the STO phase and faster on the falling part. The amplitude and duration of spikelets may be an important determinant of whether action potential threshold will be crossed during somatic integration and may govern the synchronicity of the IO output. However, whether information about the STO state is transmitted to PC via the climbing fiber (burst) signal would need to be investigated elsewhere. Yet, it is attractive to speculate about how STO state dependent alterations in regenerative event kinetics could be involved in the preservation of motor-error information over prolonged periods, which has recently been observed in Purkinje cell recordings from non-human primates (Junker et al. 2018).

Differences in locomotion were subtle and not visible at direct observation by the experimenter. We may ask if adaptations to the RNAi based coupling may have happened and how they might possibly compensate the loss of coupling. While elimination of GJA9 (the gene encoding the connexin 36 protein) in $Cx36^{-/-}$ mice has a widespread effect on the regulation of genes from all functional categories (Iacobas et al. 2007), one has to assume that there are mechanisms sensible to the presence and composition of gap junctions and a manifold of adaptations with cell-wide impact may occur which are hard to foresee. We see the loss of coupling accompanied by changes in activity and disturbed spikelet STO-phase relationship as clear indication for an improper olivary function in LV-shCx36 animals / 5w-shCX36 neurons and may assume that possible compensational mechanisms that could rescue a locomotor phenotype are likely located outside of the IO. Yet, whether the

cerebello-nucleo-olivary loop would be capable to adjust to olivary malfunction was beyond the scope of this study and would need further experimental attention.

The experimental work presented here will hopefully contribute to a better understanding of cerebellar function by providing insight into aspects of sub-threshold oscillation synchrony among neurons of the inferior olive and properties of regenerative events in the context of gap junctional coupling at different time points during postnatal development and after manipulation of gap junction functionality. We verified previous work on the necessity of gap junctions for synchronicity among olivary neurons and expanded current knowledge by detailed examination of event features and their relationship to the oscillatory state. Moreover, we identified subtle changes in locomotor activity after reduction of gap junctional coupling by knockdown of Connexin 36.

May our efforts form a brick in the construction of a comprehensive concept of information processing within the cerebellar system and help to elucidate the role of gap junctions within the inferior olive.

References

Akaneya Y, Jiang B, and Tsumoto T. RNAi-induced gene silencing by local electroporation in targeting brain region. *Journal of neurophysiology* 93: 594-602, 2005.

Albus JS. A theory of cerebellar function. *Mathematical Biosciences* 10: 25-61, 1971.

Apps R, and Garwicz M. Precise matching of olivo-cortical divergence and cortico-nuclear convergence between somatotopically corresponding areas in the medial C1 and medial C3 zones of the paravermal cerebellum. *The European journal of neuroscience* 12: 205-214, 2000.

Arancillo M, White JJ, Lin T, Stay TL, and Sillitoe RV. In vivo analysis of Purkinje cell firing properties during postnatal mouse development. *Journal of neurophysiology* 113: 578-591, 2015.

Armstrong DM, Harvey RJ, and Schild RF. Topographical localization in the olivo-cerebellar projection: an electrophysiological study in the cat. *The Journal of comparative neurology* 154: 287-302, 1974.

Azizi SA, and Woodward DJ. Inferior olivary nuclear complex of the rat: morphology and comments on the principles of organization within the olivocerebellar system. *The Journal of comparative neurology* 263: 467-484, 1987.

Baizer JS, Wong KM, Sherwood CC, Hof PR, and Witelson SF. Individual variability in the structural properties of neurons in the human inferior olive. *Brain structure & function* 223: 1667-1681, 2018.

Bazzigaluppi P, De Gruijl JR, van der Giessen RS, Khosrovani S, De Zeeuw CI, and de Jeu MT. Olivary subthreshold oscillations and burst activity revisited. *Frontiers in neural circuits* 6: 91, 2012.

Belluardo N, Mudo G, Trovato-Salinaro A, Le Gurun S, Charollais A, Serre-Beinier V, Amato G, Haefliger JA, Meda P, and Condorelli DF. Expression of connexin36 in the adult and developing rat brain. *Brain research* 865: 121-138, 2000.

Benedetti F, Montarolo PG, and Rabacchi S. Inferior olive lesion induces long-lasting functional modification in the Purkinje cells. *Experimental brain research* 55: 368-371, 1984.

Berens P. CircStat: A MATLAB Toolbox for Circular Statistics. *J Stat Softw* 31: 1-21, 2009.

Best AR, and Regehr WG. Inhibitory regulation of electrically coupled neurons in the inferior olive is mediated by asynchronous release of GABA. *Neuron* 62: 555-565, 2009.

Bleasel AF, and Pettigrew AG. Development and properties of spontaneous oscillations of the membrane potential in inferior olivary neurons in the rat. *Brain research Developmental brain research* 65: 43-50, 1992.

Blenkinsop TA, and Lang EJ. Block of inferior olive gap junctional coupling decreases Purkinje cell complex spike synchrony and rhythmicity. *The Journal of neuroscience : the official journal of the Society for Neuroscience* 26: 1739-1748, 2006.

Bourrat F, and Sotelo C. Postnatal development of the inferior olivary complex in the rat. I. An electron microscopic study of the medial accessory olive. *Brain research* 284: 291-310, 1983.

Burkarth N, Kriebel M, Kranz EU, and Volkmer H. Neurofascin regulates the formation of gephyrin clusters and their subsequent translocation to the axon hillock of hippocampal neurons. *Molecular and cellular neurosciences* 36: 59-70, 2007.

Catz N, Dicke PW, and Thier P. Cerebellar complex spike firing is suitable to induce as well as to stabilize motor learning. *Current biology : CB* 15: 2179-2189, 2005.

Cesa R, and Strata P. Axonal competition in the synaptic wiring of the cerebellar cortex during development and in the mature cerebellum. *Neuroscience* 162: 624-632, 2009.

Chen LW, Tse YC, Li C, Guan ZL, Lai CH, Yung KK, Shum DK, and Chan YS. Differential expression of NMDA and AMPA/KA receptor subunits in the inferior olive of postnatal rats. *Brain research* 1067: 103-114, 2006.

Cho HJ, Furness JB, and Jennings EA. Postnatal maturation of the hyperpolarization-activated cation current, I(h), in trigeminal sensory neurons. *Journal of neurophysiology* 106: 2045-2056, 2011.

Chorev E, and Brecht M. In vivo dual intra- and extracellular recordings suggest bidirectional coupling between CA1 pyramidal neurons. *Journal of neurophysiology* 108: 1584-1593, 2012.

Chorev E, Yarom Y, and Lampl I. Rhythmic episodes of subthreshold membrane potential oscillations in the rat inferior olive nuclei in vivo. *The Journal of neuroscience : the official journal of the Society for Neuroscience* 27: 5043-5052, 2007.

References

Ciolofan C, Li XB, Olson C, Kamasawa N, Gebhardt BR, Yasumura T, Morita M, Rash JE, and Nagy JI. Association of connexin36 and zonula occludens-1 with zonula occludens-2 and the transcription factor zonula occludens-1-associated nucleic acid-binding protein at neuronal gap junctions in rodent retina. *Neuroscience* 140: 433-451, 2006.

Condorelli DF, Parenti R, Spinella F, Trovato Salinaro A, Belluardo N, Cardile V, and Cicirata F. Cloning of a new gap junction gene (Cx36) highly expressed in mammalian brain neurons. *The European journal of neuroscience* 10: 1202-1208, 1998.

Crepel F. Maturation of climbing fiber responses in the rat. *Brain research* 35: 272-276, 1971.

Crepel F, Mariani J, and Delhaye-Bouchaud N. Evidence for a multiple innervation of Purkinje cells by climbing fibers in the immature rat cerebellum. *Journal of neurobiology* 7: 567-578, 1976.

Curti S, Hoge G, Nagy JI, and Pereda AE. Synergy between electrical coupling and membrane properties promotes strong synchronization of neurons of the mesencephalic trigeminal nucleus. *The Journal of neuroscience : the official journal of the Society for Neuroscience* 32: 4341-4359, 2012.

Curti S, and Pereda AE. Voltage-dependent enhancement of electrical coupling by a subthreshold sodium current. *The Journal of neuroscience : the official journal of the Society for Neuroscience* 24: 3999-4010, 2004.

Davidson BL, and McCray PB, Jr. Current prospects for RNA interference-based therapies. *Nature reviews Genetics* 12: 329-340, 2011.

De Gruijl JR, Bazzigaluppi P, de Jeu MT, and De Zeeuw CI. Climbing fiber burst size and olivary sub-threshold oscillations in a network setting. *PLoS computational biology* 8: e1002814, 2012.

De Gruijl JR, Hoogland TM, and De Zeeuw CI. Behavioral correlates of complex spike synchrony in cerebellar microzones. *The Journal of neuroscience : the official journal of the Society for Neuroscience* 34: 8937-8947, 2014.

De Zeeuw CI, Chorev E, Devor A, Manor Y, Van Der Giessen RS, De Jeu MT, Hoogenraad CC, Bijman J, Ruigrok TJ, French P, Jaarsma D, Kistler WM, Meier C, Petrasch-Parwez E, Dermietzel R, Sohl G, Gueldenagel M, Willecke K, and Yarom Y. Deformation of network connectivity in the inferior olive of connexin 36-deficient mice is compensated by morphological and electrophysiological changes at the single neuron level. *The Journal of neuroscience : the official journal of the Society for Neuroscience* 23: 4700-4711, 2003.

de Zeeuw CI, Holstege JC, Ruigrok TJ, and Voogd J. Mesodiencephalic and cerebellar terminals terminate upon the same dendritic spines in the glomeruli of the cat and rat inferior olive: an ultrastructural study using a combination of [3H]leucine and wheat germ agglutinin coupled horseradish peroxidase anterograde tracing. *Neuroscience* 34: 645-655, 1990a.

de Zeeuw CI, Ruigrok TJ, Holstege JC, Jansen HG, and Voogd J. Intracellular labeling of neurons in the medial accessory olive of the cat: II. Ultrastructure of dendritic spines and their GABAergic innervation. *The Journal of comparative neurology* 300: 478-494, 1990b.

de Zeeuw CI, Ruigrok TJ, Schalekamp MP, Boesten AJ, and Voogd J. Ultrastructural study of the cat hypertrophic inferior olive following anterograde tracing, immunocytochemistry, and intracellular labeling. *European journal of morphology* 28: 240-255, 1990c.

Deans MR, Gibson JR, Sellitto C, Connors BW, and Paul DL. Synchronous activity of inhibitory networks in neocortex requires electrical synapses containing connexin36. *Neuron* 31: 477-485, 2001.

Desclin JC. Histological evidence supporting the inferior olive as the major source of cerebellar climbing fibers in the rat. *Brain research* 77: 365-384, 1974.

Devor A, and Yarom Y. Electrotonic coupling in the inferior olivary nucleus revealed by simultaneous double patch recordings. *Journal of neurophysiology* 87: 3048-3058, 2002a.

Devor A, and Yarom Y. Generation and propagation of subthreshold waves in a network of inferior olivary neurons. *Journal of neurophysiology* 87: 3059-3069, 2002b.

Deyle DR, and Russell DW. Adeno-associated virus vector integration. *Current opinion in molecular therapeutics* 11: 442-447, 2009.

Doench JG, Petersen CP, and Sharp PA. siRNAs can function as miRNAs. *Genes & development* 17: 438-442, 2003.

References

Dugue GP, Brunel N, Hakim V, Schwartz E, Chat M, Levesque M, Courtemanche R, Lena C, and Dieudonne S. Electrical coupling mediates tunable low-frequency oscillations and resonance in the cerebellar Golgi cell network. *Neuron* 61: 126-139, 2009.

Elbashir SM, Harborth J, Lendeckel W, Yalcin A, Weber K, and Tuschl T. Duplexes of 21-nucleotide RNAs mediate RNA interference in cultured mammalian cells. *Nature* 411: 494-498, 2001a.

Elbashir SM, Lendeckel W, and Tuschl T. RNA interference is mediated by 21- and 22-nucleotide RNAs. *Genes & development* 15: 188-200, 2001b.

Elbashir SM, Martinez J, Patkaniowska A, Lendeckel W, and Tuschl T. Functional anatomy of siRNAs for mediating efficient RNAi in Drosophila melanogaster embryo lysate. *The EMBO journal* 20: 6877-6888, 2001c.

Elkobi A, Ehrlich I, Belelovsky K, Barki-Harrington L, and Rosenblum K. ERK-dependent PSD-95 induction in the gustatory cortex is necessary for taste learning, but not retrieval. *Nature neuroscience* 11: 1149-1151, 2008.

Fire A, Xu S, Montgomery MK, Kostas SA, Driver SE, and Mello CC. Potent and specific genetic interference by double-stranded RNA in Caenorhabditis elegans. *Nature* 391: 806-811, 1998.

Foster RE, and Peterson BE. The inferior olivary complex of guinea pig: cytoarchitecture and cellular morphology. *Brain research bulletin* 17: 785-800, 1986.

Frisch C, De Souza-Silva MA, Sohl G, Guldenagel M, Willecke K, Huston JP, and Dere E. Stimulus complexity dependent memory impairment and changes in motor performance after deletion of the neuronal gap junction protein connexin36 in mice. *Behavioural brain research* 157: 177-185, 2005.

Galarreta M, and Hestrin S. A network of fast-spiking cells in the neocortex connected by electrical synapses. *Nature* 402: 72-75, 1999.

Gellman R, Houk JC, and Gibson AR. Somatosensory properties of the inferior olive of the cat. *The Journal of comparative neurology* 215: 228-243, 1983.

Gibson AR, Horn KM, and Pong M. Activation of climbing fibers. *Cerebellum* 3: 212-221, 2004.

Glickstein M, Sultan F, and Voogd J. Functional localization in the cerebellum. *Cortex; a journal devoted to the study of the nervous system and behavior* 47: 59-80, 2011.

Grimm D, Streetz KL, Jopling CL, Storm TA, Pandey K, Davis CR, Marion P, Salazar F, and Kay MA. Fatality in mice due to oversaturation of cellular microRNA/short hairpin RNA pathways. *Nature* 441: 537-541, 2006.

Güldenagel M, Ammermüller J, Feigenspan A, Teubner B, Degen J, Söhl G, Willecke K, and Weiler R. Visual transmission deficits in mice with targeted disruption of the gap junction gene connexin36. *The Journal of neuroscience : the official journal of the Society for Neuroscience* 21: 6036-6044, 2001.

Guo S, and Kemphues KJ. par-1, a gene required for establishing polarity in C. elegans embryos, encodes a putative Ser/Thr kinase that is asymmetrically distributed. *Cell* 81: 611-620, 1995.

Hashimoto K, Ichikawa R, Kitamura K, Watanabe M, and Kano M. Translocation of a "winner" climbing fiber to the Purkinje cell dendrite and subsequent elimination of "losers" from the soma in developing cerebellum. *Neuron* 63: 106-118, 2009.

Hashimoto K, and Kano M. Functional differentiation of multiple climbing fiber inputs during synapse elimination in the developing cerebellum. *Neuron* 38: 785-796, 2003.

Hashimoto K, and Kano M. Synapse elimination in the developing cerebellum. *Cellular and molecular life sciences : CMLS* 70: 4667-4680, 2013.

Herve JC, Derangeon M, Sarrouilhe D, Giepmans BN, and Bourmeyster N. Gap junctional channels are parts of multiprotein complexes. *Biochimica et biophysica acta* 1818: 1844-1865, 2012.

Hoge GJ, Davidson KG, Yasumura T, Castillo PE, Rash JE, and Pereda AE. The extent and strength of electrical coupling between inferior olivary neurons is heterogeneous. *Journal of neurophysiology* 105: 1089-1101, 2011.

Hoogland TM, De Gruijl JR, Witter L, Canto CB, and De Zeeuw CI. Role of Synchronous Activation of Cerebellar Purkinje Cell Ensembles in Multi-joint Movement Control. *Current biology : CB* 25: 1157-1165, 2015.

Horn KM, Deep A, and Gibson AR. Progressive Limb Ataxia Following Inferior Olive Lesions. *The Journal of physiology* 2012.

References

Horn KM, Pong M, and Gibson AR. Functional relations of cerebellar modules of the cat. *The Journal of neuroscience : the official journal of the Society for Neuroscience* 30: 9411-9423, 2010.

Iacobas DA, Iacobas S, and Spray DC. Connexin-dependent transcellular transcriptomic networks in mouse brain. *Progress in biophysics and molecular biology* 94: 169-185, 2007.

Ichikawa R, Hashimoto K, Miyazaki T, Uchigashima M, Yamasaki M, Aiba A, Kano M, and Watanabe M. Territories of heterologous inputs onto Purkinje cell dendrites are segregated by mGluR1-dependent parallel fiber synapse elimination. *Proc Natl Acad Sci U S A* 113: 2282-2287, 2016.

Isacson R, Kull B, Salmi P, and Wahlestedt C. Lack of efficacy of 'naked' small interfering RNA applied directly to rat brain. *Acta physiologica Scandinavica* 179: 173-177, 2003.

Junker M, Endres D, Sun ZP, Dicke PW, Giese M, and Thier P. Learning from the past: A reverberation of past errors in the cerebellar climbing fiber signal. *PLoS biology* 16: e2004344, 2018.

Kakegawa W, Mitakidis N, Miura E, Abe M, Matsuda K, Takeo YH, Kohda K, Motohashi J, Takahashi A, Nagao S, Muramatsu S, Watanabe M, Sakimura K, Aricescu AR, and Yuzaki M. Anterograde C1ql1 signaling is required in order to determine and maintain a single-winner climbing fiber in the mouse cerebellum. *Neuron* 85: 316-329, 2015.

Kaneko M, Yamaguchi K, Eiraku M, Sato M, Takata N, Kiyohara Y, Mishina M, Hirase H, Hashikawa T, and Kengaku M. Remodeling of monoplanar Purkinje cell dendrites during cerebellar circuit formation. *PloS one* 6: e20108, 2011.

Khosrovani S, Van Der Giessen RS, De Zeeuw CI, and De Jeu MT. In vivo mouse inferior olive neurons exhibit heterogeneous subthreshold oscillations and spiking patterns. *Proc Natl Acad Sci U S A* 104: 15911-15916, 2007.

Kistler WM, De Jeu MT, Elgersma Y, Van Der Giessen RS, Hensbroek R, Luo C, Koekkoek SK, Hoogenraad CC, Hamers FP, Gueldenagel M, Sohl G, Willecke K, and De Zeeuw CI. Analysis of Cx36 knockout does not support tenet that olivary gap junctions are required for complex spike synchronization and normal motor performance. *Annals of the New York Academy of Sciences* 978: 391-404, 2002.

Kølvraa M, Muller FC, Jahnsen H, and Rekling JC. Mechanisms Contributing to Cluster Formation in the Inferior Olivary Nucleus in Brainstem Slices from Postnatal Mice. *The Journal of physiology* 2013.

Kriebel M, Metzger J, Trinks S, Chugh D, Harvey RJ, Harvey K, and Volkmer H. The cell adhesion molecule neurofascin stabilizes axo-axonic GABAergic terminals at the axon initial segment. *The Journal of biological chemistry* 286: 24385-24393, 2011.

Lampl I, and Yarom Y. Subthreshold oscillations of the membrane potential: a functional synchronizing and timing device. *Journal of neurophysiology* 70: 2181-2186, 1993.

Lang EJ, Tang T, Suh CY, Xiao J, Kotsurovskyy Y, Blenkinsop TA, Marshall SP, and Sugihara I. Modulation of Purkinje cell complex spike waveform by synchrony levels in the olivocerebellar system. *Frontiers in systems neuroscience* 8: 210, 2014.

Lefler Y, Yarom Y, and Uusisaari MY. Cerebellar inhibitory input to the inferior olive decreases electrical coupling and blocks subthreshold oscillations. *Neuron* 81: 1389-1400, 2014.

Lentz TB, Gray SJ, and Samulski RJ. Viral vectors for gene delivery to the central nervous system. *Neurobiology of disease* 48: 179-188, 2012.

Leznik E, and Llinas R. Role of gap junctions in synchronized neuronal oscillations in the inferior olive. *Journal of neurophysiology* 94: 2447-2456, 2005.

Leznik E, Makarenko V, and Llinas R. Electrotonically mediated oscillatory patterns in neuronal ensembles: an in vitro voltage-dependent dye-imaging study in the inferior olive. *The Journal of neuroscience : the official journal of the Society for Neuroscience* 22: 2804-2815, 2002.

Li X, Olson C, Lu S, Kamasawa N, Yasumura T, Rash JE, and Nagy JI. Neuronal connexin36 association with zonula occludens-1 protein (ZO-1) in mouse brain and interaction with the first PDZ domain of ZO-1. *The European journal of neuroscience* 19: 2132-2146, 2004.

Llinas R. Eighteenth Bowditch lecture. Motor aspects of cerebellar control. *The Physiologist* 17: 19-46, 1974.

Llinas R, Baker R, and Sotelo C. Electrotonic coupling between neurons in cat inferior olive. *Journal of neurophysiology* 37: 560-571, 1974.

References

Llinas R, and Muhlethaler M. An electrophysiological study of the in vitro, perfused brain stem-cerebellum of adult guinea-pig. *The Journal of physiology* 404: 215-240, 1988.

Llinas R, and Sasaki K. The Functional Organization of the Olivo-Cerebellar System as Examined by Multiple Purkinje Cell Recordings. *The European journal of neuroscience* 1: 587-602, 1989.

Llinas R, Walton K, Hillman DE, and Sotelo C. Inferior olive: its role in motor learning. *Science* 190: 1230-1231, 1975.

Llinas R, and Yarom Y. Electrophysiology of mammalian inferior olivary neurones in vitro. Different types of voltage-dependent ionic conductances. *The Journal of physiology* 315: 549-567, 1981a.

Llinas R, and Yarom Y. Oscillatory properties of guinea-pig inferior olivary neurones and their pharmacological modulation: an in vitro study. *The Journal of physiology* 376: 163-182, 1986.

Llinas R, and Yarom Y. Properties and distribution of ionic conductances generating electroresponsiveness of mammalian inferior olivary neurones in vitro. *The Journal of physiology* 315: 569-584, 1981b.

Llinas RR. Inferior olive oscillation as the temporal basis for motricity and oscillatory reset as the basis for motor error correction. *Neuroscience* 162: 797-804, 2009.

Llinas RR. The olivo-cerebellar system: a key to understanding the functional significance of intrinsic oscillatory brain properties. *Frontiers in neural circuits* 7: 96, 2013.

Long MA, Deans MR, Paul DL, and Connors BW. Rhythmicity without synchrony in the electrically uncoupled inferior olive. *The Journal of neuroscience : the official journal of the Society for Neuroscience* 22: 10898-10905, 2002.

Lu H, Yang B, and Jaeger D. Cerebellar Nuclei Neurons Show Only Small Excitatory Responses to Optogenetic Olivary Stimulation in Transgenic Mice: In Vivo and In Vitro Studies. *Frontiers in neural circuits* 10: 21, 2016.

Lynn BD, Li X, and Nagy JI. Under construction: building the macromolecular superstructure and signaling components of an electrical synapse. *The Journal of membrane biology* 245: 303-317, 2012.

MacVicar BA, and Dudek FE. Electrotonic coupling between pyramidal cells: a direct demonstration in rat hippocampal slices. *Science* 213: 782-785, 1981.

Manjarrez-Marmolejo J, and Franco-Perez J. Gap Junction Blockers: An Overview of their Effects on Induced Seizures in Animal Models. *Current neuropharmacology* 14: 759-771, 2016.

Mann-Metzer P, and Yarom Y. Electrotonic coupling interacts with intrinsic properties to generate synchronized activity in cerebellar networks of inhibitory interneurons. *The Journal of neuroscience : the official journal of the Society for Neuroscience* 19: 3298-3306, 1999.

Marr D. A theory of cerebellar cortex. *The Journal of physiology* 202: 437-470, 1969.

Marshall SP, van der Giessen RS, de Zeeuw CI, and Lang EJ. Altered olivocerebellar activity patterns in the connexin36 knockout mouse. *Cerebellum* 6: 287-299, 2007.

Mathy A, Clark BA, and Hausser M. Synaptically induced long-term modulation of electrical coupling in the inferior olive. *Neuron* 81: 1290-1296, 2014.

Mathy A, Ho SS, Davie JT, Duguid IC, Clark BA, and Hausser M. Encoding of oscillations by axonal bursts in inferior olive neurons. *Neuron* 62: 388-399, 2009.

Medina JF, and Lisberger SG. Links from complex spikes to local plasticity and motor learning in the cerebellum of awake-behaving monkeys. *Nature neuroscience* 11: 1185-1192, 2008.

Meier C, Petrasch-Parwez E, Habbes HW, Teubner B, Guldenagel M, Degen J, Sohl G, Willecke K, and Dermietzel R. Immunohistochemical detection of the neuronal connexin36 in the mouse central nervous system in comparison to connexin36-deficient tissues. *Histochemistry and cell biology* 117: 461-471, 2002.

Mercer A, Bannister AP, and Thomson AM. Electrical coupling between pyramidal cells in adult cortical regions. *Brain cell biology* 35: 13-27, 2006.

Metzger F. Molecular and cellular control of dendrite maturation during brain development. *Current molecular pharmacology* 3: 1-11, 2010.

Morara S, van der Want JJ, de Weerd H, Provini L, and Rosina A. Ultrastructural analysis of climbing fiber-Purkinje cell synaptogenesis in the rat cerebellum. *Neuroscience* 108: 655-671, 2001.

Murphy MG, and O'Leary JL. Neurological deficit in cats with lesions of the olivocebellar system. *Archives of neurology* 24: 145-157, 1971.

References

Negrello M, Warnaar P, Romano V, Owens CB, Lindeman S, Iavarone E, Spanke JK, Bosman LWJ, and De Zeeuw CI. Quasiperiodic rhythms of the inferior olive. *PLoS computational biology* 15: e1006475, 2019.

O'Brien J. The ever-changing electrical synapse. *Current opinion in neurobiology* 29C: 64-72, 2014.

Ozcan G, Ozpolat B, Coleman RL, Sood AK, and Lopez-Berestein G. Preclinical and clinical development of siRNA-based therapeutics. *Advanced drug delivery reviews* 2015.

Ozden I, Dombeck DA, Hoogland TM, Tank DW, and Wang SS. Widespread state-dependent shifts in cerebellar activity in locomoting mice. *PloS one* 7: e42650, 2012.

Pardridge WM. Drug and gene delivery to the brain: the vascular route. *Neuron* 36: 555-558, 2002.

Paxinos G, and Watson C. *The rat brain in stereotaxic coordinates*. San Diego: Academic Press, 1998.

Pettigrew AG, Crepel F, and Krupa M. Development of ionic conductances in neurons of the inferior olive in the rat: an in vitro study. *Proceedings of the Royal Society of London Series B, Containing papers of a Biological character Royal Society* 234: 199-218, 1988.

Placantonakis D, and Welsh J. Two distinct oscillatory states determined by the NMDA receptor in rat inferior olive. *The Journal of physiology* 534: 123-140, 2001.

Placantonakis DG, Bukovsky AA, Aicher SA, Kiem HP, and Welsh JP. Continuous electrical oscillations emerge from a coupled network: a study of the inferior olive using lentiviral knockdown of connexin36. *The Journal of neuroscience : the official journal of the Society for Neuroscience* 26: 5008-5016, 2006.

Placantonakis DG, Bukovsky AA, Zeng XH, Kiem HP, and Welsh JP. Fundamental role of inferior olive connexin 36 in muscle coherence during tremor. *Proc Natl Acad Sci U S A* 101: 7164-7169, 2004.

Puram SV, and Bonni A. Cell-intrinsic drivers of dendrite morphogenesis. *Development* 140: 4657-4671, 2013.

Rabinowitz JE, Rolling F, Li C, Conrath H, Xiao W, Xiao X, and Samulski RJ. Cross-packaging of a single adeno-associated virus (AAV) type 2 vector genome into multiple AAV serotypes enables transduction with broad specificity. *Journal of virology* 76: 791-801, 2002.

Ramón y Cajal S. *Histologie du système nerveux de l'homme & des vertébrés*. Paris: Maloine, A., 1909.

Rao H, Jean A, and Kessler JP. Postnatal changes in glutamate binding in the lower medulla of the rat. *Neuroscience letters* 188: 21-24, 1995.

Rash JE, Olson CO, Pouliot WA, Davidson KG, Yasumura T, Furman CS, Royer S, Kamasawa N, Nagy JI, and Dudek FE. Connexin36 vs. connexin32, "miniature" neuronal gap junctions, and limited electrotonic coupling in rodent suprachiasmatic nucleus. *Neuroscience* 149: 350-371, 2007.

Rasmussen A, Jirenhed DA, Wetmore DZ, and Hesslow G. Changes in complex spike activity during classical conditioning. *Frontiers in neural circuits* 8: 90, 2014.

Rasmussen A, Jirenhed DA, Zucca R, Johansson F, Svensson P, and Hesslow G. Number of spikes in climbing fibers determines the direction of cerebellar learning. *The Journal of neuroscience : the official journal of the Society for Neuroscience* 33: 13436-13440, 2013.

Rekling JC, Jensen KH, and Jahnsen H. Spontaneous cluster activity in the inferior olivary nucleus in brainstem slices from postnatal mice. *The Journal of physiology* 590: 1547-1562, 2012.

Rossi P, D'Angelo E, Magistretti J, Toselli M, and Taglietti V. Age-dependent expression of high-voltage activated calcium currents during cerebellar granule cell development in situ. *Pflugers Archiv : European journal of physiology* 429: 107-116, 1994.

Rouach N, Segal M, Koulakoff A, Giaume C, and Avignone E. Carbenoxolone blockade of neuronal network activity in culture is not mediated by an action on gap junctions. *The Journal of physiology* 553: 729-745, 2003.

Rozental R, Srinivas M, and Spray DC. How to close a gap junction channel. Efficacies and potencies of uncoupling agents. *Methods in molecular biology* 154: 447-476, 2001.

Ruigrok TJ. Ins and outs of cerebellar modules. *Cerebellum* 10: 464-474, 2011.

Ruigrok TJ, de Zeeuw CI, and Voogd J. Hypertrophy of inferior olivary neurons: a degenerative, regenerative or plasticity phenomenon. *European journal of morphology* 28: 224-239, 1990.

Schmitz D, Schuchmann S, Fisahn A, Draguhn A, Buhl EH, Petrasch-Parwez E, Dermietzel R, Heinemann U, and Traub RD. Axo-axonal coupling. a novel mechanism for ultrafast neuronal communication. *Neuron* 31: 831-840, 2001.

References

Schnepp BC, Jensen RL, Chen CL, Johnson PR, and Clark KR. Characterization of adeno-associated virus genomes isolated from human tissues. *Journal of virology* 79: 14793-14803, 2005.
Schwarz C, and Welsh JP. Dynamic modulation of mossy fiber system throughput by inferior olive synchrony: a multielectrode study of cerebellar cortex activated by motor cortex. *Journal of neurophysiology* 86: 2489-2504, 2001.
Shaikh AG, Hong S, Liao K, Tian J, Solomon D, Zee DS, Leigh RJ, and Optican LM. Oculopalatal tremor explained by a model of inferior olivary hypertrophy and cerebellar plasticity. *Brain : a journal of neurology* 133: 923-940, 2010.
Shaikh AG, Wong AL, Optican LM, and Zee DS. Impaired Motor Learning in a Disorder of the Inferior Olive: Is the Cerebellum Confused? *Cerebellum* 16: 158-167, 2017.
Sioud M. Deciphering the code of innate immunity recognition of siRNAs. *Methods in molecular biology* 487: 41-59, 2009.
Smith SS. Step cycle-related oscillatory properties of inferior olivary neurons recorded in ensembles. *Neuroscience* 82: 69-81, 1998.
Soechting JF, Ranish NA, Palminteri R, and Terzuolo CA. Changes in a motor pattern following cerebellar and olivary lesions in the squirrel monkey. *Brain research* 105: 21-44, 1976.
Sotelo C, Llinas R, and Baker R. Structural study of inferior olivary nucleus of the cat: morphological correlates of electrotonic coupling. *Journal of neurophysiology* 37: 541-559, 1974.
Spencer WA, and Kandel ER. Electrophysiology of hippocampal neurons IV. Fast prepotentials. *Journal of neurophysiology* 24: 272-285, 1961.
Sugihara I. Organization and remodeling of the olivocerebellar climbing fiber projection. *Cerebellum* 5: 15-22, 2006.
Sugihara I, and Shinoda Y. Molecular, topographic, and functional organization of the cerebellar cortex: a study with combined aldolase C and olivocerebellar labeling. *The Journal of neuroscience : the official journal of the Society for Neuroscience* 24: 8771-8785, 2004.
Sugihara I, and Shinoda Y. Molecular, topographic, and functional organization of the cerebellar nuclei: analysis by three-dimensional mapping of the olivonuclear projection and aldolase C labeling. *The Journal of neuroscience : the official journal of the Society for Neuroscience* 27: 9696-9710, 2007.
Sugihara I, Wu HS, and Shinoda Y. The entire trajectories of single olivocerebellar axons in the cerebellar cortex and their contribution to Cerebellar compartmentalization. *The Journal of neuroscience : the official journal of the Society for Neuroscience* 21: 7715-7723, 2001.
Szentágothai J, and Rajkovits K. Über den Ursprung der Kletterfasern des Kleinhirns. *Z Anat Entwickl Gesch* 121: 130-141, 1959.
Takasaki S. Methods for selecting effective siRNA sequences by using statistical and clustering techniques. *Methods in molecular biology* 487: 1-39, 2009.
Tilikete C, and Desestret V. Hypertrophic Olivary Degeneration and Palatal or Oculopalatal Tremor. *Frontiers in neurology* 8: 302, 2017.
Tokuno H, Ikeuchi Y, Nambu A, Akazawa T, Imanishi M, Hamada I, and Hasegawa N. A modified microsyringe for extracellular recording of neuronal activity. *Neuroscience research* 31: 251-255, 1998.
Torben-Nielsen B, Segev I, and Yarom Y. The generation of phase differences and frequency changes in a network model of inferior olive subthreshold oscillations. *PLoS computational biology* 8: e1002580, 2012.
Tovar KR, Maher BJ, and Westbrook GL. Direct actions of carbenoxolone on synaptic transmission and neuronal membrane properties. *Journal of neurophysiology* 102: 974-978, 2009.
Turecek J, Yuen GS, Han VZ, Zeng XH, Bayer KU, and Welsh JP. NMDA receptor activation strengthens weak electrical coupling in mammalian brain. *Neuron* 81: 1375-1388, 2014.
Van Der Giessen RS, Koekkoek SK, van Dorp S, De Gruijl JR, Cupido A, Khosrovani S, Dortland B, Wellershaus K, Degen J, Deuchars J, Fuchs EC, Monyer H, Willecke K, De Jeu MT, and De Zeeuw CI. Role of olivary electrical coupling in cerebellar motor learning. *Neuron* 58: 599-612, 2008.
Van Der Giessen RS, Maxeiner S, French PJ, Willecke K, and De Zeeuw CI. Spatiotemporal distribution of Connexin45 in the olivocerebellar system. *The Journal of comparative neurology* 495: 173-184, 2006.

van Essen TA, van der Giessen RS, Koekkoek SK, Vanderwerf F, Zeeuw CI, van Genderen PJ, Overbosch D, and de Jeu MT. Anti-malaria drug mefloquine induces motor learning deficits in humans. *Frontiers in neuroscience* 4: 191, 2010.

van Welie I, Roth A, Ho SS, Komai S, and Hausser M. Conditional Spike Transmission Mediated by Electrical Coupling Ensures Millisecond Precision-Correlated Activity among Interneurons In Vivo. *Neuron* 90: 810-823, 2016.

Vaney DI, Nelson JC, and Pow DV. Neurotransmitter coupling through gap junctions in the retina. *The Journal of neuroscience : the official journal of the Society for Neuroscience* 18: 10594-10602, 1998.

Vincent A, Lautermilch NJ, and Spitzer NC. Antisense suppression of potassium channel expression demonstrates its role in maturation of the action potential. *The Journal of neuroscience : the official journal of the Society for Neuroscience* 20: 6087-6094, 2000.

Vrieler N, Loyola S, Yarden-Rabinowitz Y, Hoogendorp J, Medvedev N, Hoogland TM, De Zeeuw CI, De Schutter E, Yarom Y, Negrello M, Torben-Nielsen B, and Uusisaari MY. Variability and directionality of inferior olive neuron dendrites revealed by detailed 3D characterization of an extensive morphological library. *Brain structure & function* 224: 1677-1695, 2019.

Warnaar P, Couto J, Negrello M, Junker M, Smilgin A, Ignashchenkova A, Giugliano M, Thier P, and De Schutter E. Duration of Purkinje cell complex spikes increases with their firing frequency. *Frontiers in cellular neuroscience* 9: 122, 2015.

Wassef M, Chedotal A, Cholley B, Thomasset M, Heizmann CW, and Sotelo C. Development of the olivocerebellar projection in the rat: I. Transient biochemical compartmentation of the inferior olive. *The Journal of comparative neurology* 323: 519-536, 1992.

Welsh JP, and Harvey JA. Acute inactivation of the inferior olive blocks associative learning. *The European journal of neuroscience* 10: 3321-3332, 1998.

Welsh JP, Lang EJ, Sugihara I, and Llinas R. Dynamic organization of motor control within the olivocerebellar system. *Nature* 374: 453-457, 1995.

Westerga J, and Gramsbergen A. The development of locomotion in the rat. *Brain research Developmental brain research* 57: 163-174, 1990.

Wilson WC, and Magoun HW. The functional significance of the inferior olive in the cat. *J Comp Neurol* 83: 69-77, 1945.

Xia H, Mao Q, Eliason SL, Harper SQ, Martins IH, Orr HT, Paulson HL, Yang L, Kotin RM, and Davidson BL. RNAi suppresses polyglutamine-induced neurodegeneration in a model of spinocerebellar ataxia. *Nature medicine* 10: 816-820, 2004.

Yaeger DB, and Trussell LO. Auditory Golgi cells are interconnected predominantly by electrical synapses. *Journal of neurophysiology* 116: 540-551, 2016.

Yang Y, and Lisberger SG. Purkinje-cell plasticity and cerebellar motor learning are graded by complex-spike duration. *Nature* 510: 529-532, 2014.

Yeo CH, Hardiman MJ, and Glickstein M. Classical conditioning of the nictitating membrane response of the rabbit. II. Lesions of the cerebellar cortex. *Experimental brain research* 60: 99-113, 1985.

Zamore PD, Tuschl T, Sharp PA, and Bartel DP. RNAi: double-stranded RNA directs the ATP-dependent cleavage of mRNA at 21 to 23 nucleotide intervals. *Cell* 101: 25-33, 2000.

Zappala A, Parenti R, La Delia F, Cicirata V, and Cicirata F. Expression of connexin57 in mouse development and in harmaline-tremor model. *Neuroscience* 171: 1-11, 2010.

Zar JH. *Biostatistical analysis*. Upper Saddle River, N.J.: Prentice Hall, 1999.

Zbarska S, Bloedel JR, and Bracha V. Cerebellar dysfunction explains the extinction-like abolition of conditioned eyeblinks after NBQX injections in the inferior olive. *The Journal of neuroscience : the official journal of the Society for Neuroscience* 28: 10-20, 2008.

Zhu Z, Zeng XH, Turecek J, Han VZ, and Welsh JP. RNA Interference of GluN1 Inhibits Neuronal Rhythmogenesis in the Adult Inferior Olive. *Journal of molecular neuroscience : MN* 2014.

Zitman FM, Lucas M, Trinks S, Grosse-Ophoff L, Kriebel M, Volkmer H, and Richter-Levin G. Dentate Gyrus Local Circuit is Implicated in Learning Under Stress-a Role for Neurofascin. *Molecular neurobiology* 2014.

References

Zutphen LFMv, Baumans V, and Beynen AC. *Principles of laboratory animal science : a contribution to the humane use and care of animals and to the quality of experimental results*. Amsterdam ; New York: Elsevier, 2001, p. xii, 416 p.

Supplementary

List of abbreviations

AAV	adeno-associated virus
ACSF	artificial cerebrospinal fluid
ADP	after-depolarization
AMPA	α-amino-3-hydroxy-5-methyl-4-isoxazolepropionic acid
ANOVA	analysis of variance
AP	anterior-posterior
a.u.	arbitrary unit
BC	basket cell
CAMKIIα	calcium/calmodulin-dependent protein kinase II alpha
CC	coupling coefficient
CCC	cross-correlation coefficient
CF	climbing fiber
CN	cerebellar nuclei
CS	complex spike
Cx36	connexin 36
DAO	dorsal accessory olive
DJP	depolarizing junctional potential
EGFP	enhanced green fluorescent protein
GABA	γ-aminobutyric acid
GC	Golgi cell
GJ	gap junction
HOD	hypertrophic olivary degeneration
hU6	human U6 promoter
IO	inferior olive
I_{GJ}	gap junctional current
IPSP	inhibitory post-synaptic potential
KW	Kruskal-Wallis ANOVA on ranks
LP	lentiviral particles
LV	lentiviral vector
MAO	medial accessory olive
MAP2	microtubule-associated protein 2
MF	mossy fiber
ML	medio-lateral

Supplementary

mRNA	messenger RNA
MWU	Mann–Whitney U test
NMDA	N-methyl-D-aspartate
ns	non-significant
p	postnatal day
PB	phosphate buffer
PBS	phosphate-buffered saline
PC	Purkinje cell
PF	parallel fiber
PFA	paraformaldehyde
PO	principal olive
RNA	ribonucleic acid
RNAi	RNA interference
sAP	spontaneous action potential
SEM	standard error of the mean
shCx36	short-hairpin RNA targeting connexin 36
shCTR	short-hairpin RNA non-functional control
shRNA	short-hairpin RNA
sp	spikelet
SS	simple spike
STO	sub-threshold oscillation
TU	transducing units
VI	voltage-current
WPRE	woodchuck hepatitis virus posttranscriptional regulatory element
WT	wildtype

List of figures

Conference contributions

Parts of this work have been presented in poster form at the following conferences.

Müller JM, Kriebel M, Volkmer H, Thier P. **Locomotor deficits after spatially restricted knock-down of Connexin 36 in the inferior olive of juvenile rats?** Program No. 379.19. Society for Neuroscience, 2012. New Orleans, LA.

Müller JM, Kriebel M, Volkmer H, Thier P. **Developmental dynamics of gap junction based neuronal coupling in the rat inferior olive.** Program No. 868.09. Society for Neuroscience, 2011. Washington, DC.

Müller JM, Kriebel M, Volkmer H, Thier P. **Using RNA interference to assess the role of dendro-dendritic gap junctions in the rat inferior olive.** Program No. 786.08. Society for Neuroscience, 2010. San Diego, CA.

Funding and stipends

This work is part of the research program of the Bernstein Center for Computational Neuroscience, Tübingen, funded by the German Federal Ministry of Education and Research (BMBF FKZ: 01GQ1002, A C3). The author received a fellowship of the integrated graduate program at the DFG Collaborative Research Centre „Recognize, Localize, Act: Neurocognitive Mechanisms and their Flexibility" (SFB 550) in Tübingen from Jan – Feb 2008. Travel stipends to attend the Society for Neuroscience conferences were provided by the Graduate Training Centre of Neuroscience, Tübingen, Germany.

Acknowledgements

I thank Peter Thier for giving me the opportunity to perform this work and for promoting my development as a scientist, for being a mentor on critical reasoning and an inspiring discussion partner.

I thank Hansjürgen Volkmer, Martin Kriebel and the members of the Department of Molecular Neurobiology at the NMI Reutlingen for providing me the opportunity to benefit from their extensive knowledge and resources in the design and production of the lentiviral vectors for shRNA delivery.

I thank Martin Möck for the practical introduction into the preparation of brainstem slices and into patch clamping of olivary neurons.

I thank Salah Hammodeh for practical help on immunohistology and for many discussions on the miracles of the cerebellar connectivity.

I thank Christine Pedroarena for insights into the electrophysiology and function of the cerebellar nuclei and for the pleasure of sharing the in vitro electrophysiology lab.

I thank Cornelius Schwarz and the members of the Systems Neurophysiology research group for help on innumerable aspects, and Sergejus Butovas in particular for introducing me to *in vivo* electrophysiology in the rat.

I thank Ute Großhennig and Ursula Pascht for excellent technical assistance and magnificent lab management.

I thank Mathias Jucker and the members of the Department of Cellular Neurology, Simone DiGiovanni (now Imperial College London) and the members of the former Neuroregeneration research group, Thomas Ott and the members of the animal facility for supporting the progress of my work by gracious access to their resources.

I thank all current and past members of the Department for Cognitive Neurology in particular and the community of neuroscientists in Tübingen in general and everyone whom I had the pleasure to work with.

I thank the Graduate Training Center for their broad spectrum of professional development initiatives and for funding of conference attendances.

I thank the Hertie Foundation for their generous financial dedication to the neurosciences that nurtures a flourishing neuroscience community in Tübingen in an outstanding way.

Finally, I thank my parents and family for their constant and endless support.